UNIVERSITY OF CALIFORNIA SAN DIEGO

Tools for Data-Driven Investigation of the Durability of Photovoltaics

A dissertation submitted in partial satisfaction of the
requirements for the degree of Doctor of Philosophy

in

Materials Science and Engineering

by

Rishi Eugene Kumar

Committee in charge:

Professor David P. Fenning, Chair
Professor Darren J. Lipomi
Professor Yu-Hwa Lo
Professor Gal Mishne
Professor Shyue Ping Ong

2022

The Dissertation of Rishi Eugene Kumar is approved, and it is acceptable in quality and form for publication on microfilm and electronically.

University of California San Diego

2022

TABLE OF CONTENTS

LIST OF FIGURES

LIST OF TABLES

ACKNOWLEDGEMENTS

First, thank you to Kaylee for your unwavering supporting throughout my PhD journey. I could not have accomplished half of what I did without the solid foundation that you provide in my life.

Second, thank you to David for allowing me to explore over the years we have worked together. Never did I feel limited under your mentorship, whether that be in the ideas we chose to pursue in the lab, or in exposure to the various aspects of academia. Your patience as a teacher and mentor is easy to take for granted, and only in looking back can I begin to appreciate how far I've come under your guidance. I look forward to continuing as collaborators!

Third, I'd like to thank my collaborators who have always treated me with trust, respect, and friendship. In particular, Mariana, Arun, Maria, and Martin; even while I was a first year student, you were all so warm and included me in the process even when I didn't really know what I was doing. I feel lucky to have had such great experiences with external collaborators, and it is this feeling that draws me to stay in academia.

Finally, I want to thank my labmates, past and present. You have collectively fostered an environment of learning and collaboration. Much of my work would ring hollow without your contributions (especially the materials and data you allowed me to play with). I am excited to see where we all end up!

Chapter 2, in part, is a reprint of the material "Quantitative Determination of Moisture Content in Solar Modules by Short-Wave Infrared Reflectometry" as it appears in IEEE Journal of Photovoltaics, Kumar, R. E., Gastrow, G. V., Leslie, J., Meier, R., Bertoni, M. I., and Fenning, D. P. 1748-1753 (2019). The dissertation author was the primary investigator and author of this material.

Chapter 3, in part, is a reprint of the material "Glass vs. Backsheet: Deconvoluting the Role of Moisture in Power Loss in Silicon Photovoltaics With Correlated Imaging During Accelerated Testing" as it appears in IEEE Journal of Photovoltaics, Kumar, R. E., Von Gastrow, G., Theut, N., Jeffries, A. M., Sidawi, T., Ha, A., DePlachett, F., Moctezuma-Andraca, H.,

Donaldson, S., Bertoni, M. I., and Fenning, D. P. 1-8 (2021). The dissertation author was the primary investigator and author of this material.

Chapter 4, in part, is a reprint of the material "Europium Addition Reduces Local Structural Disorder and Enhances Photoluminescent Yield in Perovskite CsPbBr3" as it appears in Adv. Optical Materials, Quinn, X. L., Kumar, R. E., Kodur, M., Cakan, D. N., Cai, Z., Zhou, T., Holt, M. V., and Fenning, D. P. 2002221 (2021). The dissertation author was one of the primary investigators and authors of this material. The dissertation author performed the synchrotron measurements and all data analysis described in this material.

Chapter 5, in part, is a reprint of the material "Accounting for sample morphology in correlative X-ray microscopy via ray tracing," MRS Advances, Kumar, R. E., Quinn, X. L., and Fenning, D. P. (2021). The dissertation author was the primary investigator and author of this material.

Chapter 7, in part, is currently being prepared for submission as "Roboflo: A Job Scheduler for Automated Experimentation Platforms" by Kumar, R. E. and Fenning, D. P. The dissertation author is the primary investigator and author of this material.

Chapter 8, in part, is currently being prepared for submission as "MixSol: Planning Volume Transfers to Reach Arbitrary Mixtures From Stock Solutions with Pipette Constraints and Minimal Waste" by Kumar, R. E. and Fenning, D. P. The dissertation author is the primary investigator and author of this material.

Chapter 9, in part, is currently being prepared for submission as "Robotic High Throughput Screening Identifies Durable Halide Perovskite Absorbers for Tandem Photovoltaics" by Kumar, R. E., Kodur, M., Cakan, Deniz N., and Fenning, D. P. The dissertation author is the primary investigator and author of this material.

VITA

2010-2014 B. S. in Nanoengineering, University of California San Diego

2015-2017 Research Associate, nanoComposix

2017-2022 Ph. D. in Materials Science and Engineering, University of California San Diego

PUBLICATIONS

Kumar, R. E., Kodur, M., Cakan, D. N., Dolan, C. Fenning, D. P. "Robotic High-Throughput Screening Identifies Durable Halide Perovskite Absorbers for Tandem Photovoltaics," (*in preparation*)

Kumar, R. E., Fenning, D. P. "Roboflo: A Job Scheduler for Automated Experimentation Platforms," (*in preparation*)

Kumar, R. E., Fenning, D. P. "MixSol: Planning Volume Transfers to Reach Arbitrary Mixtures From Stock Solutions with Pipette Constraints and Minimal Waste," (*in preparation*)

Kumar, R. E., Tiihonen, A., Sun, S., Fenning, D. P., Liu, Z., and Buonassisi, T. "Opportunities for machine learning to accelerate halide-perovskite commercialization and scale-up," Matter, (2022)

Rigter, S. A., Quinn, X. L., **Kumar, R. E.**, Fenning, D. P., Massonnet, P., Ellis, S. R., Heeren, R. M. A., Svane, K. L., Walsh, A., and Garnett, E. C. "Passivation Properties and Formation Mechanism of Amorphous Halide Perovskite Thin Films," Advanced Functional Materials, 2010330 (2021)

Kim, T., **Kumar, R. E.**, Brock, J. A., Fullerton, E. E., and Fenning, D. P. "How Strain Alters CO2 Electroreduction on Model Cu(001) Surfaces," ACS Catalysis, 6662-6671 (2021)

Kumar, R. E., Von Gastrow, G., Theut, N., Jeffries, A. M., Sidawi, T., Ha, A., DePlachett, F., Moctezuma-Andraca, H., Donaldson, S., Bertoni, M. I., and Fenning, D. P. "Glass vs. Backsheet: Deconvoluting the Role of Moisture in Power Loss in Silicon Photovoltaics With Correlated Imaging During Accelerated Testing," IEEE Journal of Photovoltaics, 1-8 (2021)

Mannodi-Kanakkithodi, A., **Kumar, R. E.**, Fenning, D. P., and Chan, M. K. Y. "First principles modeling of polymer encapsulant degradation in Si photovoltaic modules.," Phys Chem Chem Phys, (2021)

Quinn, X. L., **Kumar, R. E.**, Kodur, M., Cakan, D. N., Cai, Z., Zhou, T., Holt, M. V., and Fenning, D. P. "Europium Addition Reduces Local Structural Disorder and Enhances Photoluminescent

Yield in Perovskite CsPbBr3," Adv. Optical Mater., 2002221 (2021)

Jariwala, S., **Kumar, R. E.**, Eperon, G. E., Shi, Y., Fenning, D. P., and Ginger, D. S. "Dimethylammonium Addition to Halide Perovskite Precursor Increases Vertical and Lateral Heterogeneity," ACS Energy Letters, 2110.11458v1 (2021)

Kumar, R. E., Quinn, X. L., and Fenning, D. P. "Accounting for sample morphology in correlative X-ray microscopy via ray tracing," MRS Advances, (2021)

Kodur, M., **Kumar, R. E.**, Luo, Y., Cakan, D. N., Li, X., Stuckelberger, M., and Fenning, D. P. "X-Ray Microscopy of Halide Perovskites: Techniques, Applications, and Prospects," Advanced Energy Materials, 1-25 (2020)

Li, N., Luo, Y., Chen, Z., Niu, X., Zhang, X., Lu, J., **Kumar, R. E.**, Jiang, J., Liu, H., Guo, X., Lai, B., Brocks, G., Chen, Q., Tao, S., Fenning, D. P., and Zhou, H. "Microscopic Degradation in Formamidinium-Cesium Lead Iodide Perovskite Solar Cells under Operational Stressors," Joule, 1743-1758 (2020)

Kumar, R. E., Gastrow, G. V., Leslie, J., Meier, R., Bertoni, M. I., and Fenning, D. P. "Quantitative Determination of Moisture Content in Solar Modules by Short-Wave Infrared Reflectometry," IEEE Journal of Photovoltaics, 1748-1753 (2019)

ABSTRACT OF THE DISSERTATION

Tools for Data-Driven Investigation of the Durability of Photovoltaics

by

Rishi Eugene Kumar

Doctor of Philosophy in Materials Science and Engineering

University of California San Diego, 2022

Professor David P. Fenning, Chair

I will discuss the development and application of hardware and software tools to study the durability of both standard silicon and next-generation halide perovskite materials for applications in photovoltaics (PV). Progress in PV is stymied by insufficient tooling or methodologies, especially when experiments require various data streams to be merged. I introduce tools developed to mitigate these difficulties, and provide a case studies demonstrating the value of said tools in investigation of the durability of photovoltaic materials.

First, I develop Water Reflectometry Detection (WaRD), the first technique capable of quantitative measurement of water content within standard silicon PV modules. Using WaRD, we dissect various modes of performance loss within the modules that would typically have been

lumped together in module-level studies, quantifying the impact of moisture on two industry-standard types of photovoltaic modules.

Next, I discuss a ray-tracing method to recover spatial correlations in multi-modal benchtop and synchrotron microscopy data of a single sample. In the raw data, these correlations are reduced by the distinct probe-sample interactions and signal collection geometry of each modality. As a demonstrative example we analyze structure-function correlations in sequential microscopy data acquired for a Eu:CsPbBr3 halide perovskite thin-film crystal across three distinct measurement modes.

Finally, I present the Perovskite Automated Solar Cell Assembly Line (PASCAL), a robotic platform for the fabrication and characterization of halide perovskite thin films. PASCAL improves fabrication throughput by two orders of magnitude compared to manual operators, a critical capability given the immense composition and processing design space of halide perovskites. We demonstrate this capability by screening the optoelectronic properties and durability of thin films of 80 unique perovskite compositions in a cumulative 48 hours. This screening provides a roadmap for tailored design of halide perovskite absorbers for perovskite-on-silicon tandem photovoltaics.

Chapter 1

Introduction

1.1 The Levelized Cost of Solar Electricity

Solar energy is a critical component in the sustainable energy infrastructure we require to remove our reliance on finite and polluting fossil fuels. Roadmaps towards a decarbonized worldwide energy infrastructure suggest that photovoltaics will account for anywhere between 20-90% of total energy consumption. Even this large percentage feels small when we consider that our Sun continuously provides our upper atmosphere with 174 petawatts of energy – four orders of magnitude more power than the 18 terawatts consumed worldwide. [1, 2] To harness solar energy and realize our decarbonized future, the penetration of solar in our energy markets must be increased. To this effect, cost reduction is the strongest lever, and most effort in photovoltaic research is ultimately focused on reduction of the cost per unit energy generated by photovoltaic systems. The work contained in this dissertation attack this cost from two sides: making existing photovoltaic modules more durable (ie last longer), and designing next-generation photovoltaic modules with improved power conversion efficiency.

The cost of photovoltaic systems is measured by the levelized cost of electricity (LCOE), or cents per kilowatt hour of power generated by the system. The United States Department of Energy has set an LCOE target of 3 cents/kWh, the path to which relies on cost improvements in all facets of photovoltaics systems (Figure 1.1). [3] The two greatest opportunities for LCOE reduction lie in improvement of the operational lifetime and reduction in the cost of photovoltaic

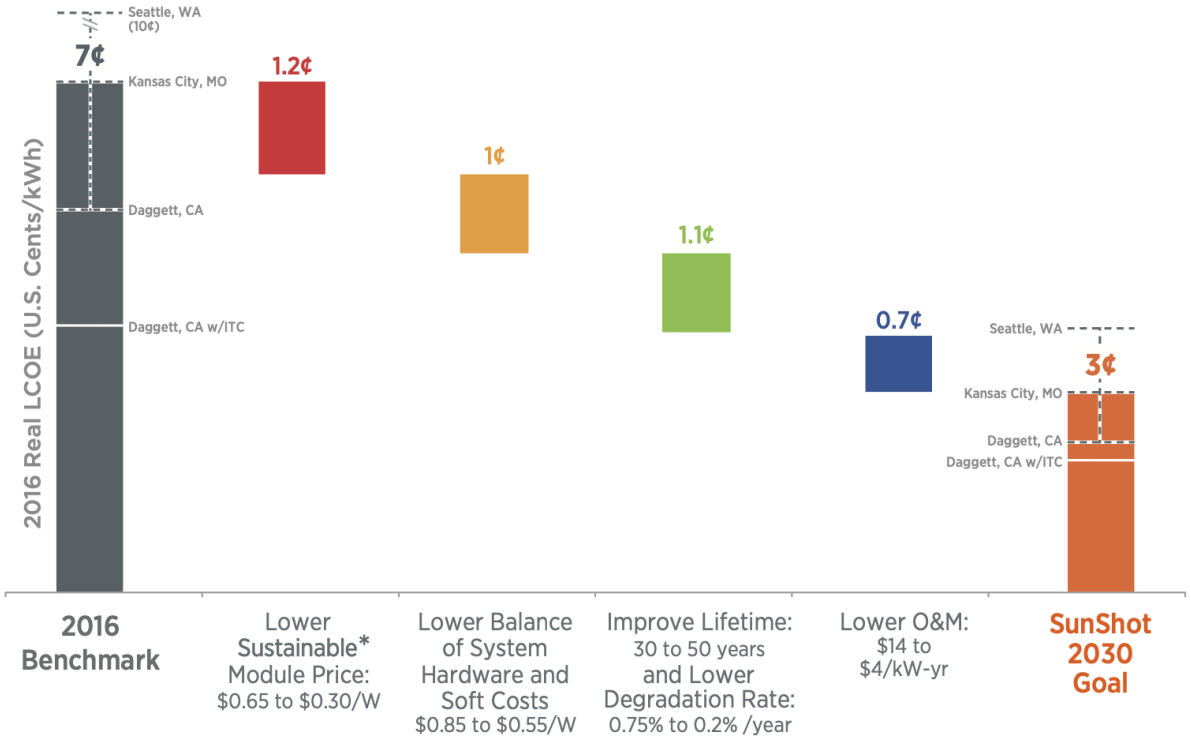

Figure 1.1. Pathway to 3 cents/kWh LCOE for utility-scale photovoltaic systems. [3] The work in this thesis aim at reducing module price (red bar) through development of high-efficiency tandem modules, and at improving operational lifetime (green bar) through understanding of moisture's impacts on module degradation.

modules. The efforts described in this thesis accordingly focus on these two areas.

1.2 Solar Absorbers, Old and New

At their core, photovoltaic cells consist of a semiconductor material in which photons are absorbed to excite electron-hole pairs, which in turn are extracted to pass current to an attached electrical load. A variety of semiconducting materials, referred to as "absorbers", can be used to construct photovoltaic cells. Across all absorbers, however, the same goals of reducing LCOE apply; improving the operational lifetime and power conversion efficiency remain primary objectives in devlopment of any PV absorber.

1.2.1 Silicon

Silicon is the most common photovoltaic absorber, with silicon-based PV making up 95% of those sold as of 2016.[4] Silicon-based photovoltaic technology has seen rapid development since the 1950's; today, silicon modules are the clear incumbent photovoltaic technology, present across rooftops and above parking spaces.[5] The success of silicon PV follows from a few key properties. First, silicon has a bandgap of 1.12 eV, which is near the optimal bandgap for capture of the solar spectrum into electrical power. Second, silicon possesses a long minority carrier diffusion length, with charge carriers within the silicon being able to travel 100-300 microns before recombining. This is a critical parameter, as photoexcited electron-hole pairs are of no value to us if they recombine within the material – energy is extracted by extraction of the carriers at electrical contacts of the PV cell. Third, silicon is the second most abundant element (after oxygen), making the raw material for fabrication of silicon photovoltaics cheap and plentiful. Finally, a great deal of technology, expertise, and infrastructure have been developed around silicon as a semiconducting material owing to its critical role in integrated circuits.

The power conversion efficiency of silicon photovoltaic cells (record of 26.1% at the time of writing) has approached its thermodynamic limits (roughly 30% for silicon, and 33% for any single absorber material), quantified as a function of material bandgap as the Shockley-Queisser limit. [6] The largest remaining improvements to the LCOE of silicon PV systems therefore come in the form of extended operational lifetime. While silicon itself is highly resilient to corrosion and degradation, the overall silicon modules suffer from a variety of degradation modes. This will be discussed in more detail in the introduction to Part I, which focuses on study of moisture-induced degradation of silicon photovoltaic modules.

1.2.2 Halide Perovskites

Halide perovskites are the new kid on the PV block, with the first photovoltaic cell being reported in 2009. [7]. In the following 13 years, the power conversion efficiency of halide

perovskite solar cells has seen a meteoric rise to a record of 25.8% at the time of writing. [8] This rapid success is a result of the tunability and relative ”defect-tolerance” of halide perovskite seminconductors.

Perovskites derive their name from the prototypical ABX_3 perovskite crystal structure [9], the family of materials which largely consists of inorganic oxide perovskites which contain oxygen at the X-site. Halide perovskites instead contain elements from the halogen family at the X-site. The A-, B-, and X- sites can each host a wide variety of elements, both as single species or as mixtures; such variations to the material composition are strong levers on the optoelectronic properties, such as bandgap, of the material. That said, the most successful halide perovskites for PV consist of: a mixture of organic (methylammonium and formamidinum) and inorganic (cesium) cations at the A-site, lead at the B-site, and a mixture of halides (iodine, bromine, and sometimes chlorine) at the X-site. [8, 10]

While the power conversion efficiency of halide perovskite solar cells have surpassed that of silicon with a projected great reduction in manufacturing cost, durability remains the achilles heels of halide perovskite PV. Defects in the perovskite compound over time under exposure to the illumination, electrical bias, and temeperature inherent to operation of photovoltaics. [11, 12, 13, 14] A variety of approaches have been shown for stabilization of halide perovskites, ranging from surface passivation with organic cations to compositional tuning at the A- site. Further background is given in the introductions for Part II and Part III, which focus on our work on halide perovskites.

1.3 Thesis overview

The goal of the research described hereafter is twofold: 1. to understand the factors relevant to durability of photovoltaic absorbers and modules, and 2. to establish and make available the tools (hardware, software, and data analysis frameworks) used to reach this understanding. The discussion is broken into three parts. Each part tackles a problem in photovoltaics research

for which proper study is limited by the existing toolsets. I establish each problem and the related motivation for design of better tools, describe the tools we developed, and demonstrate the tools in case studies.

In Part I, we explore the role of water in the degradation of silicon photovoltaic modules with an emphasis on improving operational lifetime. Moisture ingress has been implicated as a contributor to a variety of degradation pathways in silicon modules. Prior to our work, however, the actual amount of water within modules was often a hidden variable. Quantitative measurement of moisture content had relied on custom-fabricated modules or extrapolation from measurements of individual module components. We developed an optical method for quantification of water content within standard silicon modules, and designed hardware to spatially resolve this water content within modules at high resolution. Armed with this capability, we correlated local water content to local degradation within solar modules. Our study isolates the contributions of distinct water-induced degradation modes on module-wide power losses.

In Part II, we study the interplay of material structure, composition, optoelectronic behavior, and durability within a doped perovskite microcrystal using a combination of benchtop and synchrotron-based characterization techniques. Each individual technique provides a new, spatially-resolved dimension over which to evaluate the material. A simple pixel-to-pixel comparison across the data generated by each technique is not possible as the data are convoluted by unique factors arising from the physical mechanisms and the measurement geometry of each technique. We establish a ray-tracing approach to recover the effective sampling volume of each technique. Using these sampling volumes, we align the modalities to perform a faithful correlation of the total data. This method, demonstrated on a study of europium doping in $CsPbBr_3$ perovskite, provides a general approach to account for sample-probe interactions in scanning probe microscopy.

In Part III, we build the Perovskite Automated Solar Cell Assembly Line (PASCAL), an automated experimentation platform which we use to explore a wide span of halide-perovskite absorber compositions. The robotic platform improves experimental throughput and process

precision, allowing for a broad screening experiment in spite of the narrow processing windows presented by halide perovskites. In the process of building PASCAL, I developed software tools that solve general problems in the deployment of automated experimentation platforms. MixSol plans sequences of volume transfers to reach desired mixtures of stock solutions with zero waste volume, a common step in design of solution-based experiments. Roboflo computes job schedules for batches of experiments that require sequences of time-sensitive steps to be executed on a heterogeneous set of hardware resources. PASCAL is demonstrated in a screening experiment, in which ˜80 unique halide perovskite absorber compositions are fabricated and characterized in under 48 hours. The screening results provide a roadmap for development of halide perovskite solar cells in perovskite-on-silicon tandem photovoltaic modules.

Part I

Water in Silicon Photovoltaic Modules

Water is implicated in the degradation of photovoltaic modules by facilitating delamination at interfaces [15], decreasing power output under potential-induced degradation testing conditions [16], hydrolyzing encapsulants [17], enabling cation migration [18], increasing series resistance via contact corrosion [19, 20], and reducing light absorption in the cell due to scattering effects [21, 22]. Although the negative effects of water have been inferred via performance degradation metrics, no method is in use for *directly observing water and its effects across the full area of a standard module*. This inability to characterize moisture in standard modules in the lab or in the field limits our understanding of module degradation mechanisms and hinders efforts to engineer modules with extended reliability in humid environments.

Previous works have established methods for determining water content in either standalone solar encapsulants or in purpose-made test modules. Infrared imaging techniques have been demonstrated for moisture detection in photovoltaic materials, though they either rely on transmission measurements (and are thus inapplicable in modules) or remain qualitative [23, 24, 25]. Fourier-transform infrared spectroscopy (FTIR) and infrared transmission measurements have been used to determine water content in solar encapsulants laminated between two glass sheets, yielding quantitative data on moisture capacity and diffusivity of various encapsulants.[26, 25] These transmission-based techniques are limited to use in test modules constructed without solar cells. Raman spectroscopy has been used to detect degradation products in ethylene vinyl acetate (EVA) encapsulant in a module. [27] While this method can imply the presence of water in degraded areas, it is unable to quantify the amount of water present in the module. Implanted humidity sensors have provided direct measurement of water content in test modules, though the invasive nature of this technique makes it untenable in fielded modules.[28, 29] Additionally, the spatial resolution of module moisture measurement by humidity sensors is inherently low, as it is limited by the number of sensors implanted within the module. Finally, many previous studies of water in modules use finite element models to simulate moisture ingress into modules under various environmental conditions.[30, 31] As our understanding of the importance of moisture dynamics in solar encapsulant grows, so does the

need for direct measurement of moisture in modules during normal operation.

Most studies of moisture effects on silicon PV durability fall under one of two categories - macroscopic studies of entire modules under accelerated or outdoor testing, or *ex-situ* testing of module components under conditions designed to simulate humidity exposure in the field. Macroscopic studies often track the current-voltage (IV) characteristics in conjunction with one or more imaging modalities to provide insight to local module degradation mechanisms during environmental exposure. These modalities include photoluminescence to identify electronic defects in cells, electroluminescence for crack detection, infrared thermography for hot-spot detection, and ultraviolet fluorescence imaging to observe encapsulant degradation [32, 33, 34, 35]. Such correlative studies are lacking for module moisture content, which has remained a largely hidden variable due to difficulty of measurement.

Ex-situ study of module components has been used to evaluate moisture affects in more easily controlled environments where water content can be assessed. Encapsulants are among the most heavily studied components, and the diffusivity and solubility of water, decomposition mechanisms, and mechanical properties of standard materials are well understood [36, 17, 37, 38, 39]. These values are used to simulate moisture effects on module durability, including ethylene vinyl acetate decomposition, moisture uptake rates, and predicted module performance[40, 36, 16, 41, 42, 43]. Investigation of this kind are attractive for their rapid cycle of learning (relative to the $\geq$2000 hours typical of aging experiments), but cannot easily capture combined effects that may arise in operating conditions.

We address these challenges by developing an improved method for measurement of water content in standard modules. In Chapter 2, we present Water Reflectometry Detection (WaRD), a method for determination of water content in standard modules by short-wave infrared (SWIR) reflectometry which allows for direct measurement of modules in the laboratory and in the field. We describe the method and its limitations, and show that it can be used for spatial measurement of water content within a standard silicon photovoltaic module. In Chapter 3, we use WaRD in conjunction with Photoluminescence-IV (PLIV) imaging to correlate local

water content to local performance losses in representative photovoltaic modules subjected to a variety of environmental test conditions. Specifically, we track water and performance in the two industry-standard module designs (glass-glass and glass-backsheet configurations) over up to 3000 hours of aging in temperatures and humidities ranging from room conditions to the industry standard of 85°C, 85% relative humidity. While water does reduce the overall power output of both module types, the mechanisms by which moisture drives cell degradation are seen to vary between module type (cells in glass-glass modules crack in dry locations, cells in glass-backsheet modules develop series resistance in wet locations). This conclusion could not be reached without spatial quantification of water content, demonstrating the value of WaRD in durability studies of photovoltaic modules.

Chapter 2

Quantitative Determination of Moisture Content in Modules by Short-Wave Infrared Reflectometry

2.1 Introduction

Here, we demonstrate quantitative determination of water content in standard modules by short-wave infrared (SWIR) reflectometry, allowing for direct measurements of modules in the laboratory and in the field. Water has a distinct absorption band in the SWIR region due to a linear combination of lower energy vibrational modes. [44] The encapsulants, anti-reflection coating, and silicon cell in a typical module are largely transparent in this same optical region, providing a window to clearly observe water's optical signature. Additionally, the existing back reflector of a solar cell is highly reflective in this region, allowing the reflected component of an incident SWIR beam from the front side of a module to transmit twice through the encapsulant layer. A calibrated Water Reflectometry Detection (WaRD) model for SWIR determination of water content in both aluminum back surface field (Al-BSF) and passivated emitter rear contact (PERC) modules is presented. Validation of WaRD is based on reflectance data from miniature modules exposed to environments ranging from room condition to the standard 85°C, 85% relative humidity (RH) accelerated test condition (schematic shown in inset of Figure 2.1).

To establish the water content in moisture-exposed modules, we first parametrize the

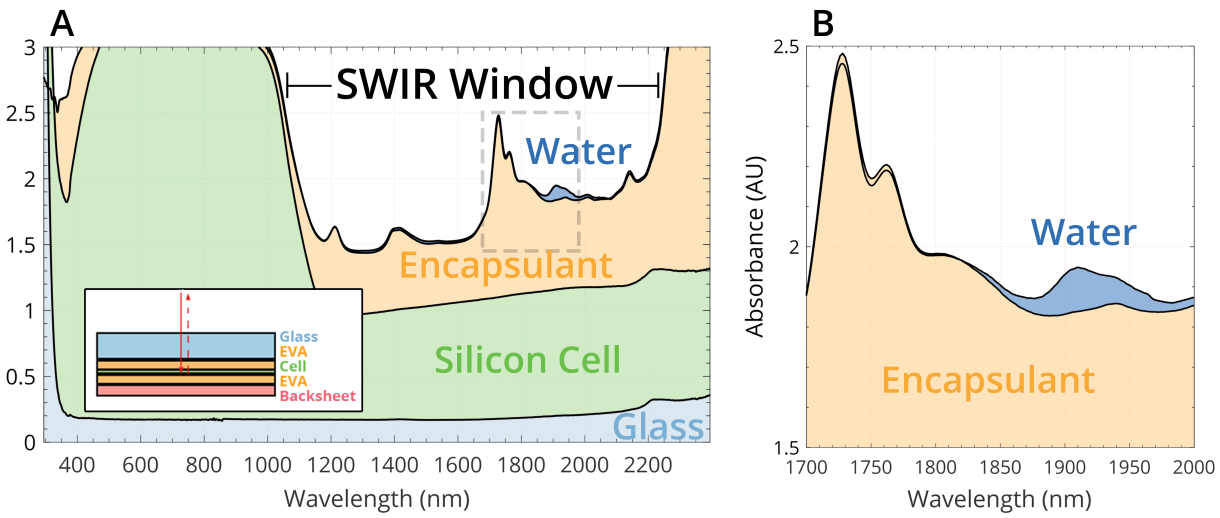

Figure 2.1. Mini Module Schematic: A schematic of miniature modules used for development of the Water Reflectometry Detection (WaRD) method is shown in the inset. The optical path (shown in red) makes two passes through the top glass, top encapsulant layer, and the cell itself due to strong reflectance at the cell's back contact. No light is transmitted through the module. (a) The absorbance contributions of each module component between 250-2300 nm. The glass and silicon cell absorb strongly in the ultraviolet and visible regions, leaving an optical window in the short-wave infrared region by which encapsulant and water absorption features can be detected. (b) The attribution of SWIR absorbance present in an EVA-encapsulated PERC module saturated at 85°C, 85% relative humidity. Attributions are based on optical measurements of each layer. The region of (a) shown more closely in (b) is marked as a dashed rectangle.

Table 2.1. Parameters for Water Diffusivity and Solubility in Solar Encapsulants

	Cybrid POE-T	3M EVA9100	EVA from 2005 [45]
E_a (eV)	0.028±0.259	0.190±0.080	0.398±0.045
D_o (cm^2/s)	$4.93 \times 10^{-6} \pm 1.23 \times 10^{-4}$	$1.32 \times 10^{-3} \pm 6.18 \times 10^{-2}$	$2.46 \pm 1.90 \times 10^{-1}$
ΔH_{sol} (eV)	0.110±0.021	0.194±0.020	0.170±0.034
C_o (g/cm^3)	0.033±0.495	2.226±0.498	1.612±0.286

diffusivity and solubility of water in contemporary encapsulants. We then expose miniature modules to various damp heat conditions until the encapsulant moisture content reaches saturation. The front-side module reflectance in the wavelength range of 1700-2000 nm is taken of samples at each saturation condition. This dataset is used to form an empirical relationship between encapsulant water content and module reflectance, which is shown to match the expected relationship theoretically based on water's infrared absorption. The resulting calibration curve enables module water content measurement with a detection limit of 0.066 mg/cm^3 and a prediction error of 0.130 mg/cm^3. In the case of EVA encapsulant, this detection limit corresponds to extremely dry climates ranging from 4-6% relative humidity at temperatures between 25-40 °C.

2.2 Experimental

2.2.1 Diffusivity and Solubility of Water in Encapsulants

Parameterization of the diffusivity and saturation concentration of water in contemporary encapsulants was done by a gravimetric study of water uptake in standalone encapsulant samples. Two commercial encapsulants were tested - 3M EVA9100 ethylene vinyl acetate (EVA), and Cybrid POE-T polyolefin (POE). Multiple sheets of solar encapsulant were vacuum laminated under standard conditions (1 atm at 145°C) to form 2.3 mm thick samples of cured encapsulant. Samples were saturated in varied temperature and relative humidity conditions, controlled by

either an environmental test chamber or a water bath. Samples were periodically removed from the environment, cooled to room temperature, dried, and weighed. Mass changes incurred due to water uptake as a function of time were fit to determine the diffusivity and solubility of water in the cured encapsulant according to Equation 2.1.

$$C(x,t) = C_s - \frac{4C_s}{\pi}\sum_{m=0}^{\inf}\frac{1}{2m+1}\sin\frac{(2m+1)\pi x}{l_{enc}}e^{-\frac{D(2m+1)^2\pi^2 t}{l_{enc}^2}} \tag{2.1}$$

Equation 2.1 is a 1-D diffusion model assuming no initial concentration of water in the encapsulant, equilibrium water concentration C_s at the faces of the encapsulant sheet in the bath, encapsulant layer thickness of l_{enc}, and neglible diffusion from the edges (thickness $<<$ width). Solubility was calculated by the mass increase between the dry and saturated encapsulant samples.

The equilibrium water content in the encapsulant is dependent on the partial pressure of water vapor, which was controlled by environmental temperature and relative humidity. First, a vacuum oven was used to fully remove water from modules. Environmental test chambers were employed to control the damp heat conditions for saturation of our miniature modules. Tested environmental conditions ranged from 23-85°C and 0-85% relative humidity. Encapsulated samples were kept in the environmental chambers until reaching 99.5% saturation water content as determined by Equation 2.1).

2.2.2 Optical Testing

SWIR reflectance measurements were performed on miniature (3 cm by 3 cm) EVA9100-encapsulated modules (schematic shown in inset of Figure 2.1) with both passivated-emitter rear contact (PERC) and aluminum back surface field (Al-BSF) cell architectures. Two module structures were used - ”mini-modules”, which follow the typical module structure with a top

glass layer (borosilicate glass purchased from McMaster-Carr) and a bottom backsheet layer (Protekt HD purchased from Madico), and ”open-face modules”, with no top glass (the top encapsulant layer is exposed) and a bottom glass layer. Reflectance was measured on a Perkin Elmer Lambda 1050 spectrophotometer using a 150 mm Spectralon integrating sphere and a Spectralon reflectance standard. Samples were oriented such that the beam is incident upon the top glass and is normal to the sample surface. Sample reflectance was measured at both room temperature and the temperature used during damp heat exposure. The elevated temperature was employed to avoid observed optical effects from condensation of water within the module as described below.

SWIR reflectance and transmission measurements were made of the individual module components. The absorbance of EVA was determined at various temperatures via reflectance measurement of an EVA9100 film laminated onto an aluminum mirror. Finally, SWIR reflectance measurements of 3M EVA9100, Cybrid POE-T, and 3M EVA9110 (another commercial ethylene vinyl acetate solar encapsulant) laminated on mirrors were taken at vacuum dry and 85°C 85% RH saturated conditions as a proof of concept for water reflectometry detection in other encapsulants.

2.3 Results and Discussion

2.3.1 Diffusivity and Solubility of Water in Encapsulant

Our measurements for the diffusivity and solubility of water in contemporary EVA are compared to those from previous work testing EVA from 2005 Figure 2.2. [45] EVA9100 holds about 40% less water than EVA of 2005, but has a slightly higher solvation enthalpy. Water diffusivity is higher in contemporary EVA for temperatures below ˜50°C. As expected, water solubility is found to be lower in POE than in EVA, reflecting the difference in polymer chemistries. EVA contains polar vinyl acetate groups, whereas POE consists entirely of nonpolar hydrocarbon chains. Water shows higher diffusivity in POE compared to all EVA formulations

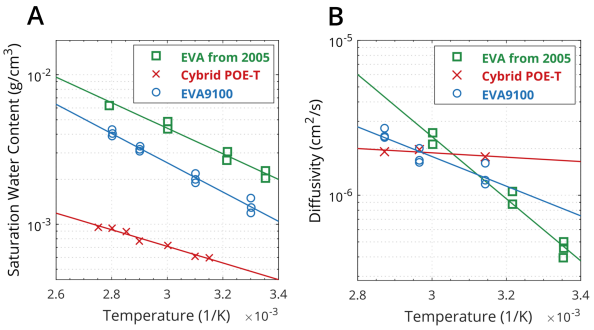

Figure 2.2. Solubility and Diffusivity of Water in EVA: (a) Solubility and (b) diffusivity of water in EVA9100, Cybrid POE-T, and an EVA formulation from 2005 [45]. The water diffusivity and solubility in EVA9100 and Cybrid POE-T were determined by gravimetric measurement of water uptake in standalone encapsulant samples. Fitting parameters for solubility and diffusivity in the three encapsulants are given in Table 2.1

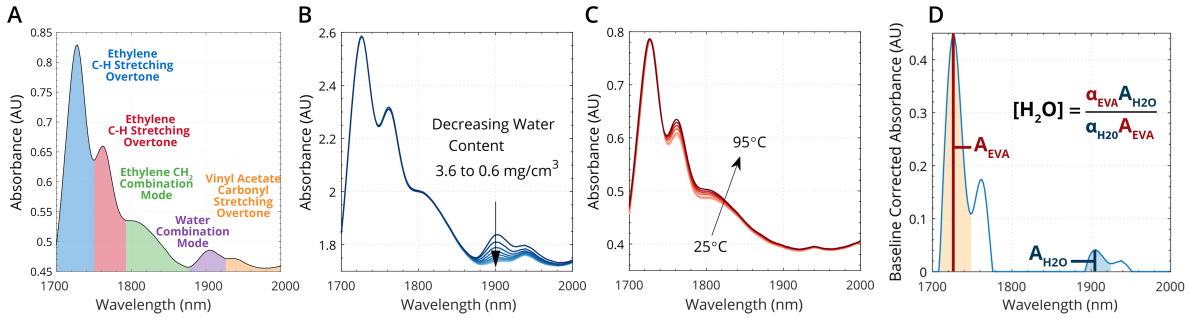

Figure 2.3. Optical Signature of Water in EVA: The water and EVA absorption features of interest in a module containing water are labeled in (a). The absorption spectra of an EVA9100-laminated PERC module previously saturated with water at 85°C85% RH equilibrating to room conditions are shown in (b). As the water concentration decreases due to outdiffusion, only the ˜1902 nm water combination band is affected, decreasing proportionally to module water content. The effect of temperature on the absorbance of EVA9100 is shown in (c). The ˜1902 nm water combination band and the ˜1730 nm EVA C-H stretching overtone are invariant with temperature, making them reliable features to rely on across relevant test conditions. After baseline removal from the absorbance spectrum, the ratio of these peaks is used to quantify module water content (d).

for temperatures below ˜60°C. Fitted Arrhenius parameters for water diffusivity and solubility in these materials are given in Table 2.1.

2.3.2 Spectral Analysis

Figure 2.1 shows the absorbance contributions of individual module components to the total absorbance in a front-side total reflectance measurement between 250-2300 nm. The silicon cell, of course, shows strong absorbance in the visible region, while the top glass shows strong absorbance in the ultraviolet and infrared regions. The encapsulant itself (EVA9100, in the case of 2.1), has pronounced absorption features in the 1200-2200 nm region. Liquid water has two absorption features in this optical region, located at 1450 nm and 1940 nm. [46] In the case of water contained within EVA, we observe a water absorption feature at 1902 nm. Transmission measurements of module components show that no light in the 250-2300 nm optical region is transmitted through either a PERC or Al-BSF cell. This implies that any incident light not reflected back to the integrating sphere has been absorbed within the module. A front-side module reflectance measurement, therefore, is equivalent to a transmission measurement making two passes through the glass, top encapsulant layer, and silicon absorber, enabling the conversion of reflected intensity to absorbance by Beer-Lambert's law (Equation 2.2).

Absorption features of water and the encapsulant are isolated from any broadband optical features by baseline subtraction. These broadband optical features - namely, those from absorbance in the glass, absorbance in the cell, and refractive index mismatch at interfaces - are essentially flat in the 1700-2000 nm range as shown in Figure 2.1(a). The subtracted baseline is estimated by smoothing the absorbance spectrum with a 102 nm wide first-order Savitsky-Golay filter. [47] This subtraction isolates absorbance changes due to water uptake, and removes architectural dependence on the absorption spectrum.

$$A = -log(R) \tag{2.2}$$

Figure 2.3(a) shows assignment of the absorption features for EVA and water in the

1700-2000 nm range. These are the strongest features present within the module reflectance SWIR window and are used to determine the amount of water within the encapsulant, and include Figure 2.3(b) shows absorbance spectra for an ”open-face” (no top glass) EVA9100-laminated PERC module with various water concentrations. The ”open-face” module was brought to a water-saturated state by environmental conditioning at 85°C 85%RH, then optically measured at room conditions over time. Due to the lack of top glass, the water content in the encapsulant continually decreases due to outdiffusion until the equilibrium water content of the room condition has been reached. The influence of water content on front-side module SWIR reflectance is clearly isolated to 1850-2000 nm. This spectral region contains a combination band (1902 nm) from water and a vinyl acetate carbonyl stretching overtone (˜1940 nm) from the EVA encapsulant.[44, 48] As expected, the absorbance at the water combination band is positively correlated to module water content (Figure 2.3(b)). The strength and position of the 1720, 1760, and 1830 nm absorption features are unchanged with varied water content. These features are attributed to higher order C-H and C-H_2 vibrational modes in the nonpolar ethylene units of EVA, which should not exhibit strong interaction with any neighboring water molecules. Therefore, it is unsurprising that these features are unaffected by water content. The carbonyl group of the vinyl acetate, being prone to hydrogen bonding with water, is affected by water in the encapsulant. [49, 50]

The front-side reflectance signal is also affected by module temperature. Measurements of dry EVA9100 at various temperatures are shown in Figure 2.3(c). The absorption intensities for two ethylene vibrations (1760 nm C-H stretching overtone and 1830 nm combination band) are seen to increase with temperature. The 1730 nm ethylene C-H streching overtone, the 1940 nm vinyl-acetate carbonyl stretching overtone, and the 1902 nm water combination band region are unchanged with temperature. The difference in temperature-dependent behavior between the two C-H stretching overtone peaks may arise from the mix of amorphous and crystalline phases within the EVA. Ethylene groups within EVA exist in both amorphous and orthorhombic crystalline phases, while vinyl acetate groups only exist in amorphous states.[51] Bonds within

crystalline regions will experience a gradual change in vibrational freedom with increasing temperature due to partial melting of smaller, less stable crystalline domains, and should exhibit a change in absorbance behavior as a result. Prior work confirms this temperature-dependent absorbance behavior in polyethylene. [52, 53] The temperature-sensitive absorption bands can therefore be associated with the degree of crystallinity of the encapsulant.

In the context of SWIR water detection, the features of interest are the C-H stretching overtone at 1730 nm and the water combination band at 1902 nm - these spectral regions display consistent behavior across the relevant range of environmental conditions and provide a robust basis for quantifying water content in modules.

By Beer's Law, the magnitude of the water absorbance, A_{1902}, is directly proportional to the concentration of water in the optical path, which consists of two passes through the glass, top encapsulating layer, and solar cell. To determine the water concentration, the optical path length must be accounted for. Given that water is insoluble in the glass and cell, the relevant optical path length for water absorption is taken to be twice the encapsulant thickness, t_{enc}. This is also the relevant path length for the 1730 nm encapsulant absorption feature, A_{1730}, the magnitude of which is proportional to the encapsulant thickness. By taking the ratio of water absorbance to encapsulant absorbance, the effect of path length on absorbance can be removed without prior knowledge of the encapsulant thickness. This treatment (Equation 2.3) yields a value proportional to the water concentration (g/cm^3) in the encapsulant by a constant factor of the ratio of feature absorption coefficients, which can be accessed from the literature or calibrated in test samples.

$$
\begin{aligned}
A_{1902} &= \alpha_{1902}[H_2O](2t_{enc}) \\
A_{1730} &= \alpha_{1730}(2t_{enc}) \\
[H_2O] &= \frac{\alpha_{1730}A_{1902}}{\alpha_{1902}A_{1730}}
\end{aligned}
\tag{2.3}
$$

2.3.3 WaRD Calibration and Detection Limits

Figure 2.4(a) shows the calibration curve for WaRD, relating the ratio of the 1730 nm EVA and 1902 nm water absorption features to the module water concentration as determined by Equation 2.3. Each point contains measurements of 6-12 modules, half PERC and half Al-BSF. The performance of WaRD is consistent across the investigated module architectures and environmental conditions, with sample to sample variation of ± 0.095 mg/cm^3. The accuracy, as determined by the root mean squared error, is 0.130 mg/cm^3. The detection limit, as defined by 3.3 times the instrumental noise, is 0.066 mg/cm^3.[54] Figure 2.4(b) shows the saturation water water concentration in EVA9100 as a function of temperature and relative humidity. WaRD is demonstrated for water concentrations representative of climate conditions ranging from extreme terrestrial conditions, such as the Atacama Desert and Singapore, to the standard 85°C, 85%RH test condition.

We observe optical effects from water condensation within modules conditioned at high temperature and humidity but measured at room temperature and humidity. When the module temperature is brought sufficiently below that of its previous environmental condition, the water in the supersaturated encapsulant condenses into water droplets within the module. This effect can be seen visually when edge-illuminating a module with condensation, as light scattering from the condensed water droplets will generate a hazy appearance (Figure 2.4(c)). The red points in Figure 2.4(a) represent measurements of high water content $>$2g/cm^3) modules taken at room

conditions, and demonstrate the effect of condensation on WaRD. When the same modules are measured at their saturation temperature (blue points), the WaRD-extracted water concentration matches the expected value. Upon cycling the temperature of a highly saturated module between room temperature and the saturation temperature, the water content measured by WaRD will decrease during cooling and increase during heating due to condensation and dissolution of water within the encapsulant. An example of this is seen in Figure 2.4(d), in which a module saturated at 85°C, 85% RH was subsequently measured at 10°C intervals while first cooling from 85°C to 35°C, then reheating to 85°C. Samples were held at each temperature for 5 minutes before measurement. The effect of temperature on WaRD is completely reversible, suggesting that condensation within the encapsulant is reversible and kinetically favorable enough to occur on the timescale of minutes.

The deviation between red and blue points in Figure 2.4(a) sets a maximum water concentration when applying WaRD at room temperature: above expected water concentrations of ~2 mg/cm^3, the module must be measured at elevated temperature to generate an accurate value for water content. In practice, this limit will only be passed in aggressive laboratory damp heat testing, as can be seen in Figure 2.4(b). Even at the highest recorded terrestrial dew point (35°C in Dhahran, Saudi Arabia on July 8, 2003), module water content would be below ~2 mg/cm^3. [55] When testing EVA-encapsulated modules above 65°C, 65% RH should be carried out at the saturation temperature to avoid condensation effects. At higher temperatures, light scattering from water condensation must be considered. Preliminary results show that modules saturated at 85°C 85%RH display an increased visible light reflectance when measured at room temperature instead of the 85°C saturation temperature, suggesting that light scattering from water condensation may reduce the short circuit current of damp heat tested modules by up to 3%.

2.3.4 Spatial Mapping of Module Water Content

The WaRD method can be adapted to a mapping setup, enabling spatial quantification of water content across a module. An example map is shown in Figure 2.5(b) and compared to the expected concentration profile generated by finite element modeling of moisture indiffusion into the module using the previously parametrized diffusivity and solubility values for EVA9100 (Figure 2.5(a)). The 3 cm by 3 cm EVA9100-encapsulated PERC module was exposed to 85°C, 40% relative humidity for 18 hours after being kept dry in a vacuum oven. The measured concentration profile mirrors the expected profile quite closely, both in the position of the indiffusion front and the range of water concentrations present across the module.

2.3.5 WaRD Feasibility in Other Encapsulants

The WaRD method should, in principle, be applicable to any encapsulant material that satisfies two criteria. Firstly, the encapsulant should not have any strongly overlapping absorption features with the water absorption feature of interest, ensuring that any change in absorbance due to water can be clearly observed. Secondly, the encapsulant should have a characteristic absorbance that is stable across the relevant range of temperatures and water contents by which the optical path length can be estimated. While WaRD has been validated using 3M EVA9100, preliminary measurements of dry and water-saturated 3M EVA9110 and Cybrid POE-T have been made to probe their absorbance behavior. Laminated samples of each encapsulant were either dried under vacuum at 50°C or saturated in a water bath at 85°C before optical measurements were taken (Figure 2.6). The dry and saturated measurements show distinct absorption at the water combination band with the 1730 nm C-H overtone remaining constant. Thus, 3M EVA9110 and Cybrid POE-T satisfy the two criteria laid out above, indicating that WaRD can be applied to these encapsulants as well. Water content quantification in polyolefins is more difficult simply due to their low moisture capacity (Figure 2.2(a), though this can be addressed by purpose-built hardware.

2.4 Conclusion

WaRD provides quantitative in situ measurement of water content within EVA encapsulated PERC and Al BSF modules with a prediction error of 0.130 mg/cm^3 and a detection limit of 0.066 mg/cm^3. This ability is demonstrated across the relevant space of water concentrations, covering terrestrial conditions and the standard 85°C, 85% relative humidity test condition. While the technique has been demonstrated in EVA encapsulant, the principle should be generalizable to many other encapsulants. WaRD measurements have also revealed the optical effects of condensation within moisture-exposed modules. After standard 85°C, 85% relative humidity damp heat tests, condensation in the encapsulant leads to light scattering, presenting a source of up to 3% error in short circuit current measurements after accelerated testing of modules. Finally, WaRD enables quantitative mapping of water content across the module area. Spatial resolution of water content in modules opens the door for correlated study of local water content and module performance, and will enable direct study of the role water plays in module degradation.

2.5 Acknowledgements

Chapter 2, in part, is a reprint of the material "Quantitative Determination of Moisture Content in Solar Modules by Short-Wave Infrared Reflectometry" as it appears in IEEE Journal of Photovoltaics, Kumar, R. E., Gastrow, G. V., Leslie, J., Meier, R., Bertoni, M. I., and Fenning, D. P. 1748-1753 (2019). The dissertation author was the primary investigator and author of this material.

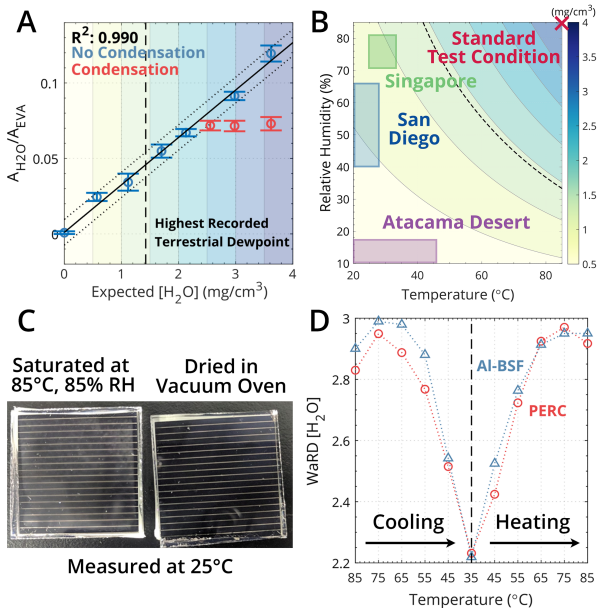

Figure 2.4. WaRD Calibration Curve: The calibration curve for converting the ratio of water and EVA absorption intensities to module water concentration is shown in (a). The calibration trend is linear as predicted by Equation 2.3. The expected saturation water concentration as a function of environmental condition is shown in (b). along with representative climates and test conditions. The two figures share contour lines demarking water concentration in 0.5 mg/cm^3 intervals, as well as a dashed line indicating the equilibrium water content expected in EVA at record terrestrial conditions. Samples for which condensation was observed either visually or spectrally are shown in red in (a), and are not included in the calibration fit line. These samples were measured at room condition, such that the encapsulant is sufficiently supersaturated for water droplets to nucleate within the encapsulant. (c) demonstrates visible condensation in a room-temperature mini module that had been saturated at 85°C, 85% RH. The haziness is not present in an identical sample that had been kept under vacuum to remove any water content from within the encapsulant. (d) shows the effect of condensation on the water content measured by WaRD. The front-side reflectance of the saturated mini module pictured at left in (c) was measured at a series of temperature ranging between the saturation temperature (85°C) and near room temperature (35°C). The measured water content returns to the expected value upon return to the saturation temperature.

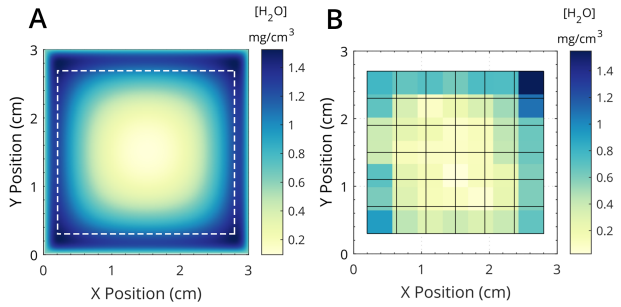

Figure 2.5. First WaRD Map: The expected water concentration profile in a 3 cm by 3 cm area EVA-encapsulated PERC module after 18 hours exposure to 85°C, 40% RH is shown in (a). (b) shows the actual concentration profile in a test module exposed to the modeled environmental condition, measured by applying the WaRD method in a 7 by 7 grid across the module (indicated by the plotted grid's intersection points. Values could not be taken at the edges of the cell due to the large ˜1 cm spot size of the integrating sphere used for mapping. The area mapped in (b) is indicated in (a) by the white dotted line.

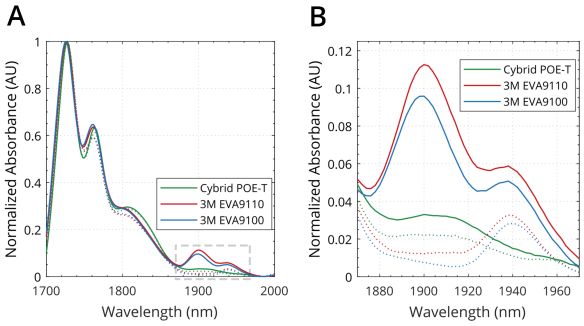

Figure 2.6. WaRD Signal in Various Polymeric Encapsulants: (a) The absorbance curves of 3M EVA9100, 3M EVA9110, and Cybrid POE-T encapsulants are shown. Samples were measured in both dry (dotted line) and saturated (solid line) states. Dry states were achieved by drying in a vacuum oven at 50°C, while saturated states were reached in an 85°C water bath. (b) The same data is shown, focused on the spectral region containing the 1902 nm water absorption feature. The region shown in (b) is marked in (a) by the dashed rectangle.

Chapter 3

Glass vs Backsheet: Deconvoluting the Role of Moisture in Power Loss in Silicon Photovoltaics with Correlated Imaging during Accelerated Testing

3.1 Introduction

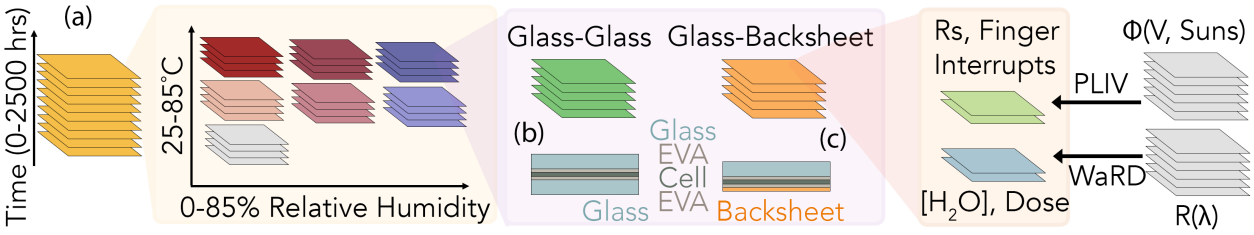

Figure 3.1. Spatially-resolved damp heat workflow: (a) Schematic of the data flow in our study. Each square represents a single spatially-resolved dataset. Local cell parameters and moisture content are tracked for (b) glass-glass and (c) glass-backsheet modules at a range of temperatures and humidities across 2500 hours of environmental exposure

Having established that we can accurately measure water content inside standard silicon photovoltaic modules using WaRD (Chapter 2), we applied WaRD to evaluate the impact of local water content to local performance losses. We combine WaRD with biased photoluminescence imaging to correlate local water content to local cell degradation at millimeter resolution [56, 57]. The water concentration and performance of modules with glass-glass (GG) and glass-backsheet (GB) bills of material (BOM) were tracked over 2500 hours of accelerated testing in conditions

ranging across 25-85 °C and 0-85% RH. We find two dominant modes of performance loss, each involving local series resistance - acute interruption of finger connections, and "background" series resistance increase. Each mode shows a unique response between module types and varied sensitivity to moisture. The interrupts, many of which are confirmed to be cracks, are most prevalent in GG modules in dry conditions. Background resistance increases significantly more in GB modules than in GG modules at high humidity levels, suggesting moisture-induced degradation of the cell's back contact. Our results suggest that in dry conditions, GB modules are preferred for their low rate of finger interruption, while in humid climates, GG modules are preferred to mitigate background series resistance losses.

3.2 Experimental Methods

3.2.1 Sample Preparation

All tests are performed on 4.9x4.9 cm mini-modules made with silicon aluminum back surface field cells (Shenzhen Taihesheng Solar Energy Co., Ltd.). The cells are encapsulated into either glass-glass or glass-backsheet modules (Madico Protekt backsheet), which vary only in the bottom layer of the module stack (schematics in Figure 3.1b-c). All modules are laminated with ethylene vinyl acetate (3M EVA9100) at 145 °C for 18 minutes.

Backsheet Ingress Sister Samples

Sister GB modules were fabricated with the cell replaced by strips of aluminum foil spaced 10 mm apart. This allowed us to measure moisture concentration through the front glass at the edge of the foil strips (using the Water Reflectometry Detection method as described below), where the relevant diffusion path for moisture is directly through the backsheet. These sister modules were saturated with water at 85 °C, 85% RH. Their water content was then mapped at 45 minute intervals over 48 hours while being held at 85 °C in room conditions.

Samples for Study of Metallization Corrosion

Sister GB modules were fabricated with a strip of polytetrafluoroethylene (PTFE) embedded at the edge of the sample between the front of the cell and the EVA layer. This PTFE allows us to selectively delaminate the front cell/EVA interface with a 180°peel (0.5 kN Instron load cell), exposing the front of the cell for testing.

3.2.2 Damp Heat Accelerated Tests

62 mini-modules are each subjected to one of seven environmental conditions - 0, 40, or 85% relative humidity (RH) at 65 or 85 °C, or 0% RH at 25 °C (Table 3.1. Dry environments were maintained in either a nitrogen glovebox (0% RH) or a desiccator constantly purged with dry air ($\leq$3% RH). Samples are held in their environment for up to 3000 hours. Each module is characterized by a suite of techniques *ex-situ* weekly until 2184 hours (13 weeks), after which they are measured every other week.

Table 3.1. Mini-Module Samples Studied Under Damp-Heat Testing

Packaging	Temp. (°C)	Rel. Humidity (%)	# Samples
Glass-Backsheet	25	0	2
	65	0	3
		40	5
		85	5
	85	0	4
		40	5
		85	5
Glass-Glass	25	0	3
	65	0	4
		40	6
		85	6
	85	0	4
		40	5
		85	5

3.2.3 Current-Voltage Measurement

Standard current-voltage (IV) measurements are taken in a four-wire configuration under 1-sun illumination (Class ABA Newport solar simulator using either a Kepco BOP 20-20D-4866 or Keithley 2401).

3.2.4 Spatial Quantification of Module Moisture Content

We use Water Reflectometry Detection (WaRD) to quantify the water content within a module's front-side encapsulant layer by short-wave infrared (SWIR) reflectance [56]. Maps of module SWIR reflectance were taken with a mapping spectrophotometer consisting of a tunable laser (NKT Photonics Compact and Select), translation stages (Thorlabs LTS150), integrating sphere (Thorlabs IS200), InGaAs detectors (Thorlabs PDA10DT), and a lock-in amplifier (Stanford Research Systems SR830). Maps are acquired with 1 or 2 mm steps. All samples are measured in room conditions except those exposed to 85 °C, 85% RH, which are heated to 85 °C during measurement to avoid moisture condensation effects [56]. To reduce mapping time to 45 minutes per module, we acquire reflectance at just 3 critical wavelengths (at the 1730 nm ethylene vinyl acetate stretching mode, at the 1872 nm isosbestic point as a baseline metric, and at the 1902 nm water combination mode) at each point. Additional full spectra (151 distinct wavelengths) are acquired at 10 mm intervals in each direction. The background spectra extracted from each full measurement are interpolated and scaled to intersect the 1872 nm baseline reflectance at each 3-wavelength point. Using this approach, we find that water measurements taken with the 3-wavelength method match those of the original full 151-wavelength sampling ($R^2 > 0.95$).

3.2.5 Spatial Determination of Cell Parameters

We employ photoluminescence current-voltage (PLIV) imaging to spatially resolve the cell parameters of each mini-module using a two-diode cell model (series resistance, saturation currents, and illumination current, no shunt) at a resolution of ≤ 100 μm [57]. All samples

are measured in room conditions. The top glass of each cell is cleaned with isopropyl alcohol (IPA) immediately prior to measurement to avoid image artifacts from glass fouling. Images are acquired by an InGaAs camera (FLIR A6251sc). A four-quadrant power supply (Kepco BOP 20-20D-4866) is used to apply bias to and measure current from cells during PLIV. A 15 watt 808 nm laser (Jenoptik JOLD-30-FC18) and optical diffuser are used to illuminate cells with >95% homogeneity across the cell area. Samples are maintained at 25 °C during measurement by a thermoelectric cooler (TE Technology CP-040HT). The short-circuit current (J_{sc}), open-circuit voltage (V_{oc}), and maximum-power point voltage (V_{mpp}) from the JV measurement are used to determine PLIV measurement parameters. Images are acquired at all combinations of electrical bias (in 100 mV steps from V_{mpp} to V_{oc}) and incident photon flux (in steps of 0.2 suns from 0 to 1 sun equivalent illumination). 1-sun equivalent illumination is taken as the laser current at which the short-circuit current generated by the cell under the laser matches that from the JV measurement. An additional "background" image, taken with no illumination or applied bias, is subtracted from all other images. PLIV is carried out at room conditions.

3.2.6 Identification of Finger Interruptions

Forward-bias electroluminescence at V_{oc} (FBEL) images are acquired during the PLIV routine. Local Otsu thresholding is used to binarize FBEL images, yielding an "isolation mask" where 1 represents electrically isolated regions of the cell [58]. A similar treatment to a luminescence image at V_{oc} and 1-sun illumination yields a "finger mask" and "busbar mask". The union of the finger and isolation masks yields an "interruption mask" where 1 represents portions of fingers that are electrically interrupted from the busbar (interrupt mask). The "interruption mask" points with the shortest distance to the busbar are identified as finger interruptions. Results were manually pruned to remove false positives ($< 3\%$) from artifacts such as camera obstructions or glass fouling. We note that, along an already interrupted finger, subsequent interruptions further from the busbar will not provide additional contrast by FBEL and are therefore undetectable in our scheme.

3.2.7 Registration of WaRD and PLIV Data

Module orientation varies slightly from week to week and between PLIV and WaRD hardware. In each image, the same four module corners are manually located and used to align the image to a common orientation by rigid transformation. As maps of module moisture content and cell parameters are acquired at different spatial resolutions, a nearest-neighbor approach was used to relate the coarse WaRD maps to the PLIV data.

3.2.8 Raman Mapping of Contact Corrosion

The sister GB modules described in section 3.2.1 were exposed to 85 °C, 85% RH for up to 1000 hours, then peeled to expose the front side of their cells. Raman spectra were taken over the cell metallization near the center of the cell. Progress of corrosion reactions were monitored by Raman spectroscopy mapping on samples that had undergone different environmental exposures [59]. Raman spectra were taken from 0 to 1200 cm^{-1} by a Renishaw Confocal InVia Raman system (backscatter geometry, 100 mW 532 nm laser excitation source, 50x objective, 1.5 μm spot size). A 1250 μm × 250 μm region above the busbar of each sample was mapped with a step size of 50 μm. For each sample, these 125 spectra were normalized to the intensity of the silver acetate vibrational mode (145 cm^{-1}) and averaged [59].

3.3 Results

3.3.1 Moisture Saturates Rapidly at the Back Side of Glass-Backsheet Modules

WaRD maps on GB test modules (constructed without a cell to allow WaRD measurements to see water ingress through the backsheet) find that moisture content of the back side saturates in under 24 hours at 85 °C. WaRD maps on standard GG and GB mini-modules show that the front side reaches moisture saturation above the center of the cells after in about 500 hours at 85 °C. This rate of front side ingress is also representative of the back side in symmetric

GG modules. Together, these experiments demonstrate that the back side of the GB modules reaches saturation roughly 3 weeks earlier than the GG modules.

3.3.2 Finger Interruptions Form in Drier Regions of Glass-Backsheet Modules

Through weekly FBEL and WaRD imaging of each sample, we extract the location, timing, water concentration, and accumulated water dose at each interruption. (Figure 3.2a-b). Water dose accumulated by time t_n is defined by $D(x,y,t_n) = \sum_{i=0}^{n} c(x,y,t_i)$, where D, t, and c represent dose, time in environmental exposure, and water concentration for coordinates (x,y) on the cell area. We exclude "day zero" interrupts (present in the as-fabricated modules) from our analyses of interrupt location and timing.

We evaluate the effect of local water concentration and dose on the formation of finger

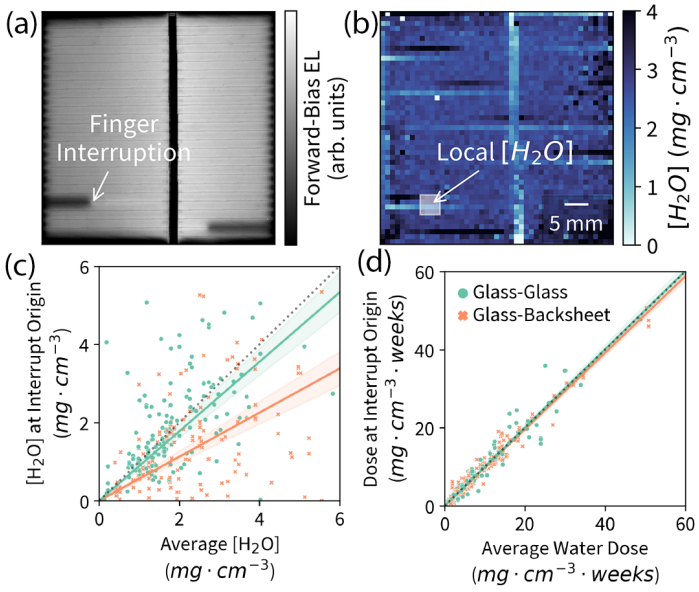

Figure 3.2. Colocating finger interruptions and water content: Example pair of (a) electroluminescence and (b) water content maps for a glass-backsheet module exposed to 85 °C, 85% RH for 670 hours. (c) Water concentration and (d) dose are compared between the interrupt location and the rest of the cell area across all environmental conditions. The dotted lines indicate equivalent water content/dose, the solid lines indicate linear fits, and the shaded bands indicate 95% confidence intervals.

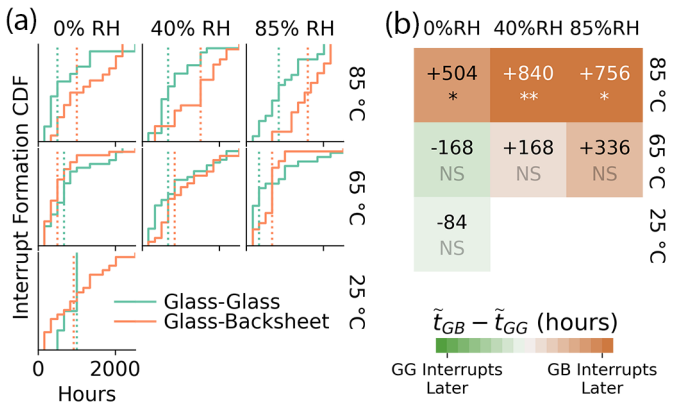

Figure 3.3. Time of Interrupt Formation in Silicon Modules under Environmental Stress: (a) Cumulative distribution of interrupt formations for glass-glass and glass-backsheet modules at each environmental condition. Dashed lines indicate median times to interruption. (b) The difference in median time ($\tilde{t}$) to interrupt formation between the two architectures at each environmental condition. Asterisks represent statistical significance in comparison across the two architectures at each condition ($** = p < 0.01, * = p < 0.05, NS = p >= 0.05$).

interruptions by comparing the water content in the immediate vicinity (within 2 mm) of the interrupt origin to the average water content across the module. The local and module-average contents are compared by linear regressions (Figure 3.2c-d) and Mann-Whitney U Tests [60]. GB modules formed interrupts in drier points within the module (p-value < 0.01, Fig. 3.2c). By contrast, interrupt origins in GG modules are not drier than the rest of the module ($p = 0.51$). Local dose did not differ from average dose within either module type ($p = 0.90$ for GG, $p = 0.70$ for GB). Additionally, the local dose around interrupts did not differ across module types ($p = 0.41$).

The accumulation of new interrupts over time in GG and GB modules is shown at each tested environmental condition in Figure 3.3a, where each curve describes the rate at which the total population of interrupts within each condition and BOM occur over 2500 hours of damp heat testing. These populations of interrupt timings are compared across module types in two ways: the median timings (shown by the dashed lines in Figure 3.3a), and Mann-Whitney U Tests to evaluate whether these differences are statistically significant. GG modules interrupt earlier than GB modules at our highest tested temperature of 85 °C, with statistical significance

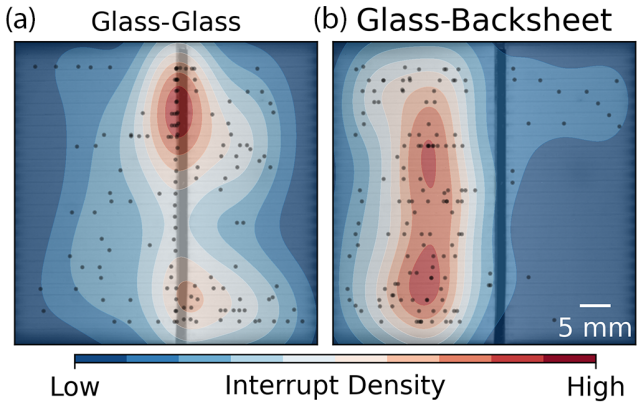

Figure 3.4. The spatial distribution of interrupts in (a) glass-glass and (b) glass-backsheet modules across all environmental conditions.

at all humidity levels (Figure 3.3b). Interestingly, increasing humidity seems to delay the onset of interrupts, as the median time to interruption is shorter in the driest samples. This is especially the case in GB modules, and the gap between GG and GB times to interruption grows with increasing humidity at each temperature.

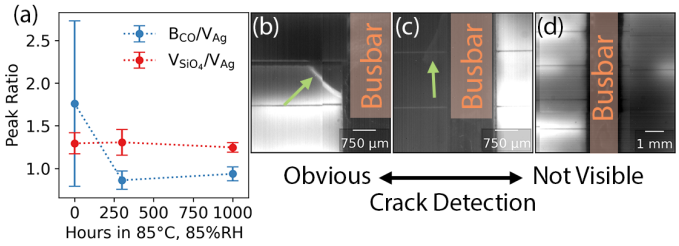

Figure 3.5. Traditional contact corrosion is not occuring within the modules: (a) Evolution of Raman vibrational modes indicative of silver contact corrosion at the busbar of GG modules over 1000 hours of exposure to 85 °C, 85% RH. (b-d) Representative high-resolution forward-bias electoluminescence images at finger interrupt origins. Green arrows indicate cracks when they are visible.

3.3.3 Glass-Glass Modules Form Interrupts at the Busbar

We find that finger interruptions in GG and GB modules form in different characteristic module regions (Figure 3.4) . GG modules form interrupts along the busbar, often near the module edge. GB modules, by contrast, tend to form interrupts mid-finger, away from the busbar but not at the very edge of the module. The spatial distribution of interruptions within each

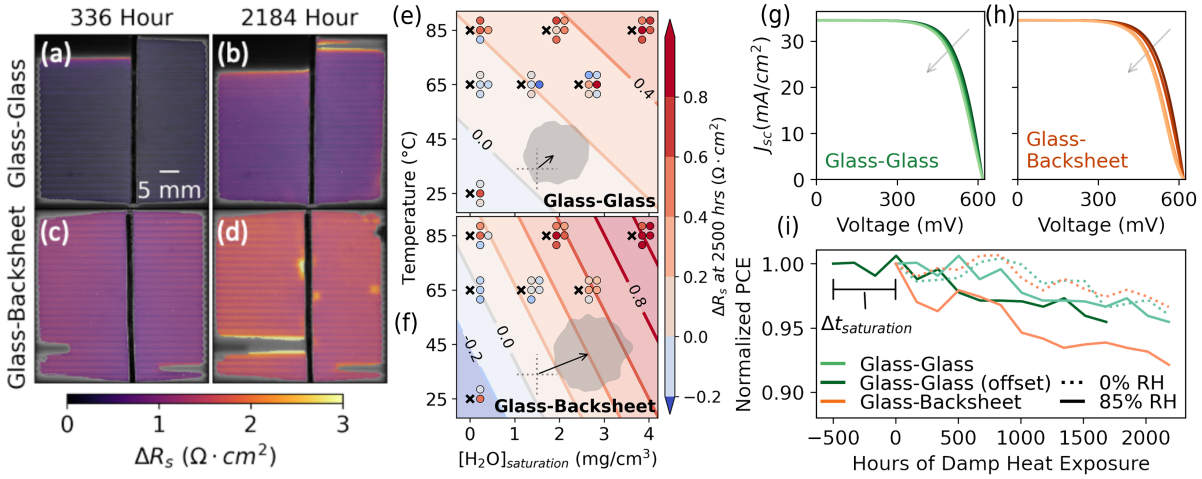

Figure 3.6. Background Series Resistance Increases under Environmental Stress: Change in series resistance for representative (a-b) glass-glass and (c-d) glass-backsheet modules after exposure to 85 °C, 85% RH. The grayscale background depicts forward-bias electroluminescence, while the foreground shows series resistance in the uninterrupted area. Increase in background resistance as a function of temperature and saturated module water content for (e) glass-glass and (f) glass-backsheet modules after 2500 hours of accelerated testing. The black crosses indicate test conditions, while the adjacent circles denote Rs changes in individual modules at each test condition. The color bar is shared between the contours and circles. The inset vector shows the gradient of Rs change with respect to temperature and saturated module water content, and the shading indicates 95% confidence bounds for the gradient vector. Simulated current-voltage curves for (g) glass-glass and (h) glass-backsheet modules affected only by background series resistance. (i) Isolated power loss from background resistance. The "offset" GG data is shifted such that its moisture saturation time matches that of GB modules.

module type does not vary across time or environmental condition.

3.3.4 No Evidence of Contact Corrosion

Raman spectra taken over the metallization near the center of cells extracted from GB mini-modules exposed to accelerated testing suggest that historical modes of contact corrosion are not occurring in these samples. Previous literature has established that in the event that the silver cell metallization is corroded by acetic acid generated from degradation of EVA encapsulant, the SiO_4 vibrational mode decreases in intensity while the C-O-Ag bending modes increases in intensity [61, 62, 59]. These changes are attributed to corrosion of the glass frit by acetic acid and the formation of silver acetate, respectively. We do not observe either of these

changes in our modules after 1000 hours at 85 °C, 85% RH (3.5a).

High resolution FBEL imaging in the vicinity of interrupt origins shows at least some of the interrupts to be caused by cracks in the cell. Absence of a visible crack here is not sufficient to say that a crack is not present, as they may be too small for our camera to observe (the highest resolution of our imaging hardware is about 30 μm) or positioned as to not affect the metallization (on which the contrast mechanism of FBEL relies).

3.3.5 Background Series Resistance Increases More in Glass-Backsheet Modules

Table 3.2. Background Series Resistance Response Surfaces

Glass-Glass	Coefficient	Std. Err.	*p*-value	95% CI
a (constant)	-0.253	0.273	0.362	(-0.811, 0.306)
b (temperature)	0.005	0.004	0.211	(-0.003, 0.014)
c ($[H_2O]$)	0.083	0.055	0.143	(-0.03, 0.196)
Glass-Backsheet	Coefficient	Std. Err.	*p*-value	95% CI
a (constant)	-0.371	0.282	0.2	(-0.95, 0.209)
b (temperature)	0.006	0.004	0.152	(-0.002, 0.015)
c ($[H_2O]$)	**0.147**	**0.051**	**0.008**	**(0.042, 0.252)**

Setting aside the regions of modules affected by finger interruptions, GB modules exhibit a larger increase in series resistance than GG modules at all but 0% RH conditions. We leverage the spatial characterization of cell parameters from PLIV and segmentation of finger interruptions from FBEL images to evaluate the uninterrupted "background" region of modules in isolation (Figure 3.6a-d).The grayscale background image in Figure 3.6a-d shows the raw FBEL image, and the purple-yellow foreground image shows the R_s map from PLIV plotted only in the "background" regions considered in subsequent analysis of background R_s. Degradation by background series resistance in particular differs between GG and GB samples, with GB samples suffering a greater increase in resistance at all but the driest conditions. To better quantify this

difference, for each module type we fit a first order response surface

$$d_{R_s} = a + bT + c[H_2O],$$

where d_{R_s} is the change in series resistance after 2500 hours of environmental exposure, T is the temperature (°C), and $[H_2O]$ is the saturation water content (mg/cm^3) in the module for a given environment. Individual module changes in background series resistance and the fitted response surfaces are shown in Figure 3.6e-f, and the numerical values and uncertainties of the response surfaces are given in Table 3.2. Though some outlying samples render our parameter confidence intervals quite wide, we see with statistical significance that higher water content leads to greater background series resistance increases in GB modules.

We isolate the impact of background R_s on module power generation by simulating their current density-voltage (JV) curves by the same shuntless two-diode cell model used in PLIV fitting [57]. Cell parameters are initialized by fitting JV curves measured for each cell prior to environmental exposure. The average background R_s increase from PLIV is then added to the starting R_s while all other parameters are held constant, yielding simulated JV curves affected only by this degradation mode. Representative simulated curves for GG and GB modules over 2500 hours at 85 °C, 85% RH are shown in Fig. 3.6g-h, along with the power conversion efficiency (PCE) extracted from such curves for all modules at 85 °C, 85% RH in Figure 3.6i. By shifting the GG PCE trendline 500 hours earlier, we align the GG and GB data such that both reach moisture saturation at the back contact at roughly t=0 hours. Still, the GB modules suffer about twice the PCE loss from background resistance as GG modules. In a dry environment at the same 85 °C temperature, the two module types show nearly identical increases in background resistance.

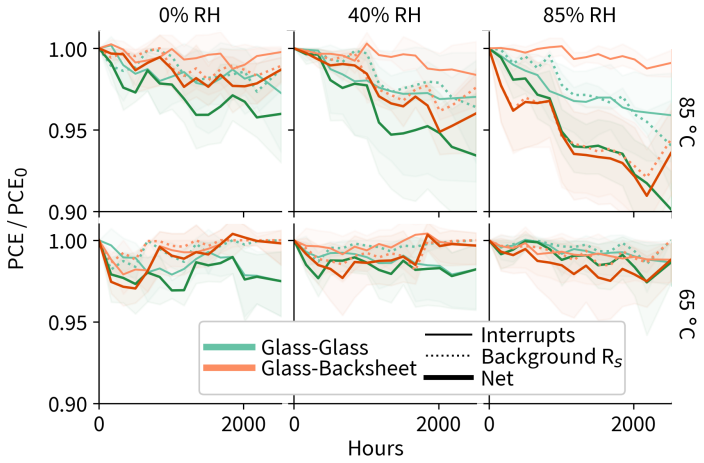

Figure 3.7. Dissected Power Losses of Silicon Modules under Environmental Stress: The isolated impacts of finger interrupts and background series resistance on power conversion efficiency are shown for each elevated environmental condition. The net loss in power conversion efficiency is also shown.

3.3.6 Net Effects of Finger Interruptions and Background Resistance

The individual and net impacts of background R_s and finger interruptions were extracted for each individual module, and are shown in Figure 3.7. Losses from background R_s are calculated by JV curve simulation as discussed in section 3.3.5. The impact of finger interruptions on PCE for each cell are estimated from the inactive area fraction seen via FBEL. The inactive area is scaled to an equivalent PCE loss by $PCE_{norm} = 1 - 0.467 * Area_{inactive}$. This relationship was empirically determined by a linear fit (RMSE=3% PCE_{norm}) to observed inactive area and normalized PCE (from JV curves) from our GG modules. We fit GG modules alone as we observed the majority of their power losses to arise from finger interruptions, and a fit to GB modules would include large background resistance effects.

3.4 Discussion

3.4.1 Mechanical Properties of Module Packaging May Explain Finger Interruptions

Our forensic analysis of finger interrupts suggests that their primary cause is cell cracking. For many of our interrupts, these cracks are clearly visible in FBEL. For the others, the alternative explanation of contact corrosion seems unlikely as we do not observe Raman signatures of byproducts from corrosion of the metallization (at least within the first 1000 hours of exposure to 85°C, 85% RH, by which point 70% of GG and 32% of GB finger interrupts had formed). We speculate that the difference in location of interrupts between GG and GB modules may arise from the mechanical properties of the module constructions. Previous studies found modules with stiffer encapsulants to generate larger stresses within the silicon cell [63, 64]. Additional reports find GG modules to generate larger stresses during lamination and thermal cycling than GB modules [65, 66]. Our observation of a high density of interrupts near the ends of the busbars in GG samples is consistent with reports of cracks formed during the interconnect soldering process [67, 43]. Lamination and tab soldering processes generate mechanical stresses in modules from coefficient of thermal expansion (CTE) mismatches between module components, and these stresses are most acute in the immediate vicinity of the interconnects [43, 68, 69, 70, 64]. The cause of mid-finger interrupts in GB samples is less clear, though we note that the combined thickness of the backsheet and back side ethylene-vinyl acetate layers in our modules thins from center to edge. Thicker polymer layers have been shown to reduce the fraction of total module mechanical stresses imparted across the cell [64].

We see that interrupts form earlier in drier conditions, and that interrupts in GB modules tend to form in drier parts of the module. Previous reports find the shear storage modulus of solar encapsulants to lessen with moisture exposure, attributed to plasticization of the polymers[37]. Stiffer (and, accordingly, drier) encapsulants impart more mechanical stresses on the cell, which would increase the chance of cracking [63, 71]. The magnitude of this plasticization effect varies

dramatically across encapsulants. For EVA, a 63% increase in relative humidity is required to match the reduction in shear modulus of a 1 °C temperature increase. Interestingly, the shear storage modulus of polyvinyl fluoride-based backsheet (as used in our modules) was found to be 16 times more sensitive to moisture than that of EVA (just a 4% RH increase is equivalent to a temperature increase of 1 °C). Assuming that the finger interruptions we observe are from mechanical cracks in the cell, the greater plasticization of backsheets may be a contributing factor to the delayed formation of finger interrupts we observe in GB modules at high humidities. Future studies aimed at colocation of module stresses and water content across environmental conditions and bills of material should be undertaken to investigate this moisture-driven mechanism of mechanical failure in modules.

3.4.2 A Mode of Series Resistance Increase Unique to Glass-Backsheet

Background series resistance increases in uninterrupted cell regions are nearly twice as severe in GB modules than GG at the most aggressive humidity condition. Possible explanations for this result include faster moisture ingress through the backsheet leading to earlier degradation by the same mode, or a unique degradation mode between the backsheet and the cell which is not present in the GG modules. The moisture content at the back side of GB modules reaches saturation a full 500 hours earlier than GG at 85 °C. Even when accounting for this offset (for example comparing GB week 3 to GG week 6) the series resistance of GB modules remains higher, suggesting that the difference in time to water saturation is not a sufficient explanation for this issue (Figure 3.6h). In fact, the series resistance of our GG modules does not show much sensitivity to humidity at all, displaying essentially the same power loss from background resistance in 0% RH and 85% RH conditions at 85 °C (Figure 3.6h). In all scenarios, the front side of GB and GG modules should have identical moisture exposure. Together these observations implicate moisture as a reactant in some form of back-contact degradation mode unique to GB modules with Al-BSF cells. Future work is needed to check for a similar degradation mode in passivated emitter rear contact (PERC) cells in GB modules.

3.4.3 Tailoring Module Packaging to Deployed Environment

The durability of the GG modules in this study is limited by finger interruptions, and the durability of GB modules by background R_s issues at high humidities. The results would suggest that GB modules would be preferred in drier climates, while GG modules would be best suited for humid climates. This stands in contrast to the conventional wisdom that a ”breathable” backsheet is preferred in humid environments to allow moisture and acetic acid generated from EVA hydrolysis to escape the module [38, 19]. Modern cells with newer solder paste formulations may be less susceptible to contact corrosion via acetic acid, as demonstrated by the invariance of the R_s of the GG modules in this study to humidity and the absence of corrosion byproducts in Raman measurements. This is encouraging, as the market share of GG modules is projected to increase due to growing interest from grid installers in bifacial modules [72]. Further efforts to reduce cracking in GG modules are needed. Given that the majority of GG cracks originate at the busbar, technologies that aim to either reduce thermal stresses at the busbar during soldering [73] or to implement interconnect that avoid busbars altogether could be of interest.

3.5 Conclusion

We have shown that moisture can be accessed as a dimension in correlative studies of module durability. Two primary modes of cell degradation were tracked during durability testing using correlative imaging - finger interruptions and ”background” series resistance. Finger interruptions occurred earlier in glass-glass modules than in glass-backsheet, and at drier conditions regardless of module architecture. Interrupts in glass-backsheet modules formed in drier parts of the module.

Background series resistance shows a strong sensitivity to humidity in glass-backsheet modules, in which raising relative humidity at 85 °C from 0 to 85% RH doubled the efficiency loss attributed specifically to this degradation mode (from 4 to 8% relative after 2500 hours). In contrast, we find that modern glass-glass modules are resilient to humidity-driven increases in

series resistance. The performance of glass-glass modules is primarily limited by mechanical failures in the cell. To improve the operating lifespan of fielded modules, it will be important to understand the influence mechanical stress has on module durability.

Future WaRD-informed studies on fielded modules or in a fluctuating test environment designed to generate moisture gradients within the module may reveal further local influences of water on silicon module durability.

3.6 Acknowledgements

Chapter 3, in part, is a reprint of the material "Glass vs. Backsheet: Deconvoluting the Role of Moisture in Power Loss in Silicon Photovoltaics With Correlated Imaging During Accelerated Testing" as it appears in IEEE Journal of Photovoltaics, Kumar, R. E., Von Gastrow, G., Theut, N., Jeffries, A. M., Sidawi, T., Ha, A., DePlachett, F., Moctezuma-Andraca, H., Donaldson, S., Bertoni, M. I., and Fenning, D. P. 1-8 (2021). The dissertation author was the primary investigator and author of this material.

Part II

Aligning Sequential, Multimodal, Spatial Measurements of Anisotropic Samples

Drawing correlations such as structure-property relationships is integral to the study of materials. To this end, studies that combine spatially-resolved characterization by multiple modalities can offer strong explanatory power, correlating physical or functional properties at the local level. In particular, the growth in capabilities of and access to synchrotron facilities around the world has enabled novel multi-modal studies on materials ranging from biological samples[74, 75, 76] to next-generation photovoltaic materials.[77, 78, 79, 80, 81, 82, 83] Extracting scientific insights from these correlative datasets requires careful consideration of the mode-specific, and often non-overlapping, sampling volume used in the correlative microscopy. Here we describe a ray-tracing method that accounts for the finite extent and roughness of thin films and nanomaterials, creating a first approximation of the probe-sample interaction for each modality that tightens correlations in multi-modal nanoprobe characterization.

The correlations in multimodal microscopy data, e.g. generated by synchrotrons, can be systematically reduced by geometric factors and local probe-sample interactions. For example, matrix effects can alter X-ray fluorescence (XRF) measurements, where the path length of both incident and fluoresced photons within the sample can selectively attenuate a given element's signal recorded at the detector. [84, 85, 81] Geometric factors can be significant in the study of samples anisotropic in either morphology or composition, such as porous battery electrodes[86, 87], catalysts [88, 89], standalone single-crystals [78], biological cells [90], or patterned semiconductor devices [91]. Furthermore, these factors compound when relating multiple measurements of a sample. Whether acquired in a synchronous correlative microscopy approach or via sequential measurements, each mode of data is subject to unique geometric effects determined by instrument geometry and sample properties.

Here, we encounter the problem of correlating sequential measurements in studying the interplay of structure, composition, and optoelectronic behavior of europium-doped $CsPbBr_3$ halide perovskite. Halide perovskites are an emergent class of materials potentially suitable for most optoelectronic applications. Their intrinsic properties are commensurate with optoelectronic figures of merit, as they exhibit large absorption coefficients with sharp onsets, high

photoluminescent yields, tunable bandgaps, long carrier lifetimes, and low intrinsic trap densities. [92, 93, 94, 95, 96] This, in conjunction with their facile, solution-based fabrication methods and wide-ranging flexibility in chemical composition, has made perovskites attractive candidates in the development of light-emitting diodes, lasers, phosphors, detectors, and indoor and outdoor photovoltaic cells. [97, 98, 99, 100, 101, 102, 103, 104, 105, 106, 107, 108, 109, 110, 111, 112]

Halide perovskite materials possess the ABX3 structure, where the chemical species on each of the A-, B-, and X- sites can be varied and mixed (within the bounds of structural formability guided by the Goldschmidt tolerance factor and related heuristics) to modulate the material's properties.[113, 114, 115] The composition of each site has been under investigation, but typically consists of either an organic (methylammonium or formamidinium) or inorganic (Cs) A-site, a divalent B-site (most often Pb), and a halide at the X-site (Br, Cl, I). Inorganic halide perovskites, most commonly of composition CsPbX3, have been of particular interest for their stability against environmental stresses. [110, 116, 109, 117] Variation of the X-site from chlorine to bromine to iodine adjusts the bandgap across the visible spectrum while preserving high photoluminescence quantum yields and narrow emission line widths.[118] The addition of lanthanide ions to CsPbX3 perovskites improves the photoluminescent yields even further, extends the possible emission range into the near-infrared, and in some cases enables new physics within the material as a divalent 2+/3+ or aliovalent 3+ dopant at the B-site. [119, 120, 121, 122]

Of the lanthanide additives, europium has shown especially promising improvements to performance of both organic and inorganic perovskites. Europium-containing inorganic perovskite quantum dots display blue, green, and red emission with photoluminescent yields up to 90%, the red emission arising from quantum cutting between the host lattice and Eu^{3+}.[123, 117] Strong excitonic binding in these quantum dots makes their PL yield less sensitive to particle size and morphology, allowing bright particles to be formed even within glass melts. [99] Solar cells fabricated with europium additives to the hybrid MAPbI3 and inorganic $CsPbI_3$ and $CsPbI_2Br$ perovskite absorbers displayed increased power conversion efficiency and stability under conditions ranging from exposure to ambient atmosphere to prolonged one-sun

illumination.[121, 116, 124, 125] The improvement in stability has been ascribed to strain-induced stabilization of the kinetically-trapped photoactive perovskite phase and the suppression of ionic defects via "redox shuttling" between Eu^{2+} and Eu^{2+} ions. Existing literature has established both the benefits of europium to perovskites, as well as proposed the mechanisms by which some of these benefits are conferred. Incorporation of Eu onto the lattice in place of lead, its mitigation of deleterious redox reactions, and its influence on microstrain have been attributed to improving the optoelectronic and stability properties of perovskite devices.[121, 116] In the following chapters, we leverage high-resolution mapping techniques to evaluate these hypothesized mechanisms at the nanoscale. Once the various datasets capturing spatial microstrain, composition, and photoluminescence are in hand, I develop a ray-tracing workflow to enable a faithful correlation across datasets. Each of the raw datasets are subject to unique sample-probe interactions and measurement geometries, making a simple pixel-to-pixel correlation innacurate as the sampling volume at each pixel differs across datasets. The ray-tracing approach quantifies these sampling volumes, with which we mutually convolve the datasets to compare equivalent sampling volumes. This treatment improves the accuracy of fluorescence data and clarifies relationships between microstrain, composition, and optoelectronics in Eu:$CsPbBr_3$.

Chapter 4

Europium Addition Reduces Local Structural Disorder and Enhances Photoluminescent Yield in Perovskite $CsPbBr_3$

4.1 Introduction

In this study, we use synchrotron nanoprobe X-Ray Diffraction (nXRD) and Fluorescence (nXRF) mapping to investigate the nanoscale stoichiometry and microstructure of $CsPbBr_3$ crystal films with nominal 5% Eu^{2+} addition. Using micro-photoluminescence, we correlate the photoluminescence (PL) to local elemental composition and strain distribution. We find that Eu addition clearly improves PL yield and line width with a minor blue-shift to the bandgap. This improved PL is ascribed to a reduction in microstrain seen by nXRD, which along with heterogeneity in europium content seen by nXRF indicates that the presence of europium changes the crystallization process. Finally, the stability of $CsPbBr_3$ under sustained hard x-ray dosage is greatly improved with the addition of europium. Our work sheds light on the local influence of europium on the structural and optoelectronic properties of perovskites, further supporting this class of materials as an encouraging prospect for use in applications ranging from light emission to high-energy photon detection.

4.2 Experimental Methods

4.2.1 Sample Synthesis

Substrates were cleaned via a series of sonication and rinse steps as follows: sonication in 2 vol% Hellmanex in DI water for 15 min, rinse with DI water, sonication in DI water for 15 minutes, rinse with DI water, sonication in IPA for 15 min, sonication in acetone for 15 min, rinse with IPA, then dried. 0.33 M precursor solution (molar ratios of 1:1 $CsBr:PbBr_2$ for $CsPbBr_3$, and 1:0.95:0.05 $CsBr:PbBr_2:EuBr_2$ for $Eu:CsPbBr_3$ samples) was made in DMSO inside a nitrogen glovebox. The solution was heated to 120°C and mixed by vortexing until all solids dissolved. The clean substrates were plasma-treated for 10 mins, in air at 200 mbar. The PDMS stamps were preheated on a hotplate at 150°C. 40uL of precursor solution was dropped on the substrate. The substrate was spun for 10 seconds at 500 rpm (accelerated at 500 rpm/s), then put upside down on the PDMS and pressed with tweezer for 5 minutes. Then the substrate was removed from the PDMS, flipped over and heated for another 2 minutes at 150°C.

4.2.2 Inductively-Coupled Plasma Mass Spectrometry

The relative molar ratios of Eu, Pb and Cs were measured using a Thermo Scientific iCAP RQ ICP-MS. The as-grown crystals were scraped off the substrates and dissolved in 2% analytical grade nitric acid in preparation for the measurement.

4.2.3 Benchtop X-Ray Diffraction

The XRD of the samples was acquired on a Rigaku Smartlab with 0.02 degrees per step from 10° to 50° with 2mm slit in parallel beam mode. Samples were measured on directly on the substrate they were synthesized on.

4.2.4 Synchrotron X-Ray Fluorescence and X-Ray Diffraction

Nano-XRF and nano-XRD were both acquired at the 26-ID-C beamline at the Center for Nanoscale Materials and the Advanced Photon Source at Argonne National Laboratory,

using a focused 10 keV x-ray beam. d-spacing was determined precisely by performing a spatially-resolved rocking curve, where the incident and detector angles were held constant while the sample theta was rotated. The 2D scattering detector was calibrated by measurement of a powder silicon reference sample. This procedure enables complete reconstruction of the 3D scattering vector at each point, which allows us to know not only the magnitude of the scattering (d-spacing), but the direction of scattering (relative lattice tilt). Additionally, the peak width of overall scattering intensity vs sample theta is fit to provide a measure of local structural disorder. XRF readings were corrected for attenuation of both the incident and fluoresced x-rays, using the nominal stoichiometry (5% Eu:$CsPbBr_3$ or pristine $CsPbBr_3$) and a density of 4.42 g/cm3 to approximate the X-ray attenuation coefficient of the sample. In addition to the attenuation coefficient, the optical path length of both the incident and fluoresced photons was approximated using a ray-tracing approach, where the incident beam and detector orientations are known from the measurement geometry, and the 3-d sample morphology is approximated using the white-light interferometry thickness map under the assumption that no voids exist within the sample. This treatment, along with a detector calibration using NIST XRF standards (NBS1832, NBS1833) normalizes the measured fluorescence to remove hardware and sample attenuation effects and enable quantitative analysis.

4.2.5 Thickness Measurement

The topography of the crystals was measured with a Filmetrics Profilm3D in White Light Interferometry mode with 50x magnification, at a nominal lateral resolution of 0.1 μm and a vertical resolution of 0.1 nm.

4.2.6 X-Ray Photoelectron Spectroscopy (XPS)

XPS spectra were acquired using a Kratos Analytical AXIS Supra equipped with a monochromatic Al K-alpha x-ray source at the UC Irvine Materials Research Institute. Measurements were taken at 0° and 70° angles of incidence, acquired with a 20 eV pass energy at 0.1 eV

steps with 100 ms dwell time. Spectra were background corrected using a Shirley background, aligned in energy using adventitious carbon, corrected by the instrument and element specific sensitivity factors (2.467 for Eu 3d, 8.329 for Pb 4f), and peaks were fit by Voigt line shapes to find peak areas.

4.2.7 Micro-Photoluminescence

Photoluminescence maps were taken using a Renishaw Raman/microPL tool with a 514nm excitation laser, 600 mm grating, 0.5s dwell time and 0.05% power. The photoluminescence peak position, intensity, and FWHM were extracted by a single-Gaussian fitting of the raw data.

4.3 Results and Discussion

We fabricated $CsPbBr_3$ crystals with and without 5% $EuBr_2$ (mol fraction with respect to the B-site) added to the precursor solution on quartz substrates, using a previously-established PDMS stamping method during annealing.[126] This fabrication approach results in isolated thin-film crystals typically 1 -2 μm thick and 20-30 μm wide. Inductively-Coupled Plasma Mass Spectrometry (ICP-MS) found the average Eu mol fraction in the Eu:$CsPbBr_3$ samples to be 4.8%, near the nominal 5% (Table S1). Benchtop XRD confirms that both crystals with 5% mol $EuBr_2$ added (Eu:$CsPbBr_3$) and pristine $CsPbBr_3$ crystals form in the room-temperature orthorhombic phase (Pnma, ICSD #97851) (Figure 4.1a). The Eu:$CsPbBr_3$ crystals show less texture than the $CsPbBr_3$, as the benchtop diffraction pattern clearly shows the Eu:$CsPbBr_3$ microcrystals exhibit a wider range of orientations. We do not observe a shift in the diffraction peaks upon addition of 5 mol% Eu^{2+}. This is not unexpected, as the ionic radii for octahedrally-coordinated Eu^{2+} and Pb2+ cations are similar at 117 and 119 pm, respectively.[127]Previous reports have shown europium to have varying effects on the lattice parameter of perovskites, though there is consensus that europium can be incorporated into the perovskite crystal structure at moderate loadings with little to no effect on the lattice parameter.[111, 121, 116] For example,

Wang et al. showed that, in methylammonium lead iodide, increasing europium loading does not affect the diffraction peak positions until 4.8 mol%, at which point they observe a peak shift indicating an increased lattice parameter.

4.3.1 Nano-Diffraction Shows Reduced Structural Disorder

To better understand the crystals' microstructure, synchrotron-based scanning nano-X-Ray Diffraction (nXRD) measurements were carried out on select individual crystals from each sample type. This technique rasters a 60-nm full-width half-maximum (FWHM) monochromatic X-ray probe across the sample and uses a 2D panel detector to collect the scattering produced at each point, generating a rich, nanoscale map of the structural properties.[79] nXRD is highly sensitive both in terms of detection limit and spatial resolving power. Minority crystal orientations and phases barely present or undetectable in benchtop XRD data can often be seen clearly in nXRD, although the total area sampled is limited currently to several 100s μm^2. Coupled with supporting characterization, from nXRD we obtain unique insights into the microstructural behavior of europium in $CsPbBr_3$.

The nXRD reveals that, unlike the $CsPbBr_3$, the individual Eu:$CsPbBr_3$ "crystals" are, in fact, multicrystalline, with crystallites diffracting from multiple orientations present across the crystal area. Figure 4.1(b) shows a nanoscale map of microstrain in two exemplary crystals of each type, showing the variation in d¬-spacing relative to the average value within the crystallite. Only a fraction of the geometric area of the Eu:$CsPbBr_3$ crystals diffract to a particular Bragg angle. The Eu:$CsPbBr_3$ remain fully crystalline, but other orientations account for the diffraction from areas of the crystal in white in Fig 1 (b). In the case of the pristine samples, one orientation is dominant and expressed across the entire crystal area (Figure 4.1b). This suggests that the addition of europium to $CsPbBr_3$ precursors alters the crystallization process and promotes the formation of smaller crystalline domains. As can be seen from the scanning nano-diffraction, the strain state varies substantially within individual domains, with much higher levels of microstrain in the pristine $CsPbBr_3$. The intensity of color in Figure 4.1b indicates the local deviation in

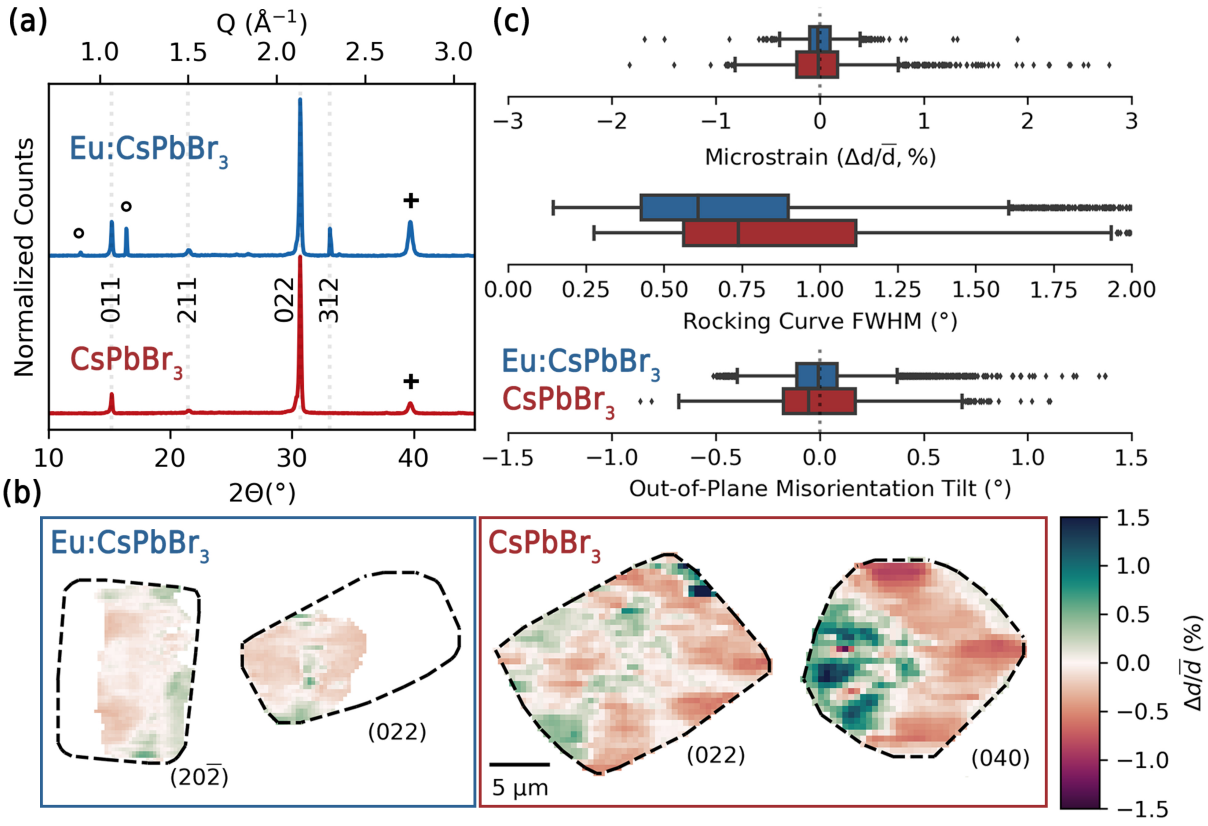

Figure 4.1. *Europium Reduces Microstrain in CsPbBr$_3$*: (a) Benchtop XRD patterns of $CsPbBr_3$ and Eu:$CsPbBr_3$ samples. Peaks are indexed to the orthorhombic phase, with peaks arising from $EuBr_2$ precursor ('o') and Pt from the fiducial marks present on the substrate ('+') indicated. (b) Spatial distribution of relative d-spacing in two crystals of each sample type obtained by synchrotron nano-XRD. (c) Overall distributions of strain, diffraction peak width, and out-of-plane lattice tilt in the $CsPbBr_3$ and Eu:$CsPbBr_3$ samples, including all measured data (additional data shown in the SI).

d-spacing relative to the average d-spacing observed across the crystal area. These deviations contribute on aggregate to the microstrain seen in a benchtop measurement. The Eu:$CsPbBr_3$ sample exhibits less microstrain than the $CsPbBr_3$ sample. Furthermore, the gradient of d-spacing (how fast the color changes in Figure 4.1b) across the Eu:$CsPbBr_3$ crystals is lower in magnitude than in $CsPbBr_3$, meaning that the strain state is more homogenous across these samples with smaller absolute values. This finding is summarized in the boxplots at the top of Figure 4.1c, where the distribution of d-spacing variation is narrower for Eu:$CsPbBr_3$. Note that while we can confidently observe microstrain, we have not reported the absolute strain value. For the

polycrystals, reporting an absolute strain by just one orientation may give an incomplete picture. However, we see a clear reduction in the overall microstrain of crystals containing europium. The Eu:$CsPbBr_3$ crystals also display a lower degree of mosaicity, i.e., less tilting of the lattice across each crystalline domain, and reduced rocking curve full-width half-maximum (Figure 4.1c). The reduced rocking curve FWHM indicates reduced structural disorder within the nanoscopic X-ray probe interaction volume. Peak broadening can signal multiple structural phenomenon, such as lattice defects (dislocations, interstitials, etc.), mosaicity, varying strain state, or small diffracting domains.[128] We do not expect much domain-size broadening here as the planar area of our diffracting domains are tens of microns across, and the thicknesses associated with domain-size broadening (¡100 nm) would imply unlikely domains with extremely high aspect ratios. This leaves us to conclude that the broadening we observe consists of lattice defects and the already identified mosaicity and strain variation in our sample. On the whole, the nXRD paints an interesting picture of europium's impact on the $CsPbBr_3$ microstructure: we find evident polycrystallinity and decrease in texture, indicating a reduction in crystallographic order at long length scales (microns), but also improvement of short- to medium-range structural order, including reduced structural defect density and mosaicity. Only small amounts of second phases, which we attribute to unreacted precursors, can be seen via nXRD and are primarily located around the perimeter of the crystals. We identify these as $EuBr_2$ and PbBr2, though the proximity of reflections from these phases in reciprocal space makes assignment in nXRD difficult. In the Eu:$CsPbBr_3$ samples, the benchtop XRD (taken before the nXRD) clearly shows $EuBr_2$, implying that this $EuBr_2$ is unreacted precursor rather than a degradation product. In the case of the europium-free $CsPbBr_3$ samples we can confidently assign the precursor diffraction to PbBr2.

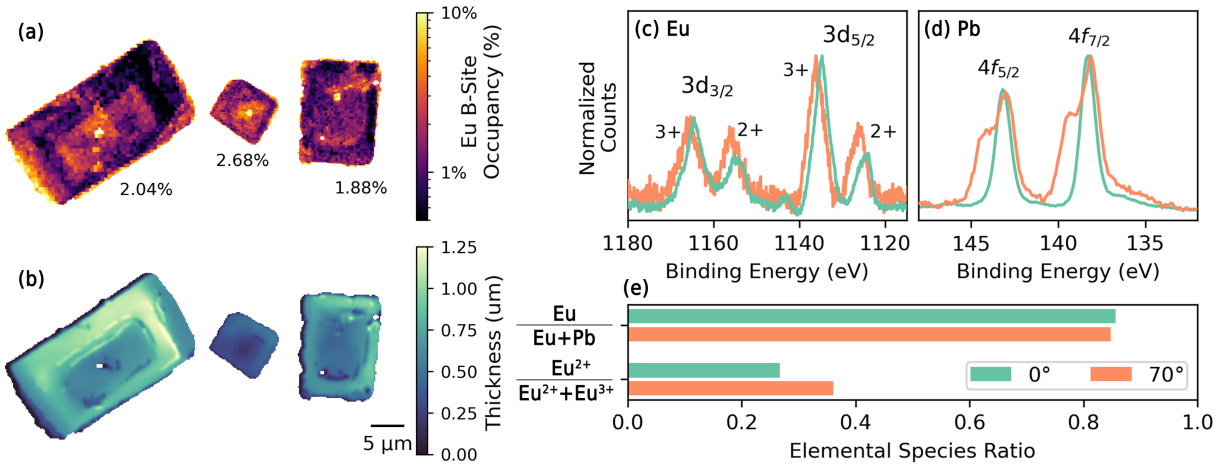

Figure 4.2. *Europium is Heterogeneously Incorporated into $CsPbBr_3$*: (a) Implied europium B-site occupancy as measured by synchrotron nano-XRF microscopy. The average is indicated below each crystal. (b) Thickness images corresponding to the crystals above. Scale bar is shared between (a) and (b). (c) Eu 3d and (d) Pb 4f XPS spectra, taken at normal (green) and grazing angles of incidence (orange). (e) The ratios between Eu oxidation states, and between Eu and Pb content, from the above XPS spectra.

4.3.2 Composition and Surface Chemistry of Eu:$CsPbBr_3$ Crystals

Europium is Heterogeneously Incorporated

Nano-X-Ray Fluorescence (nXRF) microscopy reveals that the local B-site stoichiometry varies spatially across all Eu:$CsPbBr_3$ samples, from trace amounts up to local concentrations of 10% Eu (Figure 4.2a). With detection of only minor amounts of $EuBr_2$ in these samples and no clear evidence of other impurity phases from benchtop or nXRD, we evaluate B-site stoichiometry in terms of the implied Eu B-site occupancy $M_Eu/(M_Eu+M_Pb)$, where M is the areal molar concentration (mol/cm^2) of the chemical species, and all europium and lead ions are assumed to be incorporated into the perovskite lattice. Note that these values are in areal concentration – nXRF provides compositional quantification integrated along the beam path, in this case integrating through the vertical dimension of the film. Eu-occupancy peaks as high as 10% at the crystal center, then decays to trace levels towards the crystal edges (Figure 4.2a). The average content is about 2-2.5%, somewhat lower than the ICP-MS value of 4.8%. Unlike nXRF, ICP-MS averages over the total contents of the substrate, implying that either our nXRF

sample size is too small to capture the true average Eu-occupancy, or that residual Eu species are present on the substrate outside of the perovskite after fabrication. The latter seems to be true in our case given that we observe unreacted $EuBr_2$ around the crystals by both benchtop XRD and nXRD. This 2.5% measured Eu occupancy is consistent with our lack of any observed diffraction peak shifts, as seen at similar concentrations in Eu:MAPbI3. [31] The Eu:$CsPbBr_3$ crystals are thinner in the center, as measured by white-light interferometry (Figure 4.2b), with larger concentrations of europium being present in these thinner regions. The $CsPbBr_3$ crystals do not have this thin-center morphology and are generally thicker than their europium-containing counterparts.

The Crystal Surfaces are Rich in Europium

To better understand the chemistry and distribution of Eu in the crystals, we conducted angle-dependent XPS measurements. The spectra were collected at 0° and 70° angles of incidence to probe depth-dependent variations in chemical composition and oxidation state within the first few nanometers of the crystal surface. The Eu 3d and Pb 4f spectra are shown in Figure 4.2c-d. Focusing on the Eu 3d spectra, we see doublets corresponding to both Eu^{2+} and Eu^{2+}.[129] Notably, we introduce only Eu(II), whereas most previous reports introduce the more common Eu(III). The chemistry in the thin film crystals is in the end similar to previous reports, where we find a coexistence of Eu^{2+}/Eu^{2+} oxidation states within the sample.[111, 121] The population of Eu^{2+} may be slightly higher at the surface (Figure 4.2e) based upon the increase seen when moving from normal to grazing incidence. We note that these peak ratios qualitatively rather than quantitatively reflect the relative population of the species, given the unknown depth distribution and the heterogeneity evident in the sample. The Pb 4f spectra in Figure 4.2d reveal the appearance of a high-binding energy peak in the surface-sensitive 70° spectrum, consistent with the native oxide of lead.[130] Figure 4.2e also shows that the implied Eu B-site fraction at the surface is Eu-rich, reaching 80%, as derived from the XPS after accounting for the spectral relative sensitivity factors (RSF). This evident surface enrichment, in conjunction with the nXRD

identification of unreacted $EuBr_2$ precursor primarily around the edge of the crystal, suggests that at least a portion of the europium added during synthesis segregates to the outer crystal surfaces. Even so, the numbers point to a significant degree of europium incorporation within the bulk crystal. If the first 5 nanometers of the micron-thick crystals have 80% Eu-occupancy as measured by XPS, the bulk crystal would still need to have an average 1.6% Eu-occupancy to yield the thickness-integrated 2% value detected by nXRF. This presents just a 25% error in the bulk europium loading determined by nXRF and maintains the observation that the bulk of the Eu:$CsPbBr_3$ crystals are rich in europium while maintaining the perovskite phase.

4.3.3 Photoluminescence Intensity Increases with Europium Addition

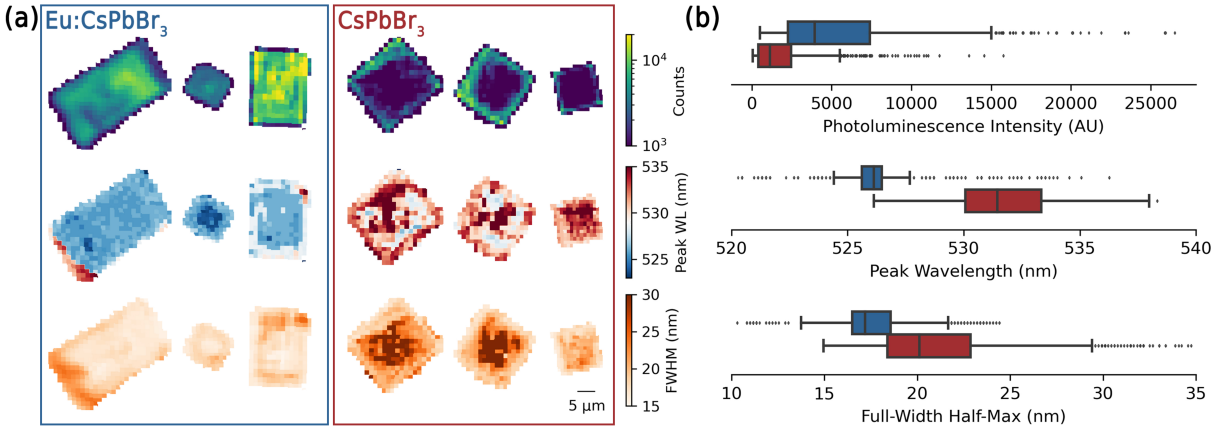

Figure 4.3. *Europium Blueshifts and Brightens Photoluminescence in $CsPbBr_3$*: Photoluminescence behavior. a) Maps of photoluminescence intensity, peak emission wavelength, and emission full-width half-max for representative Eu:$CsPbBr_3$ crystals (left) and $CsPbBr_3$ (right). b) Overall distributions of the fitted photoluminescence parameters from (a).

Eu:$CsPbBr_3$ crystals display superior photoluminescence properties with respect to their pristine counterparts. Figure 4.3a shows micro-photoluminescence maps of the intensity (top row), peak wavelength of emission (middle row), and FWHM (bottom row) for the Eu:$CsPbBr_3$ (left) and $CsPbBr_3$ crystals (right). The Eu:$CsPbBr_3$ crystals show brighter photoluminescence (PL) on average, with roughly 2x higher intensity as seen in the summary box plot of Figure 4.33b. The Eu:$CsPbBr_3$ crystals show strong luminescence from much of the crystal area, while the

$CsPbBr_3$ crystals show strong edge-to-center variation with the edges being substantially brighter than the central regions of the crystal. The emission spectra of Eu:$CsPbBr_3$ are blue-shifted by about 5 nm on average and have lower FWHM relative to $CsPbBr_3$. These changes suggest that Eu incorporation improves the optoelectronic quality of in the perovskite by reducing shallow trap states that would serve to broaden the emission spectrum and reduce band-to-band recombination. Where the Eu:$CsPbBr_3$ crystals show relatively uniform emission spectrum across the area of the crystal, the $CsPbBr_3$ crystals show a chaotic distribution of red- and blue-shifted regions. This varying distribution of emission point-to-point (4.6 nm standard deviation) echoes the substantial variations in strain seen in the pristine crystals (Figure 4.1b). This is consistent with our previously reported finding that local strain leads directly to luminescence peaks shifts in $CsPbBr_3$.[130] Both crystal chemistries display an edge-to-center variation in emission wavelength, though the direction of these trends are reversed – the edges are redshifted in Eu:$CsPbBr_3$, but blue-shifted in $CsPbBr_3$. The redshift towards the edges in europium containing samples is further evidence that europium incorporation lowers the emission wavelength, given that nXRF shows Eu-occupancy to decrease from center to edge.

4.3.4 Stability Under X-Rays

The incorporation of Eu dramatically improves the radiation hardness of the crystal, a key criterion for application in high-energy particle detection or in extreme environments. The structural stability of Eu:$CsPbBr_3$ and $CsPbBr_3$ crystals was examined under continuous 10 keV hard x-ray exposure at 1.9 x 1021 photons/cm2 /s. Waterfall plots of the time-resolved diffraction during X-ray exposure are shown in Figure 4.4a for Eu:$CsPbBr_3$ (top) and $CsPbBr_3$ (bottom). The $CsPbBr_3$ shows significant structural degradation. The strongest diffraction peak at 3.3Å-1 in the $CsPbBr_3$ sample shifts to higher diffraction angles during the beam exposure, a “lattice collapse” mode of structural integrity loss we commonly observe when exposing sensitive perovskites to high doses of focused hard x-rays.[130] Loss of crystallographic structure can manifest in peak shifts, as severed atomic bonds cause d-spacings to change, and in peak intensity loss, as portions

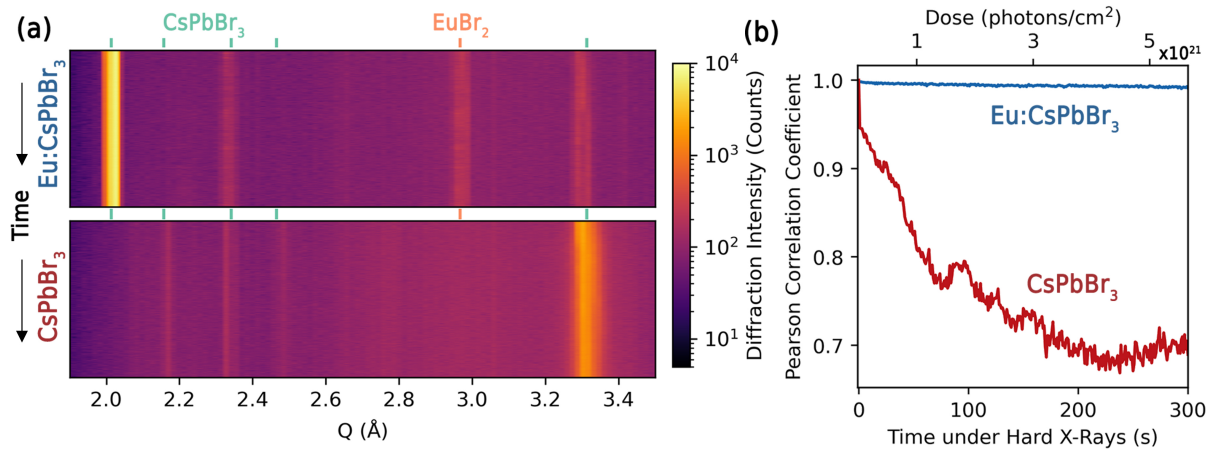

Figure 4.4. *Europium Improves X-Ray Hardness of $CsPbBr_3$*: (a) Waterfall plots of diffraction patterns of Eu:$CsPbBr_3$ and $CsPbBr_3$ crystals exposed to sustained focused hard x-rays for 5 minutes. Diffracting phases are indexed by tick marks above the plots. (b) Statistical correlation over time between the images of the diffraction patterns collected by the area detector, corresponding to the waterfall plots in (a).

of the diffracting domain become disordered. Pearson correlation of the time-resolved area diffraction images to the initial image takes both of these degradation signatures into account and shows that europium imparts much greater structural stability and radiation hardness to the crystal (Figure 4.4b). Some minor instability remains even in the Eu:$CsPbBr_3$ – we note that a peak splitting of the 3.3Å-1 peak persists after 100s exposure (Figure 4.4a). Despite its multicrystallinity, the reduced microscopic structural disorder in Eu:$CsPbBr_3$ dominates overall to improve x-ray hardness.

4.3.5 Discussion

Our results make clear that europium addition has a pronounced effect on the nucleation and growth of $CsPbBr_3$ crystals. Based on the heightened europium content at the crystal centers it seems as though europium clustering may act as a seed for nucleation and encourage polycrystallinity. Additionally, XPS shows that europium is enriched at the surface. It is possible that europium-rich surface layers are acting as a passivation layer for the perovskite crystals. In looking towards device applications requiring charge extraction, such as photo-

voltaics or optical sensors, the increased polycrystallinity concomitant with europium addition may reduce device performance by hindering long range charge transport. If columnar grain structures can be maintained, such devices may still produce enhanced performance. Various literature reports, including successful solar cell fabrication with Eu:$CsPbBr_3$, suggest that the growth kinetics of europium in perovskites can be overcome to yield performant optoelectronic devices.[111, 121, 124] As in our findings, europium-containing perovskite solar cells are consistently reported to have reduced grain sizes and improved stability against illumination or environmental stresses. Further work investigating the role of europium in perovskite synthesis kinetics is needed to establish methods for increasing crystalline domain size while preserving improved optoelectronic and microstructural quality. Finally, though we have investigated the local role of europium in an inorganic perovskite, a wide range of halide perovskites incorporating lanthanides in quantum dots and thin films have been shown.[119, 122, 123] The bulk behavior of devices under study is generally of greatest interest and the figure of merit, but may overlook key aspects of local interactions between the ionic species of the additive and the host lattice, whether from elemental segregation, microstrain, or simply deviation between nominal and actual loadings of additives in strongly performing samples. Microscopic understanding of the compositions and structure must be established to understand their true tradeoffs and implications, especially for long-term device stability.

4.4 Conclusion

We investigate the microstructural underpinnings of the enhancements brought by europium addition to perovskite optoelectronics. The electronic quality of Eu:$CsPbBr_3$ is improved to yield an increased fraction of band-to-band recombination and fewer shallow traps, as evidenced by the increase in photoluminescence intensity and decrease in emission bandwidth. We use scanning X-ray nano-diffraction to show that these improved emission characteristics appear correlated to a reduction in microstrain at the nanoscale. Despite having a multicrystalline

microstructure, the europium-added samples have less microstrain and exhibit less mosaicity than pristine $CsPbBr_3$. The reduced nanoscopic structural disorder corresponds with greatly improved radiation hardness of Eu:$CsPbBr_3$. The improved luminescence yield and increased stability make Eu addition a promising strategy for the engineering reliable photodetectors across the electromagnetic spectrum, including X-ray and gamma-ray detectors - an application for which inorganic perovskites have shown significant promise.[131]

4.5 Acknowledgements

Chapter 4, in part, is a reprint of the material "Europium Addition Reduces Local Structural Disorder and Enhances Photoluminescent Yield in Perovskite CsPbBr3" as it appears in Adv. Optical Materials, Quinn, X. L., Kumar, R. E., Kodur, M., Cakan, D. N., Cai, Z., Zhou, T., Holt, M. V., and Fenning, D. P. 2002221 (2021). The dissertation author was one of the primary investigators and authors of this material. The dissertation author performed the synchrotron measurements and all data analysis described in this material.

Chapter 5

Accounting for Sample Morphology in Correlative X-ray Microscopy via Ray Tracing

5.1 Introduction

A variety of modeling tools are available for simulating the beam propagation to the sample plane in synchrotron experiments built on top of ray-tracing solvers, of which SHADOW (currently SHADOW3) is most widely used.[132, 133, 134] Though these tools give an accurate estimate of the beam profile at the sample plane, a critical missing component for the experimentalist is simulating the propagation of this beam through a heterogeneous sample and subsequent signal generation. No available tools to our knowledge address the issue of spatially-variant probe-sample interactions. To address this challenge, we present a morphology-informed ray tracing approach to simulate probe-sample interactions in raster scanning measurements, allowing for a first approximation of matrix effects and spatial correlation of the data acquired across scanning synchrotron-based and optical microscopy setups. As a demonstrative example we analyze structure-function correlations in sequential microscopy data acquired for a Eu:$CsPbBr_3$ halide perovskite thin film crystal [126] in three distinct measurement modes, each with its own measurement geometry: nanoprobe X-ray diffraction (nXRD), nanoprobe X-ray fluorescence (nXRF), and normal-incidence confocal micro-photoluminescence (μPL) [78]. First, we estab-

lish a three-dimensional (3D) model of our sample with nanoscopic accuracy using 3D optical profilometry. Next, each measurement geometry is defined for simulation by the orientation of the incident photon probe, sample, and involved detectors. We then perform ray tracing of the X-ray beam propagation within our sample, accounting for attenuation of incident and detected photons within the sample. Ray tracing generates a "sample point-spread function" (sPSF) that encodes the weighted contribution of sample volume to the signal recorded at the detector during each mode of measurement (i.e., scattering and fluorescence). By accounting for local geometric effects in our measurements, we correct the nXRF and nXRD data for attenuation and improve the precision of the spatial correlation across our three modalities. Such precise assessment of sampling volume and matrix effects in correlative measurements will be increasingly necessary as the volume and complexity of multimodal studies increases at upgraded and next-generation synchrotron facilities.

5.2 Methods

5.2.1 Synchrotron X-Ray Fluorescence and X-Ray Diffraction

Nano-XRF and nano-XRD were both acquired at the 26-ID-C beamline at the Center for Nanoscale Materials and the Advanced Photon Source at Argonne National Laboratory, using a focused 10 keV x-ray beam (beam waist ¡200 nm). Fluorescence maps (500 nm step size) were acquired with the sample oriented such that the sample substrate normal is 20° off the incident beam axis. The fluorescence detector, oriented 90° off the incident beam axis, was calibrated using NIST XRF standards (NBS1832, NBS1833). Local d-spacing of the pseudocubic (600) plane was determined by performing a spatially-resolved rocking curve (500 nm step size) in the Bragg condition, where the incident and detector angles were held constant while the sample theta was rotated in 0.25° increments. The 2D scattering detector was calibrated by measurement of a powder silicon reference sample. This procedure enables complete reconstruction of the 3D scattering vector at each point.

5.2.2 Defining the Simulation Volume

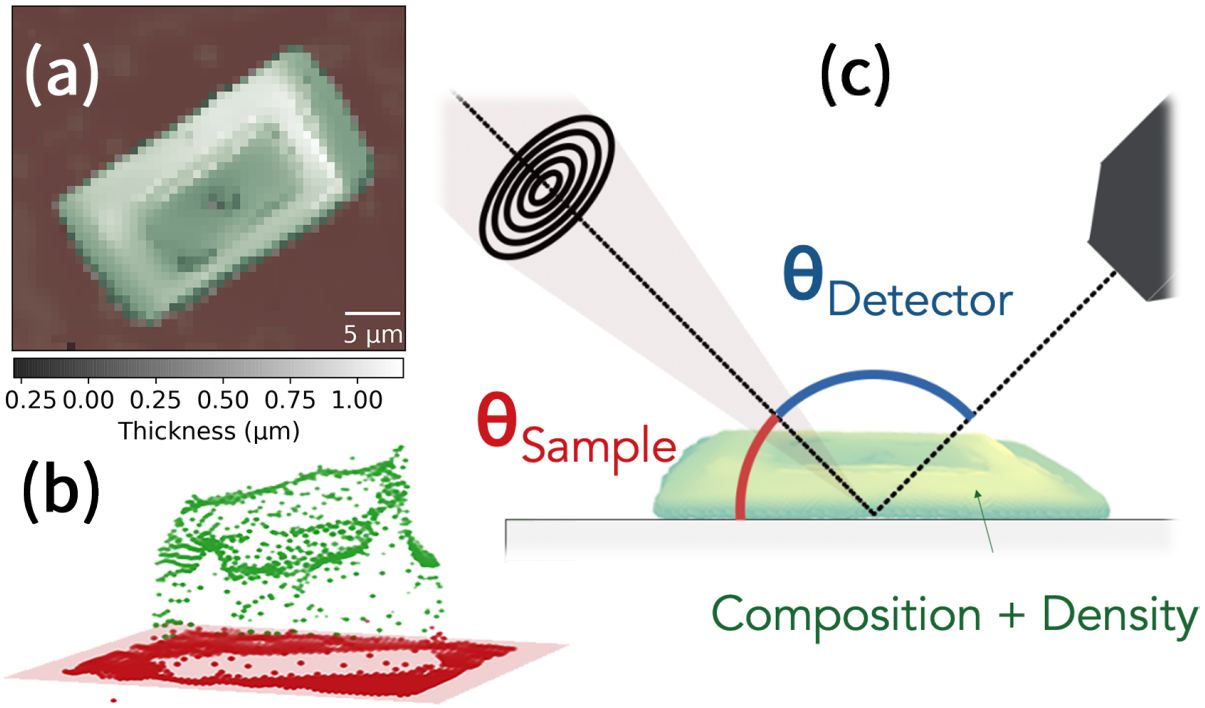

Figure 5.1. *Generation of 3D Sample Volume from Profilometry Data*: (a) Profilometry data of our isolated Eu:$CsPbBr_3$ crystal. False coloring indicates sample (green) and background (red) regions. (b) The surface profile of the crystal (green) after removal of the background baseline (red). (c) Three-dimensional solid body model of the crystal formed by extrusion of the green points, along with the material properties and measurement geometry parameters required to define the ray-tracing simulation.

The topography of the crystals was measured with a Filmetrics Profilm3D in White Light Interferometry mode with 50x magnification at lateral resolution of 100 nm and a vertical resolution of 0.1 nm. We construct a 3D model of our sample from this profilometry data (Figure 5.1, detailed procedure given in the Supporting Information). The instrument geometry is defined by the Euler angles of the incident beam and the detector axis with respect to the sample. Our synchrotron measurements utilize a nanoprobe with a beam waist of ¡200 nm. As such, we treat both the incident probe and signal photons as pencil beams propagating in the directions defined by the Euler angles. The simulation mesh is generated by interpolation of the sample model onto a mesh scaled to match the highest resolution dimension (in our case,

the z-dimension), generating more points along the coarse lateral dimensions. The mesh is then extended in the xy-plane to accommodate the lateral projection of the incident beam trajectory.

5.2.3 Ray Tracing

Algorithm 1: Trace an Incident Beam

Result: Beam intersection points for measurement at (x,y)

define $l_{step}, \theta_{incident}, \theta_{detector}$

z = z_{max}

incidenthits = [] ;

exithits = [] ;

while z $\geq$ 0 **do**

  if (x,y,z) is in sample **then**

    incidenthits.append([x,y,z]);

    exithits.append(traceexitbeam(x,y,z));

  end

  x -= $l_{step}\cos(\theta_{incident})$

  z -= $l_{step}\sin(\theta_{incident})$

end

return incidenthits, exithits

Algorithm 2: Trace an Exit Beam

Result: Beam intersection points for exit ray spawned at at (x,y,z)

define $l_{step}, \theta_{incident}, \theta_{detector}$

$m_{sample} = bool$

exithits = [] ;

while $z \leq z_{max}$ **do**

  if (x,y,z) is in sample **then**

    exithits.append([x,y,z]);

  end

  x += $l_{step}\cos(\theta_{incident})$

  z += $l_{step}\sin(\theta_{incident})$

end

return exithits

Algorithm 3: Calculate Measured Signal

Result: Measured signal at (x,y) for incident photon energy $E_{incident}$ and signal photon energy E_{signal}

define l_{step}

$T_{incident} = e^{-\mu(E_{incident})l_{step}}$

$A_{incident} = 1 - T_{incident}$

$T_{signal} = e^{-\mu(E_{signal})l_{step}}$

incident = 1

signal = 0

for hit in incidenthits(x,y) **do**

  incident *= $T_{incident}$

  this signal = $A_{incident}$

  for signalhit in hit **do**

    this signal *= T_{signal}

  end

  signal += this signal

end

return signal

For each lateral coordinate (x, y), a single ray is simulated starting from the top of the simulation mesh (x, y, z_{max}). As this ray propagates along the incident direction with a step size d_{step}, two events occur for each step where the ray intersects the sample: the intersection is recorded, and a signal ray is spawned. The signal ray similarly propagates towards the detector until $z = z_{max}$, and the total number of steps where the sample is intersected is recorded. A schematic of one ray simulation is shown in Figure 1g. The full algorithm is formalized in Algorithms 1,2, and3.

5.2.4 Estimating Self Absorption

We approximate the X-ray attenuation coefficient μ within our sample for relevant photon energies by the material's density and nominal average elemental composition.[135] The attenuation coefficient is applied to the intersection points tabulated during ray tracing, with each incident ray starting with unit intensity and each signal ray starting with the intensity lost from the incident beam in one step (Algorithm 3). The fraction of the "true" fluorescence signal as measured for each lateral coordinate is taken to be the sum of all final signal ray intensities at that coordinate. Measured fluorescence values are then divided by this fraction to remove self-absorption effects. By separating the expensive ray tracing from the attenuation calculations for each element's signal, we quickly apply the ray tracing results to fluorescence data for elements with different emission energies.

5.3 Results and Discussion

Correcting Fluorescence Data for Self-Absorption

We first validate our ray tracing approach by comparing simulated and measured X-ray fluorescence signals acquired in two different sampling geometries. Simulated and measured cesium XRF data collected from the same Eu:$CsPbBr_3$ sample in Bragg nXRD and nXRF geometries are shown in Figure 5.2a-f. Cesium XRF intensity is simulated by assuming that the cesium concentration is constant across the volume of the microcrystal, a fair assumption in our largely-single-crystalline sample.[78, 126] The simulations capture the crystal's hopper morphology [136] and, especially, the horizontal smearing by the beam projection in the shallow Bragg geometry (Figure 5.2c,e). Sharper contrast in the simulated maps can be attributed to our pencil beam assumption. This would be reduced by expanding the ray tracing model to account for the angular distribution of incident photons defined by the zone plate numerical aperture, finite tails of the probe shape, and the solid angle of collection of the detectors.

Ray tracing the incident and emitted photons in the X-ray fluorescence measurement

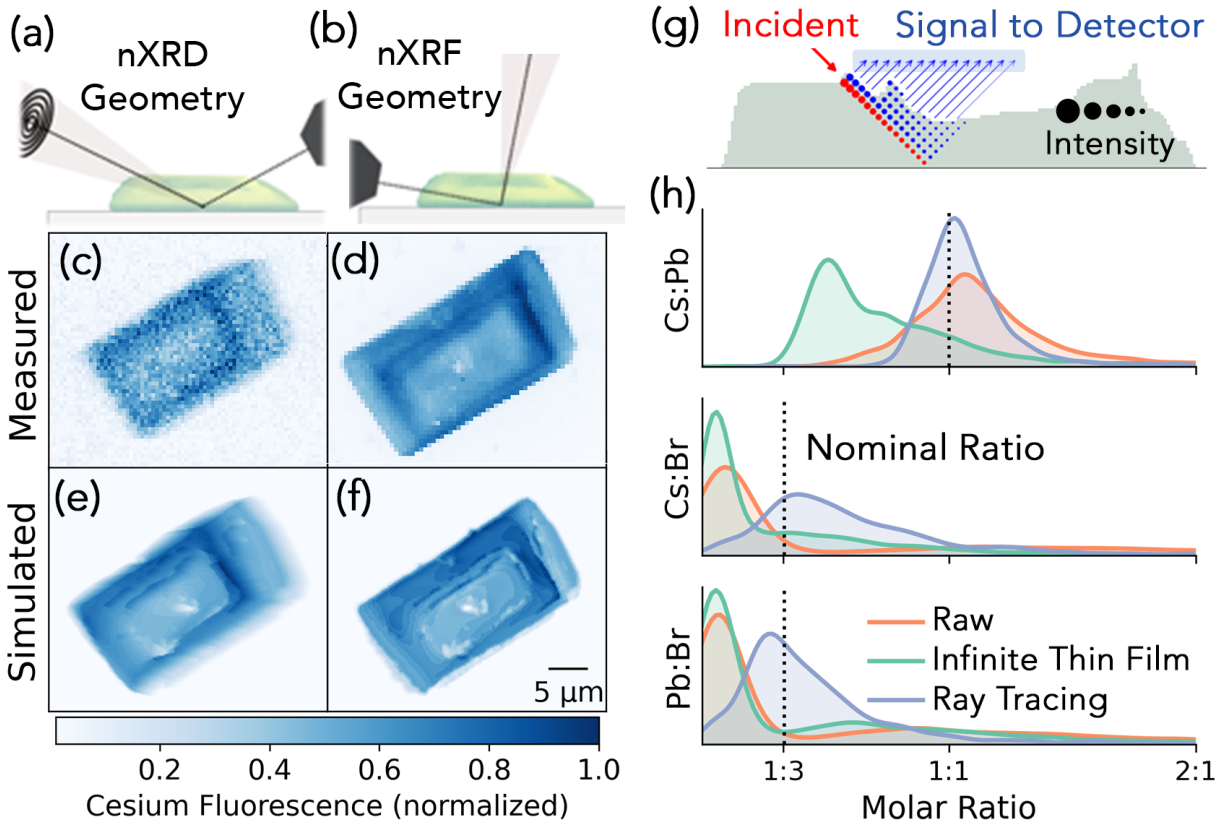

Figure 5.2. *Raytracing Simulation*: Instrument geometries where nano X-ray fluorescence was collected: (a) a correlative Bragg scattering configuration (a) and a geometry optimized for only nano X-ray fluorescence signal, with respective simulated (c,d) and measured (e,f) cesium fluorescence maps of the Eu:$CsPbBr_3$ thin film crystal. (g) Single-ray example of the ray tracing process showing the incident ray and all collected signal rays. (h) Distribution of raw, thin-film corrected[13], and ray-trace corrected molar ratios measured in the fluorescence-optimized geometry. The dashed vertical line shows the nominal composition ratio.

enables correction for self-absorption.[137, 138] The degree to which the raw fluorescence data is affected by self-absorption depends on the sample composition and the path length of photons within the sample (Figure 5.3). West et al. formalized an effective process for self-absorption correction in planar thin-film samples, where these path lengths are well defined.[81] The geometric assumptions made in their process do not apply to our rough, anisotropic crystal. By raytracing, we extend the analysis of West et al., accounting for varying path lengths across the sample. The molar ratios of the major components in our perovskite microcrystal converge to the

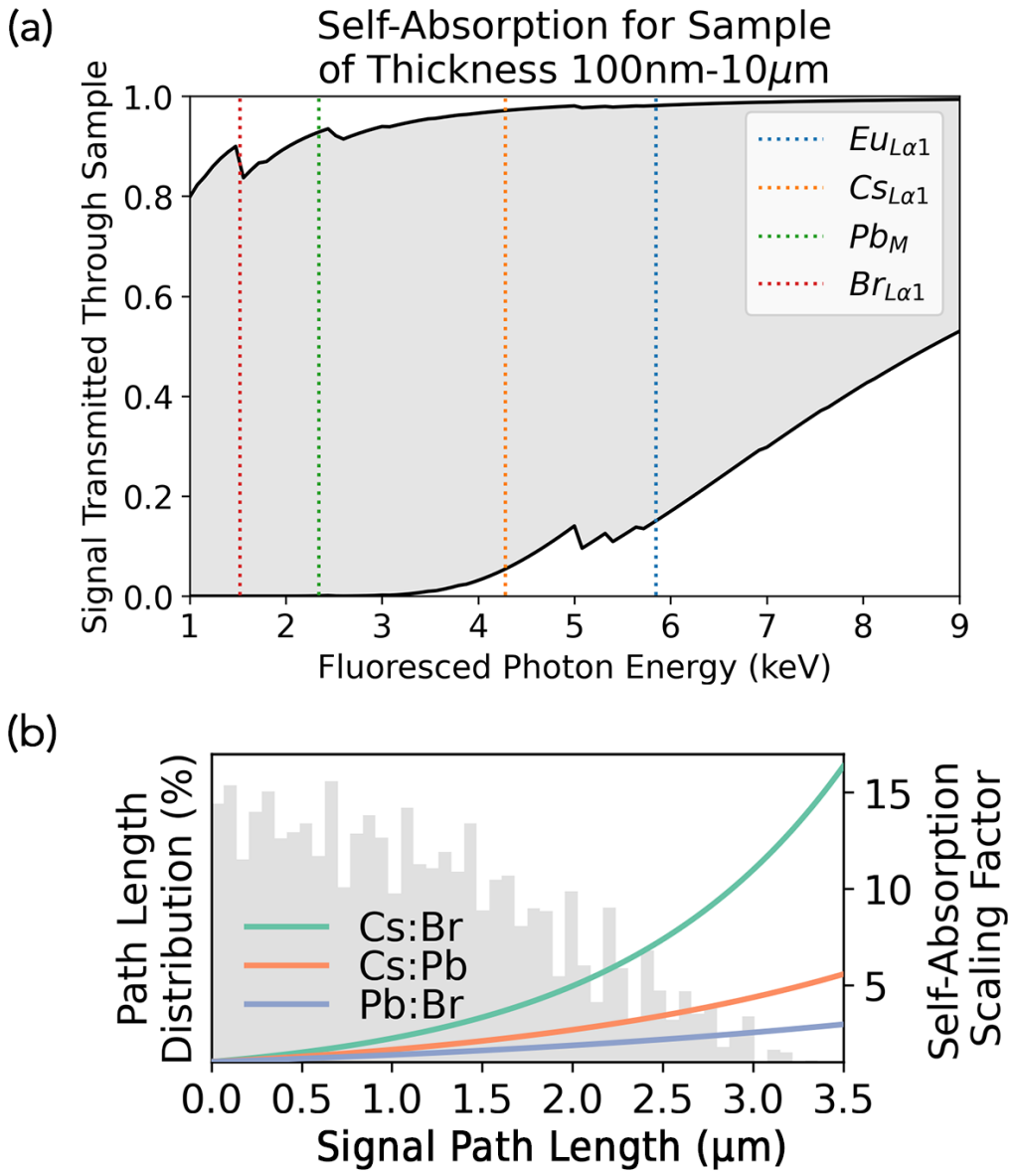

Figure 5.3. *Effect of Path Length on Self-Absorption Correction of Fluorescence Signal*: (a) The fraction of fluorescence signal transmitted through our perovskite sample to the detector for optical path lengths ranging from 0.1 to 10 μm. Emission energies for the four elements of interest in our sample are indicated. (b) A histogram of fluorescence signal path lengths as recorded from ray tracing in the nXRF geometry. The three overlaying traces indicate the degree to which molar ratios between majority elemental species in our sample are skewed in the raw fluorescence data as a function of signal path length.

expected stoichiometry after correction by our ray tracing approach (5.2g). The distribution tails are also reduced, as lateral variations in self-absorption (from the position of the fluorescence

detector to the left of the sample) are corrected. We note that our quantification of bromine content is made using the $Br_{L\alpha}$ line, the low signal of which contributes to broad distributions of molar ratios involving bromine.

5.3.1 Accounting for Geometric Differences via Convolution

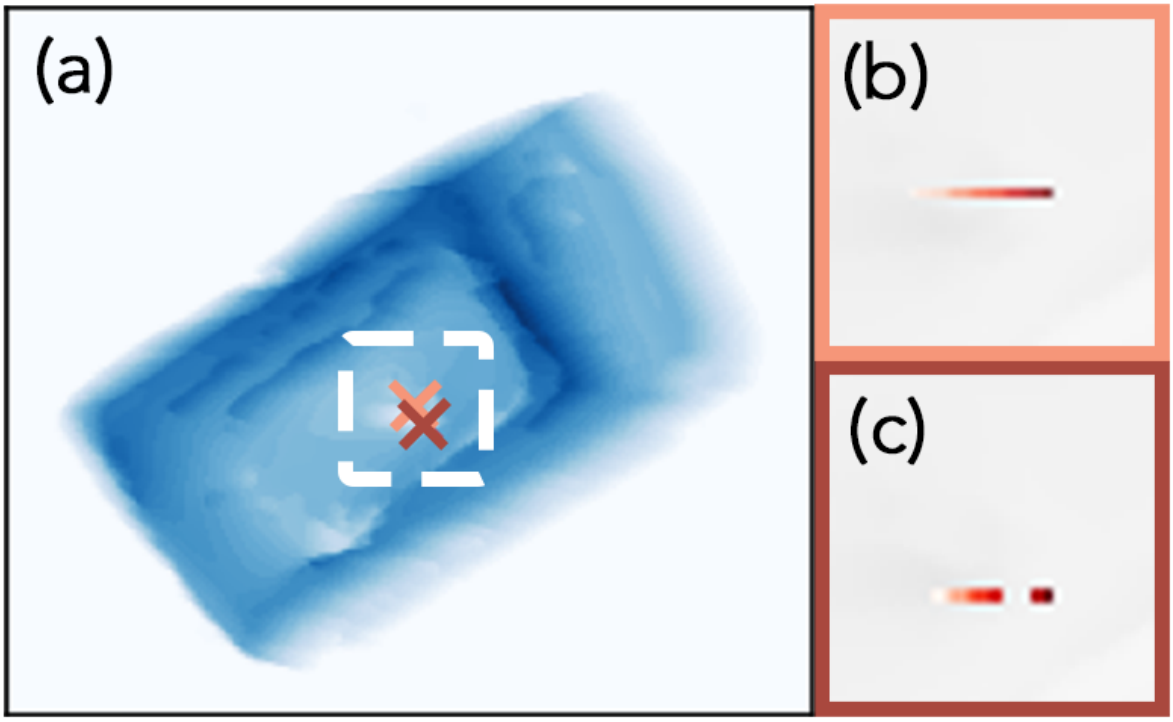

Figure 5.4. *Example Sample Point-Spread Function*: Local sample point-spread function (sPSF) for two points on the sample, marked in (a), are shown in (b) and (c).

Ray tracing returns not only the relative signal measured for each pixel in our spatial dataset, but the points in the sample from which that signal is generated. The ray-tracing simulation assembles a rank five tensor where each coordinate (x,y) holds the local sample point-spread function $sPSF(x,y,z)$, a sparse 3D mask encoding the weighted contribution of each point in the sample to the total signal recorded at the detector for coordinate (x,y). As the nXRF, nXRD, and μ-PL data are sampled only in the two lateral dimensions in the plane of the thin film crystal (all signal generated in the dept of the sample is projected into 2D), we

integrate the sPSF along the Z-direction. Examples of local sPSF's from the nXRD geometry are shown in Figure 5.4. In our case, we measured our perovskite crystal sequentially in three mapping measurements: nXRD, nXRF, and μPL. sPSFs were determined for the nXRD and nXRF geometries. The μPL sPSF sPSF was set to the identity matrix, as the optical path of the confocal microscope used is normal to the sample and incurs no lateral projection. We can use the resulting rank four tensor, which describes local 2D convolution, to better analyze the correlations between our 2D mapping data from different modalities. Even perfectly registered maps encode information from different sample volumes owing to the geometry differences and the differing light-matter interactions at hand with the change in photon energies. The raytraced sPSF enables a more precise comparison across multiple measurements with varied interaction volumes.

All raw measured data can be thought of as a convolution of the true sample nature by the sPSF. Deconvolution of the sPSF from the raw data would recover the map of the sample properties at the highest sampling resolution. In practice, the noise level of experimental data prohibits a deconvolution approach. This issue is further exacerbated by the spatially-variant nature of our PSF. Existing algorithms for spatially-variant deconvolution hinge on finding sections with multiple constant-PSF chunks, whether by recovering the image in sections with constant PSFs and stitching or by decomposing the spatially-variant PSF into eigenfunctions and continuously varying their eigenvalues across the image area [139, 140, 141, 142]. These methods may be applicable for samples with periodic features and thus a small number of unique local PSFs, but for general cases these algorithms may not suffice. A simpler (albeit less satisfying) approach to reconcile sampling volume differences across datasets is to convolve each dataset by the sPSF of the others (Figure 5.5a). Though the spatial resolution of each individual image is reduced, the total data is now equivalently convolved and can be compared pixelwise. Applied to our nXRF, nXRD, and μPL datasets, this forward convolution treatment reveals local correlation of composition, microstructure, and optoelectronic quality across a microstrain gradient observed in the nXRD (Figure 5.5b). Note that, applied to 2D data like ours, the sample

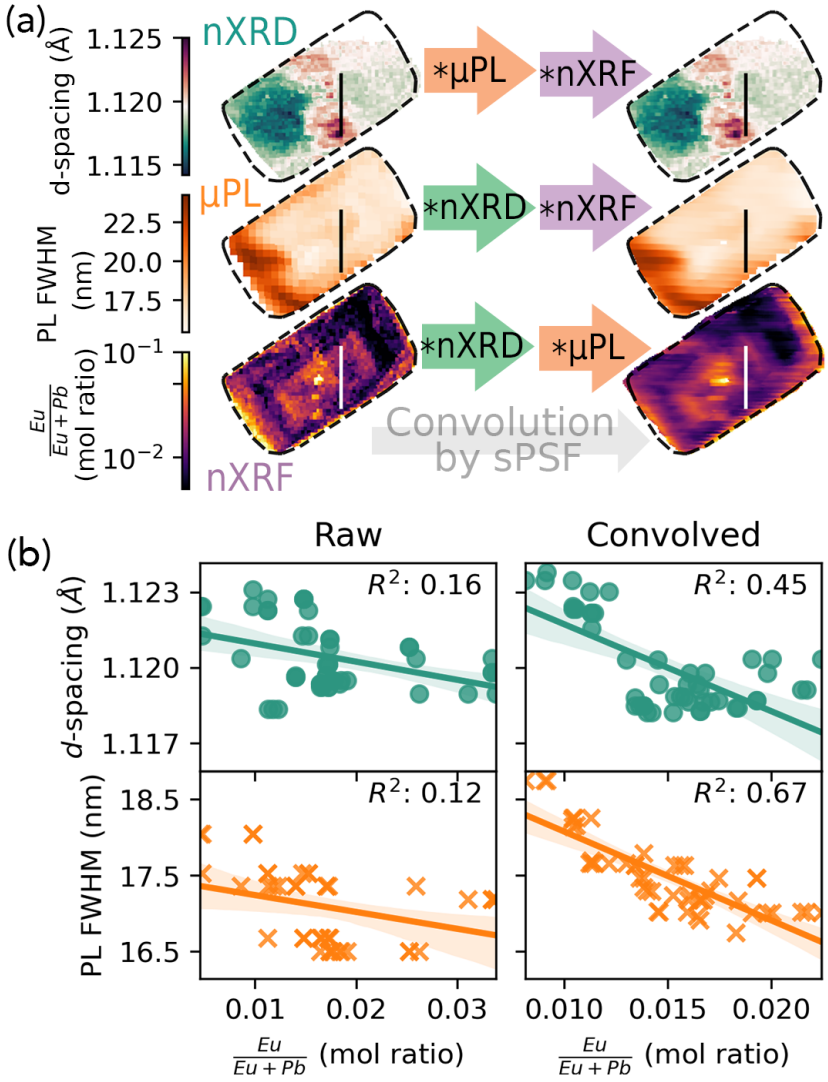

Figure 5.5. *Convolution of Measurement Modalities by Sample Point-Spread Functions*: (a) Convolution of each of the nano X-ray diffraction (nXRD), micro photoluminescence (μPL), and nano X-ray fluorescence (nXRF) data by the sample point-spread functions (sPSF) from the other data geometries yields equivalently convolved images. (b) Pixelwise correlation of the d-spacing from nXRD and the μPL full-width half-maximum (FWHM) with the local europium content from nXRF along the vertical lines in (a). Linear fits (solid lines) and associated R-squared values are shown for each correlation both before (left) and after (right) convolution. The shading represents 95% prediction intervals.

information is implicitly compressed into the two lateral dimensions despite rays being traced in three dimensions. This shortcoming continues to wane as advanced techniques and dedicated hardware capable of resolving material structure [143, 144, 145, 146, 147, 148, 149, 150] and

composition [74, 90, 151, 152, 153, 154, 155, 156, 157] in three dimensions proliferate across upgraded synchrotron facilities. These 3D techniques also carry unique interaction volumes that must be considered in comparison across modalities, for which our approach can be employed to mutually convolve the data modalities in 3D. Still, these techniques are not always feasible as they require specific hardware, often incur large photon doses that prohibit sensitive samples, and, in the case of tomography, may be difficult to apply to extended thin samples such as ours. [158, 159] Regardless of the raw data dimensionality, the forward-convolution approach allows for a morphologically informed comparison across modalities.

5.3.2 Caveats and Further Considerations

Our ray tracing approach does not take any secondary photon interactions into account. The validity of this simplification depends on the sample under study. For large, highly crystalline samples measured in a Bragg condition, dynamical scattering may significantly alter the transmission of x-rays through the sample. [135, 160] Samples of high-Z compositions may also be subject to secondary fluorescence. [161, 162] Each of these phenomena will modify the sPSF and the resulting convolutions of the data.

Self-absorption correction adjusts estimates of local composition, which in turn adjusts the expected degree of self-absorption. This suggests that an iterative solver with alternating updates to the composition and self-absorption factors could be employed to converge towards the true local composition. In our specific case this approach is not required. We have high confidence that in our high-quality crystalline sample (not a polycrystal), the local content of all elements other than lead and europium (the dopant species) are constant, and self-absorption differences between compositions at the extreme ends of our measured Pb and Eu stoichiometry only generate a 1-4% difference in our molar ratios of interest (Figure 5.6). Development of iterative composition solvers will be important for the study of samples with poorly constrained composition, especially in dense correlative datasets as generated in diffraction-limited and/or tomographic experiments at next-generation synchrotron facilities.

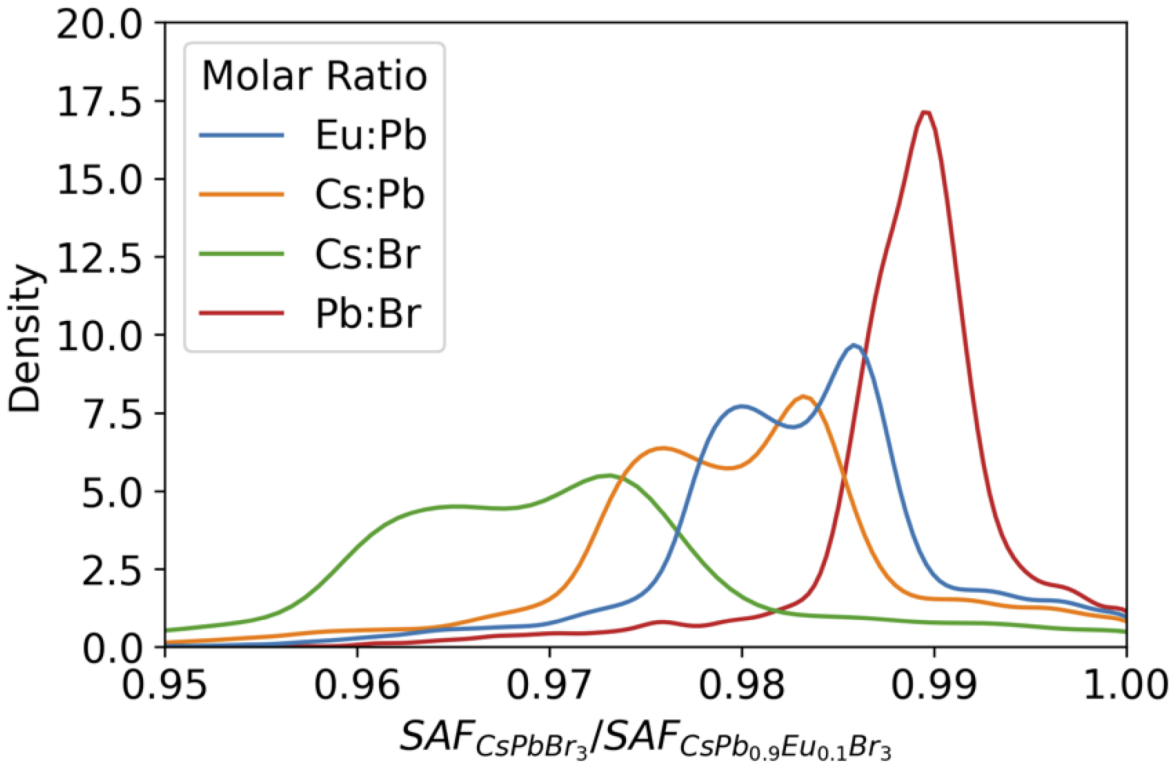

Figure 5.6. *Effect of Composition on Self-Absorption of Fluorescence Signal*: Effect of sample composition on molar ratios after self-absorption correction for points across the sample area. The compositions are selected as the extreme ends of compositional variation based on measured composition. The distribution of values results from the variation in path lengths across the sample.

5.4 Conclusion

To realize the full power of multimodal correlative microscopy studies, the nuances of each individual mode must be accounted for. Even in a simultaneous measurement with multiple detectors, the data acquired at each detector is subject to different geometric effects within the sample. We have shown that even a simple ray-tracing approach employing pencil beams and Beer-Lambert attenuation can correct for self-absorption effects in X-ray fluorescence measurements, allowing quantitative compositions to be extracted from highly anisotropic samples. Ray tracing also generates a sample point-spread function encoding the local probe-sample interaction volume for each pixel in spatially-resolved mapping or imaging measurements,

which can be used to reconcile the sampling volume differences across datasets. We show that jointly convolving the multimodal datasets with the sample point-spread function of each is a simple yet effective way of bringing spatial data into the same frame for comparison. Future development in flexible and noise-tolerant deconvolution algorithms, especially recent efforts leveraging machine learning [163, 164, 165], may make deconvolution more tractable. The ray-tracing approach described here can be improved in many ways, such as accounting for the shape and angular range of the incident probe, the collection angle of the detector, and second-order effects in modeling probe-sample interaction (e.g. secondary fluorescence). We envision future tools for rigorous simulation of probe-sample interactions to be built on standard ray-tracing engines like SHADOW [133] and incorporated into simulation platforms like OASYS [132] to enable end-to-end simulation of multi-modal experiments from probe to detector that maximizes the ability to make scientific inference from correlative microscopy data. The promising results from our preliminary efforts prove that these tools will bring practical benefits to multimodal studies, particularly when techniques involve long path lengths such as in X-ray and neutron experiments.

5.5 Acknowledgements

Chapter 5, in part, is a reprint of the material "Accounting for sample morphology in correlative X-ray microscopy via ray tracing," MRS Advances, Kumar, R. E., Quinn, X. L., and Fenning, D. P. (2021). The dissertation author was the primary investigator and author of this material.

Thank you to Moses Kodur at UC San Diego for his help in taking the μPL data, and to Tao Zhou, Martin V. Holt, and Zhonghou Cai from the Center for Nanoscale Materials at Argonne National Laboratory for their assistance during and valuable discussion about our synchrotron measurements. This work was supported in part by the National Science Foundation under Grant No. DMR-1848371. Use of the Center for Nanoscale Materials and the Advanced Photon Source,

both Office of Science user facilities, was supported by the U.S. Department of Energy, Office of Science, Office of Basic Energy Sciences, under Contract No. DE-AC02-06CH11357. This work was performed in part at the San Diego Nanotechnology Infrastructure (SDNI) of UCSD, a member of the National Nanotechnology Coordinated Infrastructure, which was supported by the National Science Foundation (grant ECCS-1542148).

Part III

High Throughput Screening of Halide Perovskite Solar Absorbers

Chapter 6

The Perovskite Automated Spin Coating Assembly Line (PASCAL)

6.1 Comparisons to Existing Work

Lab automation has seen the greatest market penetration in biology research, specifically in drug discovery research. Liquid handlers are used at scale to prepare small-volume mixtures of potential drug molecules and their targets at various concentrations to evaluate their interactions. Most steps of the drug discovery pipeline are now automated, with sample preparation, heating steps, filtration steps, and characterization steps being performed by automated tools. Many efforts to automate research in other fields have begun with the arbitrage of mature components from biological lab automation platforms. Liquid handling, therefore, is treated as a solved problem for automation purposes. Still, materials science automation often requires tools and processing windows outside those of biological experiments.

In the case of halide perovskite automation, there are two major differences from biological automation that drive hardware design: the film deposition process, and the use of solid samples on glass slides instead of liquid samples.

The majority of halide perovskite thin films are fabricated using spin-coating, a design decision that is carried through the two other perovskite automation platforms that exist worldwide. [166, 167] Blade-coating, an alternative thin-film deposition method which may in fact become more relevant to perovskite research as it is more amenable to production at scale, is

not currently incorporated in any automation platform for halide perovskites. It is, however, the central step of an automation platform at Argonne National Lab designed to fabricate and test thin films [168]. In design of an automated platform for halide perovskite research, we must construct hardware to fabricate thin films.

Regardless of the method chose for film fabrication, the samples will be made on rigid slides that must be moved from one location to another. This necessitates the use of a robotic arm with an end effector capable of carrying glass slides. There are numerous robot arm designs that will be compared later, but the end effector design will generally fall into one of two strategies: using fingers to clasp the edges of the sample, or using vacuum to attach to the surface of the sample.

Beyond these two core components, hardware needs will depend entirely on the experimental parameters and potentially characterization that one wants to include. For halide perovskites, some form of heating is necessary to anneal samples after spincoating, of which both hotplates [167] and furnaces [166] have been employed in existing platforms. Characterizations for halide perovskite materials primarily probe optical properties and film quality, so spectroscopic and imaging methods are of interest.

6.2 Hardware Considerations

6.2.1 Liquid Handling

We chose to use an Opentrons OT2 liquid handler for our platform, primarily for cost and ease of integration into the rest of the platform. First, the OT2 is an economical choice, with total cost of ¡$10k as opposed to ¿$20k for competing platforms from industrial players like Tecan and Hamilton. More importantly, the OT2 runs off of Python code and its operation can be highly customized, which is critical for our custom application.

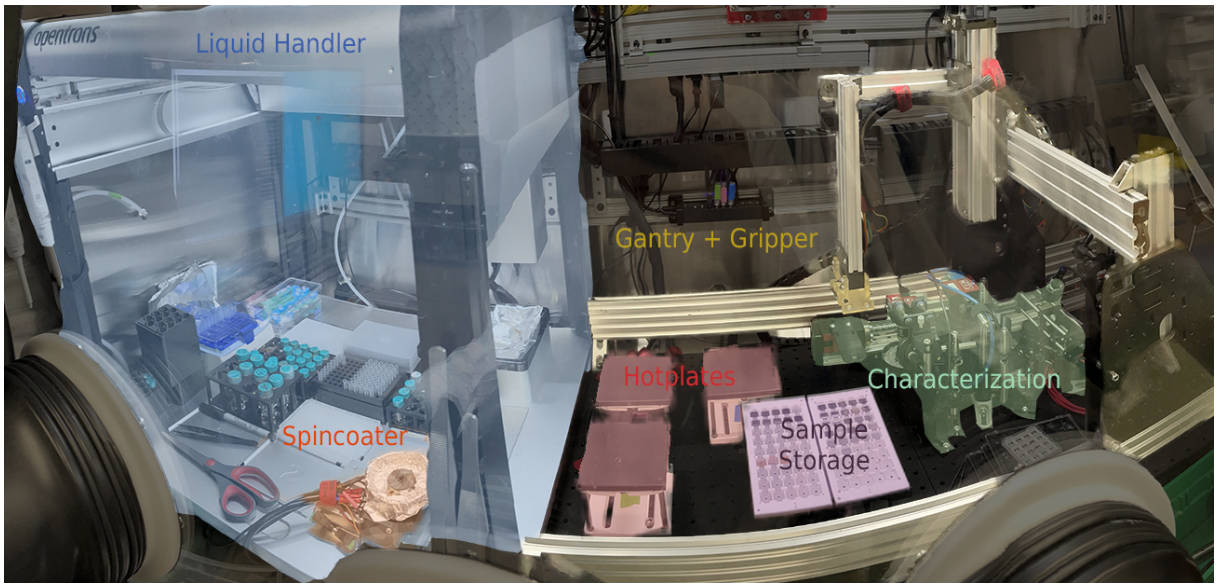

Figure 6.1. The Perovskite Automated Solar Cell Assembly Line (PASCAL), with the various hardware modules highlighted and labeled. The entire system is contained within a nitrogen glovebox.

6.2.2 Spin Coater

Our spincoater consists of a hollow-shaft brushless DC motor, an ODrive brushless motor driver, a machined aluminum base, and some 3D-printed parts (the spincoating chuck, the shroud to catch solution spraying off of the substrate, and some mounting components).

Beyond the typical design considerations of a spincoater (pull vacuum on the chuck to hold the sample, sufficient rotational top speed, acceleration, etc.), our application must satisfy one major extra constraint: we must be able to rotate the chuck to a known orientation. This is because our gripper lacks a rotational degree of freedom about the z-axis (ie a wrist), and it must pick and place a square glass substrate on the chuck. Therefore, we must be confident that the chuck starts and finishes in the same orientation such that the parallel grippers contact the slide properly when picking up the sample. We satisfy this constraint by attaching an indexed rotary encoder to the motor shaft. This design choice necessitated a ”closed-loop” motor controller (such as the ODrive) which tracks the rotor *position* as opposed to an ”open-loop” controller (like a typical electronic speed controller [ESC]) which tracks the rotor *rotational velocity*.

The aluminum base has three major design objectives. First, it must hold the chuck normal to the work surface, stably up to high rotational velocities. In practice, I simply had the chuck machined out of a solid block of aluminum large enough to not worry about shifting from vibrations at high rotational velocities. Second, it must provide an airtight path through which to pull vacuum on the chuck. To do so, I had a channel machined to connect the center of the motor's mounting position to a 3/8N̈PT tapped hole on the side of the base. A shallow 1 cm groove is positioned to fit a greased rubber o-ring between the flat base of the motor and the aluminum base, completing the seal so vacuum does not leak at this joint. Finally, the base must couple to the standard deck slots of our Opentrons OT2 Liquid Handler. This forces the block to be slightly larger than required (footprint of 85.5 mm x 127.8 mm).

A later iteration of the spincoater implemented a 40x40 mm fan to constantly blow across the brushless motor. We found that the motors would occassionally burn up under long operating durations. I expect that this was an issue of overheating (ohmic heating, as the motor windings carry amps of current under normal operation) melting the wire insulations, leading to shorts that damage the motor. After the fan was installed, no motors burned out after even many hours of spincoating with a 50% duty cycle.

6.2.3 Sample Transfer

For the transfer of samples on glass slides between stations, we need a robot (to move the samples around the platform) with an end effector (to pick up and put down samples).

Motion

The robot arm design follows from both hard and soft constraints. First, the precision, accuracy, and repeatability of our robot must be sufficient for our application. In our case, we require precision and repeatability ¡0.1 mm to ensure that the glass slides are placed in their expected positions. Accuracy is less of an issue since we will calibrate the coordinates of each station in the platform, but once precision and repeatibility constraints are satisfied, the

accuracy generally follows. Second, we must be able to utilize the rectangular footprint inside our glovebox, and be able to reach the robot into the liquid handler to move samples to and from the spincoater. Third, the hardware and implementation should be as simple as possible, as this system will be maintained by materials scientists and chemists who should not be expected to have a working understanding of complicated robotic systems.

To satisfy these criteria, we opted for a cartesian robot (moves in x,y,z directions). The three axes are driven by stepper motors. The x and y dimensions are direct-drive and employ a belt, which allows for the motor to move the gantry along long distances defined by the belt length. The robot does not support any load in the x or y directions, and does not need to accelerate very quickly, so any loss in responsiveness or accuracy from belt stretching during operation is not an issue. The z dimension, however, does need to support the load of the arm and gripper, and therefore uses a lead screw. The gripper is mounted at the end of an arm which extends for about 10 inches towards the spincoater and 10 inches towards the floor of the workspace. The horizontal extension is to translate the accessible workspace volume into the liquid handler, enabling the gripper to access the spincoater. The vertical extension enables the y and z axes to be translated up, providing more space for the characterization and other hardware while allowing the gripper to reach towards the floor of the workspace. Cost and complexity aside, a six degree of freedom robotic arm on a linear track would have been a better choice for our system. In fact, such arms are a growing standard in laboratory automation, and are employed in the other perovskite automation platforms. Our robot, however, was constructed for about $500 using hobby grade aluminum extrusion and electromechanical components and 3D-printed parts. Additionally our design was chose to simplify implementation and future expansion or repairs. The cartesian control simplifies path planning algorithms (as opposed to the inverse kinematics or radial controls required for robot arms with radial joints), which are not a focus of our work or within the expertise of our lab. Our simple robot is controlled using an off-the-shelf 3D-printer control board (Bigtreetech SKR Mini E3 v2.0), which has open-source firmware and is controlled via G-Code.

Gripper

Once our robot arm can reach all required points in the platform, it must be able to manipulate the glass slides at these points. In doing so, we want to minimize the chance of damage to or cross-contamination of the materials deposited on top of the individual slides, which drove us away from a vacuum mechanism and towards a gripping mechanism. While suction is a more consistent option for manipulating glass slides, it requires contact on one of the flat surfaces (top or bottom) of the substrate. Contact from the top not possible after the top is coated with material, and contact from the bottom requires an exposed bottom surface at all points in the platform (as is the case in Ada at the Burlinguette lab [**?**]). All stations in our platform have flat bottoms that enclose the entirety of the substrates, ruling out a vacuum-based effector for our platform.

We opt for a parallel gripper, driven by a servo, with stainless steel fingers. The gripper fingers are attached by springs which pull the fingers towards one another. To open the gripper, the servo rotates, ensuring that the fingers are at the known open position as the outward force from the servo horn fights the inward force of the springs. To pick up a sample, the gripper is closed past the width of the sample (eg to pick a 10 mm samples, we set the gripper to put the fingers about 8 mm apart). This transfers all mechanical load off of the servo and onto the springs; servos under constant load are prone to overheating, at which point they do not operate properly. In this scenario, the load (measured as the current draw) on the servo can be measured to check whether a sample has been succesfully grasped, as this load should be near zero if the sample is grasped (servo is not fighting the springs), or high if a sample is not grasped (servo is fighting the springs). The fingers are made of stainless steel to be resilient to potential chemical exposure, and to maintain rigidity when picking hot samples directly from the hotplates.

6.2.4 Heating

All heating is performed on custom-build hotplates. We opted to build our own hotplates to improve space efficiency, improve temperature homogeneity across the plate, and to be remotely controllable by Python scripts. These hotplates are 4" x 4" aluminum tops with 3" x 4" heating elements, raised from the workspace floor with 4" stainless steel posts. The aluminum plates afford much greater temperature uniformity than the standard ceramic plates of commercial hotplates, and the resistance to acids granted by ceramic is not required for typical halide perovskite synthesis routines. Additionally, we separate the heating elements from the control elements, the latter of which are mounted to the wall away from the workspace. This improves the packing density of hot surfaces in the limited workspace.

6.2.5 Characterization

The PASCAL characterization train is designed to provide figures of merit for development of halide perovskite photoabsorbing layers. We use spectroscopy to measure optoelectronic figures of merit (material bandgap, photoluminescence intensity), and imaging to measure film morphology (roughness, coverage, and pinholes and spincoating defects).

Optical Characterization

We employ transmittance and photoluminescence spectroscopy to characterize the optical absorbance and radiative recombination behavior of thin films.

Both rely on a spectrometer to record light intensity across the visible spectrum. We selected the StellarNet Silver Nova spectrometer because it is thermoelectrically cooled (higher signal-to-noise ratio to detect faint luminescence), fiber coupled, and has a Python interface to ease integration into the greater platform. The light is collected from above sample using a 1" parabolic mirror, then passes through a plano-convex lens to be focused into a fiber optic cable. This fiber optic passes through a free-space coupling (Thorlabs U-Bench with collimators at the input and output ends) in which a filter slider has either an empty slot or a longpass filter. This

longpass filter is only insterted during photoluminescence measurements to block the excitation wavelengths from the spectrometer. to After the free-space coupling, the light is sent to the spectrometer.

For transmittance measurements, we couple a broadband halogen lamp into a fiber optic cable. This fiber optic terminates below the film, inline with the parabolic mirror above the film.

For photoluminescence (PL) measurements, one of two 0.9 mW lasers are shone onto the sample to excite carriers within the film and generate luminescence. These low-power lasers were selected to simplify the safety requirements of the setup; the lasers are rated as ”class 2”, and any lasers of class 3 or higher require safety controls such as interlocks and completely closed light paths that are not feasible in the constrained space of the glovebox allocated for these PL measurements. The two lasers are used for different measurements. The first is an unfocused red (635 nm) laser, which provides about 0.1 suns equivalent irradiance to the sample. This is intended to measure sample photoluminescence while minimizing the chance of damage or photoinduced changes to the sample. The first is a blue (405 nm) laser with a 2” focal length plano convex lens to focus the laser to a fine spot aimed at the focal point of the collection parabolic mirror. Focusing is not perfect, as the laser impinges on the sample at a decent angle (about 40off normal) to accomodate the 1” parabolic mirror. The effective irradiance is about 4-5 suns. This laser is used to elicit photoinduced changes within the sample as a metric for photostability.

Darkfield Imaging

We employ darkfield imaging for a measure of film morphology. This setup employes a silicon CMOS camera (Thorlabs), a 10X microscope objective, and an LED ring light. The ring light is positioned direcly below the sample (trans illumination), close enough such that no light enters the microscope objective. This way, the only signal reaching the camera comes from light scattered through the sample. Brightness in this image therefore represents morphological features (cracks, roughness, pinholes, etc) in the film that scatter light into the microscope

objective. The 10X objective provides an image with a pixel size of about 10 microns, making the darkfield camera an effective probe for macroscopic film defects, but likely insufficient to resolve nanoscopic pinholes in the film.

PL Imaging

The same darkfield imaging camera is used for photoluminescence intensity imaging as well. A blue (405 nm) LED lamp (Thorlabs) is positioned above the sample to excite carriers and generate photoluminescence emission from the sample. A 450 nm longpass filter (optical density of 4) is placed between the microscope objective and the camera's CCD to reduce signal from reflectance of the excitation source from the sample surface. We also remove the infrared filter from camera (these often come installed on RGB cameras by default) to allow greater sensitivity in detection of deep red to near-infrared emission as is common in narrower bandgap perovskites. The red channel of the RBG image is used for a qualitative metric of optoelectronic homogeneity across a film. This metric is qualitative, as intensity on the camera conflates PL intensity and wavelength by virtue of the wavelength-dependent sensitivity of the silicon CMOS detector.

Brightfield Imaging

A silicon CMOS camera and ring light (epi illumination) are used to take brightfield images of the samples. These are standard images with about a field of view of about 1", and are used to check for dropped samples or poor film coverage.

6.2.6 Glovebox integration

All of the hardware discussed above is installed within a nitrogen glovebox. We strove to move as much of the electronics outside of the glovebox to avoid corrosion from vapors released into the glovebox during spincoating and annealing steps. This is achieved by adding as many KF40 feedthroughs as possible, spread along the back wall and the ceiling to accomodate wiring in different regions of the glovebox. The only electronics inside the glovebox are the control board for the Opentrons liquid handler (a Raspberry Pi), the internal circuitry of the cameras, PID

controllers for the hotplates, and the spincoater chuck encoder, and the motors for the spincoater, gantry, and characterization stage.

All wiring to control the hardware is passed outside the glovebox through KF40 flanges. A total of 6 USB cables and 8 BNC cables allow for expansion in the future. Three DB25 cables carry data and power wires to control hardware. These include the endstops, encoders, and power wires to the stepper motors powering the gantry and characterization axis. The power wires to the spincoater are instead run through thick conductors (a three prong power extension cable), as the high current used to drive the brushless motor would burn out the PCB traces within the DB25 breakout cables.

Chapter 7

Roboflo: A Job Scheduler for Automated Experimentation Platforms

7.1 Motivation

Automation is becoming prevalent in laboratories across biology, chemistry, and materials science research. Laboratory robotics improve research throughput while freeing researchers from the burden of rote tasks. Further gains in throughput and efficiency of efforts is promised by Automated Experimentation platforms, which combine robotics and artificial intelligence to iteratively design, execute, and analyze experiments to achieve a research objective. [169] Automation, however, ”isn’t automatic”; there are many hurdles in the implementation of laboratory automation ranging from hardware design and integration to software tools for experimental planning tools and data analysis. [170] These hurdles are exacerbated by the fact that the skills they require lie outside of the domain of typical members of the laboratories for whom the tools are being designed. Fortunately, many of these issues are fundamental to lab automation, and general solutions will hopefully arise to ease the development of future automation platforms. Our goal with Roboflo is to provide one such general solution to a critical step in the automation pipeline – the scheduling of time-sensitive, coordinated tasks for execution by a set of hardware with limited capacities.

Throughput and efficiency are the primary value propositions of AE platforms. At its core, an AE platform consists of two components – robots to carry out experiments, and an artificial

intelligence (AI) agent to tell the robots what to do. Much of the gain in throughput promised by AE platforms lies in the efficient coordination of its robotic components, which alone can offer many orders of magnitude improvement in throughput. For the AI agent, generation of a single ”datapoint” multiple experimental steps for the robots to synthesize and characterize samples. Completing many ”datapoints” in parallel therefore requires the robots to juggle tasks across stations and experiments to maximize hardware utilization while ensuring that experiments are performed as defined by the AI agent. This is a classic optimization problem known as the ”job shop problem”. Implementations of these approaches vary on a case by case basis, and are not expected to be within the skillset of the primary users of AE platforms (ie domain scientists). The difficulty of job scheduling compounds as we imagine platforms under demand from multiple users. Such large-scale AE platforms, especially those set up at national user facilities, will be available for remote users to schedule their own experimental queries akin to high performance computing (HPC) resources available today. In this scenario, scheduling decisions must be made in realtime at the edge to fit in remote queries without compromising on the queries currently in progress.

Here we present Roboflo, a Python-based job scheduler tailored for AE platforms that abstracts (to the level of the experimentalist) the definition and solution of the job shop problem . Roboflo assumes that a set of independent workers act in concert to execute a set of tasks for a given protocol, in the process passing a sample from one worker to another to perform tasks. To use Roboflo, one needs to define: 1. a set of workers that can perform tasks, 2. a set of transition tasks to move samples between the workers, and 3. sets of tasks that should be completed in a certain order. Given these components, Roboflo formulates and solves a constraint-programming problem to provide a feasible schedule to complete the tasks. Roboflo’s flexible, abstraction-based definition of an AE platform allows for changes in hardware or capabilities to be easily reflected in the job scheduling. Finally, Roboflo allows tasks to be started at an arbitrary time, enabling tasks to be fit into an existing schedule as may be desirable in AI-driven closed-loop experiments or for shared AE platforms. We believe that Roboflo fills a common need for AE

platforms, and hope it can server as a standard backend for job scheduling.

7.2 Comparisons to Existing Work

7.2.1 The Job Shop Problem

The Job Shop problem is a classic problem in operations research. In this problem class, we have a set of jobs that must be executed in a certain order. Each job must be executed using some specific resource(s), each of which has a limited capacity. The objective of our solving algorithm is to minimize the ”makespan”, or the total time required to complete all jobs while respecting resource constraints. This problem is classified as NP-hard [171, 172, 173], meaning that the exact answer (ie the shortest schedule) cannot be retrieved for all combinations of jobs and resources. We can, however, retrieve approximations to this correct answer, which in practice is sufficient for our use case – we can retrieve a schedule that is feasible (no resource constraints violated) and has a reduced makespan than running all jobs in series (we get some parallelization). The operations research literature has provided a variety of algorithmic advances to solve this problem, making the solution of typical lab automation schedules problem not only possible but tractable to solve in reasonable timeframes (seconds to minutes). [174, 175]

7.2.2 Constraint Generation

While tools to solve the job-shop problem are now well established – we use OR-tools, an open-source package from Google [176] – the implementation of these tools can be tricky and requires skills outside the domain of typical experimentalists. Roboflo employs Constraint Programming Satisfiability (CP-SAT) to solve our lab automation schedules. [177] In the CP-SAT paradigm, jobs and resource utilization must be reperesented as a set of variables linked by linear equations and inequalities, with another variable representing an objective value that must be maximized or minimized. In our case, variables represent the starting and ending times of jobs, and inequalities force tasks to occur in desired sequences and resources to be used at or

below their maximum capacity. The objective value is the latest ending time for a given task, which we aim to minimize. The construction of this set of variables and constraints is highly dependent on the specific nature of tasks and resources for a specific lab automation scenario.

Our goal with Roboflo is to abstract the CP-SAT problem construction step to the level of the experimentalist. Problems are defined as experimental ”tasks” and hardware ”workers” without concern for the specific equations of the constraints. These abstractions are constructed with specific attention towards automation platforms where a physical sample is moved between ”workers” (eg fabrication and characterization stations) by another ”worker” (eg a robotic arm) over the course of an experiment. The final output is effectively a Gannt chart of times at which each task should be initiated and completed (Figure 7.2), given in machine-readable formats amenable to an automation pipeline.

7.3 Algorithm

7.3.1 First-class components

To construct the job scheduling problem, we must first define the tasks to be executed and the robotic components that will execute said tasks. In Roboflo, these are defined through four classes: we define Protocol’s as a sequence of Task’s to be completed, and define a System of individual Worker’s that can execute the Protocol’s. We must also define a set of Transition’s – Task’s that function to move a sample from one Worker to another. Given these pieces, Roboflo will construct and solve a constraint-programming problem to find a schedule to execute the Protocol’s.

Roboflo assumes that: - each Task occurs with one Worker. While multiple Worker’s can be required to complete a Task, the sample must reside with a given Worker for the duration of the Task. - Task’s do not interact with one another. A given Worker can be defined to handle more than one Task at a time (ie a hotplate can heat multiple Protocols at once), but multiple Protocols will note collapse at any point (ie five Protocols to weigh powders cannot merge into a

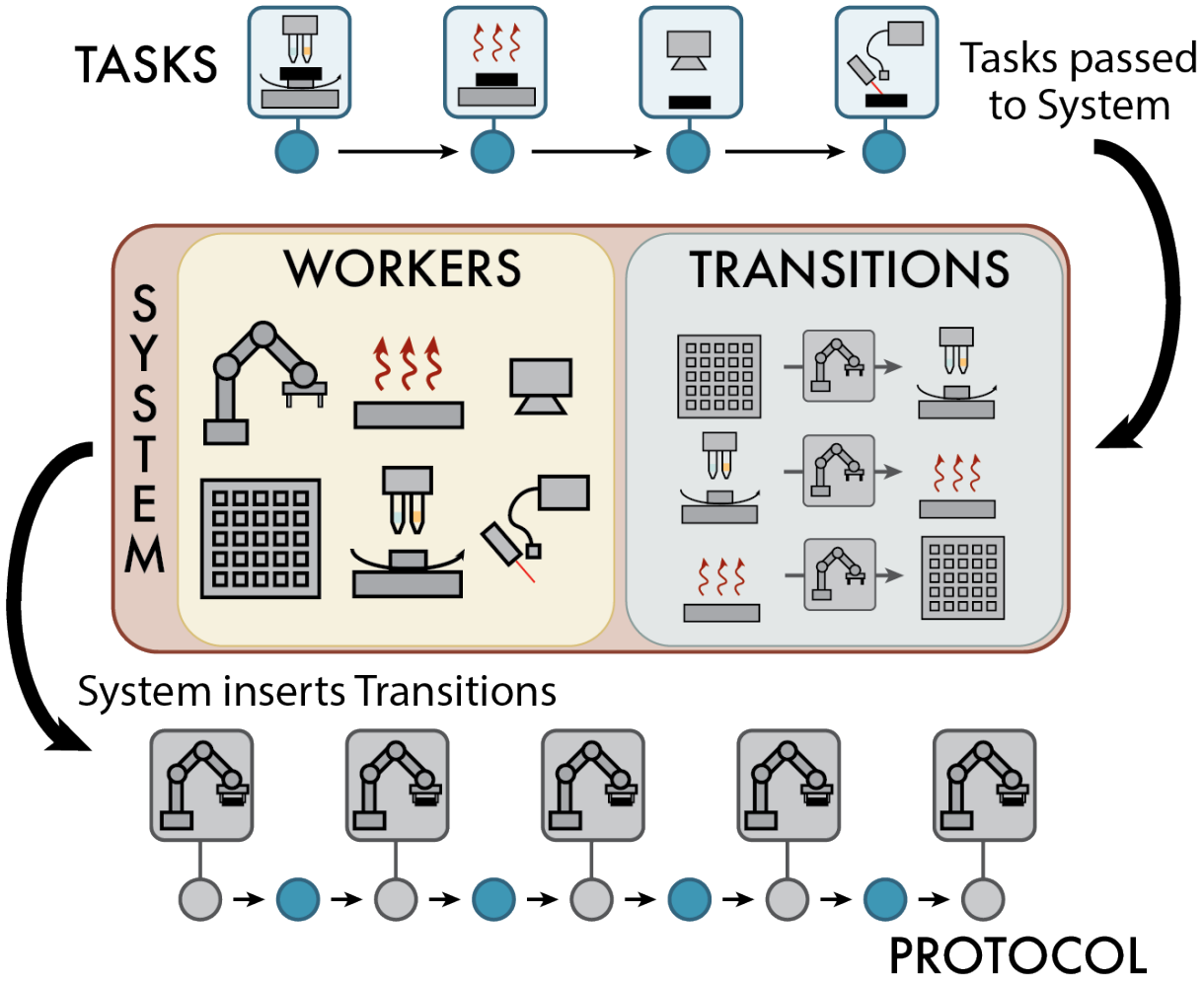

Figure 7.1. This figure demonstrates the components required to generate a single Protocol. A sequence of Tasks is passed to the System, which consists of Workers and Transitions. The System inserts any necessary Transitions to move samples between Workers for the Task sequence, returning a Protocol that contains all machine instructions to execute the Task sequence.

single heating step).

The System

The System class is defined by a set of Workers and Transitions. For each individual piece of hardware in the AE platform, we must instantiate a Worker, specifying a unique name and work capacity (number of Task's the Worker can complete simultaneously). In addition to Worker's, we define Transition's, which are Task's that move samples between a "source"

Worker and a ”destination” Worker. Together, the set of Transitions encode a finite state machine describing the allowed paths a Protocol can take between Worker’s in the System. [178]

The Protocol

Each experiment executed on the AE platform is considered a Protocol. In Roboflo, we assume that a physical sample will proceed from Worker to Worker over the course of a Protocol, completing one or more Task’s at each Worker. A Protocol is defined by a series of Task objects. Each Task is defined by a name, a set of Worker(s) required to execute the Task, and an expected duration to complete the Task. Additional properties determine how to schedule this Task with respect to other Task’s, both within the Protocol and across all Protocol’s. A Task can be specified to be ”immediate”, which requires that it executes as soon as the preceding Task within the Protocol is complete (for instance, moving a sample out of an oven to ensure the heating time is controlled). Additionally, a Task can be specified as a ”breakpoint”, meaning that it should be prioritized over later Task’s in all Protocol’s assigned to the System.

Once a worklist of Task’s are defined (ie the experimental procedure is codified into a sequence of Task objects), we pass this sequence into the System to generate a complete Protocol. Critically, this step inserts Transition’s wherever required in the worklist to move the sample to the appropriate Worker for each Task. In this way, the user need only to define Task’s of interest to the experimentalist (weigh this, heat this, etc), leaving the operational steps of the Protocol (move from the weigh station to the hotplate, etc.) for Roboflo to figure out. The user also defines the earliest start time of the Protocol, which defaults to zero to allow the constraint programming solver maximum freedom to optimize the schedule; in the case of a Protocol being added to an experiment in progress, this parameter can be used to ensure that the Task’s in this Protocol execute at future times.

7.3.2 Constraints Considered when Solving the Schedule

After the System is defined and all desired Protocol's created, we are left with a set of Task's that must be scheduled according to the constraints defined during Task creation, and to the constraints imposed by the capacity of each Worker in the System. We use constraint programming to determine the start time for each Task. The ending time is implicit, as each Task has a user-defined duration. Here, we outline how each constraint is represented mathematically for the constraint programming solver.

Task's within a Protocol must occur in order

For each Task, the start time must be greater or equal to than the ending time of the preceding task. If a Task is specified to be "immediate", then its start time must be equal to the ending time of the preceding Task. The start time of the initial task is set to be greater than or equal to the user-defined earliest start time for the Protocol.

Worker's must have enough capacity to complete each Task

For each Task, we have variables for the start and end times. From these we create an "interval" variable, and collect the total set of "intervals" for each Worker. For Worker's with a capacity of one, we enforce that none of these "intervals" overlap (ie only one Task can happen on that Worker at a time). For Worker's with a capacity greater than one, we treat each interval to have a weight of one, and enforce that the cumulative load on each Worker does not exceed the Worker's capacity.

Only one sample can reside on a unit-capacity Worker at a time

For Worker's with a capacity of one, we construct additional "intervals" between sequential Transition tasks to and from the Worker in each Protocol. Without this constraint, Protocol's with two or more Task's occuring on a unit-capacity Worker in a row may collide if the constraint solver opts to interweave the Task's from each Protocol. In principle, better constraint

structures exist to cover this scenario. We initially employed a ”reservoir” constraint structure that increments Worker capacity when a sample arrives (marked by the end time of an incoming Transition) and decrements when a sample leaves (end time of an outgoing Transition). While the reservoir constraint better reflects the physical constraints of the AE platform, it presented much greater computational complexity that rendered Roboflo unusable for even moderate quantities (¿100) of Task's. Our compromising solution prevents the failure mode of colliding Protocol's while still allowing schedules to be solved for large quantities of Task's in acceptable time.

Maintaining Protocol Order

Often we do not care about the order in which each Protocol is executed, and each Protocol should be defined assuming no interactions with another. Should the user opt to preserve Protocol order (eg to preserve a randomized order that minimizes systematic errors from the time of Protocol execution), we add a simple constraint that the starting time of the initial Task of each Protocol must be greater than that in the preceding Protocol.

Breakpoints and Inserting Protocols During Runtime

Once a the start times have been solved for a set of Task's, additional Task's can be added into the System and solved around the existing schedule. This comes in to play in two scenarios: solving schedules with ”breakpoints”, and adding new Protocol's into an existing set of Protocols.

”Breakpoints” indicate Task's which should be given higher scheduling priority than others. Within a Protocol, multiple Task's can be designated as ”breakpoints”, with priority given to the earlier breakpoints. When solving a schedule for a set of Protocol's containing breakpoints, Roboflo will initially construct a schedule only with Tasks's up to the first breakpoint in each Protocol. Note that any immediate Task's following the breakpoint Task will also be included in this step. Once the start times for these Task's have been solved, all Task's up to the second breakpoint will be included, and the schedule will be solved. This process repeats until start

times for all Task's are solved. Previously solved start times are set as constants in each iteration of this process, such that new Task's are solved around the existing schedule.

A Protocol added to an existing schedule is solved in the same fashion as a Protocol with breakpoints. The Task's from the new Protocol are added the total Task set in the existing schedule, and the start times for the new Protocol's are solved around the existing schedule. Roboflo provides an option to "flex solve" upon adding a new Protocol, in which case the start times of all Task's currently starting after the start time of the new Protocol are no longer treated as constants. In practice, we have not seen a significant reduction in the total runtime of schedules by "flex solving", though there may be scenarios where this approach is desirable.

7.4 Results and Discussion

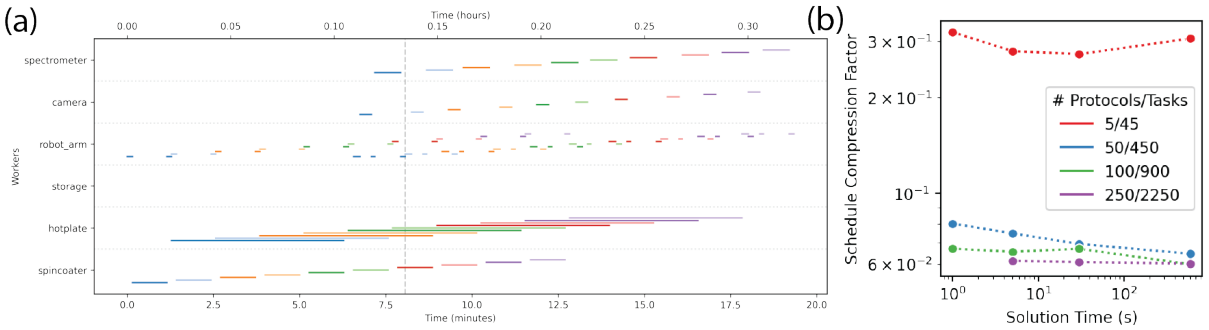

Figure 7.2. (a) Schedule for ten identical protocols on a mock automated experimentation platform with a robot arm to move samples between a storage tray, spincoater, hotplate, and two characterization stations. Each horizontal line represents the duration of a Task, and each color represents a Protocol. The Task's are plotted in rows based on which Worker is considered "home" during execution of the Task. The vertical dashed line indicates the time at which the first protocol is completed. (b) Schedule compression factor solving time and schedule size. The missing point represents a condition for which a valid schedule was not found.

7.5 Integrating Roboflo into an Automated Experimentation Platform

As an example, we imagine an AE platform for the fabrication and measurement of thin films by spin-coating (Figure 7.1). This platform has six Workers (ie stations): a spincoater, a hotplate, a camera, a spectrometer, a robotic arm to move samples between Workers, and a storage Worker to hold samples before and after the Protocol. Following Section 7.3.1, a Roboflo System is constructed for this platform by defining Workers for each piece of hardware, and Transitions to move between the hardware. Once the System is defined, Protocol's are constructed by the System from lists of Task's. In this example, a Protocol begins with spincoating a thin film, follows with annealing of the thin film, and ends with measurements at the camera and at the spectrometer. Accordingly, the user inputs four Tasks to the System (blue dots in Figure 7.1). Each Task has a Worker as the "location" at which it occurs. Based on these locations, the System inserts Transitions between Tasks as necessary to move the sample between "locations" (gray dots in Figure 7.1) – an essential step for automation that is irrelevant to the experimentalist. The total set of Tasks and Transitions constitute one Protocol. Once a set of Protocols have been constructed, we tell Roboflo to solve the schedule, which can then be exported as a JSON file and passed to the AE platform. [179]

7.5.1 Typical Schedule Solve Time

Solving times of 30 seconds or less are sufficient to approach the optimal schedule for typical experiments. We demonstrate this with our mock spin-coating AE platform. Figure 7.2(a) shows an example schedule for ten identical protocols following the steps described earlier and shown in Figure 7.1. Each horizontal line represents the duration of a Task, and each color represents a Protocol. The Task's are plotted in the row of the Worker considered "home" during execution of the Task. The vertical dashed line indicates the time at which the first protocol is completed (˜8 minutes).

We evaluate the quality of a schedule by the ”compression factor”. The compression factor is the duration of the schedule divided by the duration of a schedule in which all protocols are run serially. For example, the schedule shown in Figure 7.2(a) has a compression factor of about 0.25. Schedule compression factor is shown as a function of the time spent searching for a solution (from 1 to 600 seconds) and the size of the scheduling problem (from 45 to 2250 Tasks) in Figure 7.2(b). A valid schedule was found for all trials except the largest problem at the shortest search time. Once a schedule was found, however, additional solution time shows diminishing returns in the compression factor. Larger schedules allowed for greater compression factors, likely due to the greater degrees of freedom afforded with additional Tasks. The specific values here are highly dependent on the Protocol's and System of interest. Bottlenecks in the System will raise the lower bound of the compression factor, though this simply reflects the physical constraints of the System. Our results do, however, provide useful heuristics for use of a Roboflo: tens of seconds of solution time should be plenty to find a valid schedule.

Note that all tests were performed on a consumer-grade laptop (M1 Macbook Air, 2020). For large numbers of Tasks (over $10\hat{3}$), our CP-SAT solver required exponentially more time than specificed to find a valid schedule. Code profiling exposed that our solver was memory-limited, suggesting that improved hardware may be required to solve larger problems. Thorough benchmarking of our backend CP-SAT solver suggest that, with the proper hardware, performance can scale sufficiently across a range of standard operations research benchmarks. [175]

7.5.2 Improved Throughput

The primary value proposition of Roboflo is to compress the total time required to run a set of experiments on valuable automation hardware. Proper scheduling can provide a significant increase in throughput with no additional hardware cost. We demonstrate this by a schedule solved for an experiment consisting of ten identical Protocols on our simulated AE platform (Figure 7.2b). The resulting schedule requires a total of 25 minutes to execute, whereas the same experiment with protocols run in series would have taken 94 minutes. Even in this simple case,

we see that proper job scheduling yields nearly a 4x improvement to throughput. The exact degree of improvement will depend heavily on the nature of Tasks and degree of parallelization possible for a given AE platfom.

7.5.3 Online Scheduling

In the previous example, we showed how ”offline” job scheduling can be used prior to beginning an experiment. Roboflo additionally allows for ”online” scheduling, where Protocols are inserted into an existing schedule. This is a key feature enabling closed-loop automated experimentation, wherein new protocols are introduced mid-experiment by an AI agent based on the results of previous protocols. [169] Online scheduling also allows multiple users to leverage the same system simultaneously, as will be the case for advanced AE platforms at shared user facilities. To insert a protocol to an existing schedule, we must only provide a minimum start time for the new Protocol, after which point we solve the schedule as before. Under the hood, this amounts to changing the minimum bound of the start time of the initial Task in the new Protocol. In practice, this start time should be set slightly in the future from the current time of the experiment to allow time to both solve the schedule and to integrate the results into the AE platform’s task queues. Conveniently, the computational overhead of solving a schedule with a few new Protocol’s is lower than solving a schedule from scratch. This arises from the fewer degrees of freedom typical of these scenarios, where the majority of Tasks being scheduled already have their start times fixed from a previous solution, and only the start times of Tasks from the new Protocol(s) must be solved for.

7.5.4 Flexibility for New Hardware and Tasks

The abstractions present in Roboflo map one-to-one with physical hardware and tasks of the AE platform. If a new piece of hardware is incorporated into the platform, one must simply add a new Worker and corresponding Transitions to the Roboflo System. New Tasks are similarly easy to incorporate, and in fact arbitrary Tasks can be scheduled into any Protocol given that

they only use Workers present in the System. Codebases for homebuilt hardware tend to be highly specific and fragile, and the high turnover in academic labs leads to upgrades and tweaks being made by tool maintainers who may not have had a hand in the design of the AE platform. While this point will not make headlines, we hope that Roboflo facilitates both rapid prototyping, flexibility, and maintainability for AE platforms.

7.6 Acknowledgements

Chapter 7, in part, is currently being prepared for submission as "Roboflo: A Job Scheduler for Automated Experimentation Platforms" by Kumar, R. E. and Fenning, D. P. The dissertation author is the primary investigator and author of this material.

Chapter 8

MixSol: Planning Volume Transfers to Reach Arbitrary Mixtures From Stock Solutions with Pipette Constraints and Minimal Waste

8.1 Motivation

A common research goal is to evaluate how a system behaves given different ratios and amounts of its constituent components. In these scenarios combinatorial experiments are often employed to survey material behavior, such as the efficacy of treatment molecules in drug discovery [180, 181, 182], the optical signature of colloidal nanoparticles [183, 184, 185], and the crystal structure and capacity of battery electrodes [186, 187, 188]. Solution-based approaches simplify the execution of such combinatorial studies, in that two solutions can simply be mixed at controlled ratios to form intermediate solutions of interest. While the calculation of the volumes required of the starting solutions to form a target intermediate solution is quite simple, the complexity of such calculations grows with the number of starting and intermediate solutions. Furthermore, the physical constraints of the hardware used to perform the volume transfers (minimum pipetting volume, pipette precision, etc.) impose limits on mixing paths, making some mixtures impossible without either generating intermediate dilutions or excess volume of the target solution. We provide a mathematical framework and software tool to

devise a sequence of volume transfers to reach from a set of starting solutions a set of target solutions with target volumes. Our tool, MixSol, takes into account the minimum volume transfer allowed per step to ensure that transfers are within the reliable range of the user's pipetting hardware. When a target cannot be achieved from the starting set while respecting this minimum transfer volume, MixSol will attempt to use other achieved targets as intermediates to reach the target mixture. Overall, MixSol enables programmatic generation of a sequence of volume transfers to reach arbitrary mixtures with no waste volume, automating a critical planning step in solution-based mixing experiments.

8.2 Algorithm

Planning the volume transfer sequence occurs over three major steps. First, we construct from the total set of starting and target solutions the *solution matrix*

$$\mathbf{S} = [s_1, ..., s_n]^t \in R^{n \times c}$$

where s is the number of solutions and c is the number of unique solutes and solvents comprising the set of solutions. Additionally, we define the *availability set* $\mathbf{A} \subset S$ as the set of solutions s_i that are available to be mixed into other targets. $\mathbf{A}$ initially consists of a set of solutions the user defines as "stock solutions", and grows as the algorithm proceeds. Second, the total set of volume transfers is computed and in the *transfer graph*

$$\mathbf{T} = [t_1, \ldots, t_n]^t \in R^{n \times n}$$

where $\mathbf{T}$ is a directed acyclic graph for which $\mathbf{T}_{i,j}$ is the volume transfer from s_i to s_j. Each row t_i is computed by non-negative least squares factorization to solve for t_i in

$$St_i^T = s_i^T \mid \sum_{j \in \mathbf{A}} t_{i,j} = 0$$

If a valid t_i is found, s_i is added to $\mathbf{A}$. This process proceeds iteratively until either transfers are solved for all targets, or all unsolved targets are deemed unsolvable. Finally, in the event that all targets are solved, the graph hierarchy of T is computed by topological sorting [189] to determine the sequence of volume transfers. These steps are now described in more detail.

8.2.1 Constructing the Solution Matrix S

To construct the *solution matrix* $\mathbf{S}$, we must first represent the individual stock and target solutions as vectors s_i. The user first defines each solution by its solute(s) and solvent(s). Given the total set of stock and target solutions, we enumerate the set of unique solute and solvent components $\mathbf{C} \in R^c$. Each solution is represented as a vector s_i where element $s_{i,j}$ is: for solutes, the molarity of solute C_j in solution s_i, and for solvents, the solvent fraction of solvent C_j in solution s_i. This distinction is made because while for solutes the absolute amounts matter for mixture calculations, for solvents only the relative amounts matter; when one dilutes a solution with the same solvent, the molarities of the solutes decrease accordingly, whereas the solvent remains unchanged.

8.2.2 Constructing the Transfer Graph T

Given the matrix representation $\mathbf{S}$ of our solutions, the volumes t_i of solutions $\mathbf{S}$ that mix to yield a target solution s_i can be described as a solution to the linear system of equations $St_i^t = s_i^t$ with the additional constraint that all elements of t_i are non-negative (we cannot mix negative volumes). The general concept of using matrix math to solve for mixing fractions is well described by Schrier *et al.* [190] In our framework, we have two other constraints: only available solutions $s_i \in A$ can be used, and the smallest element of t_i must be greater than the minimum allowed volume transfer (set by the user based on the pipetting hardware). Initially, only the stock solutions are available. We iteratively attempt to solve for volume transfers

$$t_i \forall s_i \notin A \text{ by } St_i^T = s_i^T \mid \sum_{j \in \mathbf{A}} t_{i,j} = 0$$

using non-negative least squares (NNLS). At this point, some targets may be impossible to reach. After each iteration, however, more solutions become available, ideally providing a path to previously unreachable targets. If the size of the available set **A** does not increase after an iteration, then the algorithm has reached a dead end and cannot find a solution, at which point the user must adjust their target volumes, target solutions, or stock solutions to allow for a valid mixing strategy. In the event that transfers t_i are solved for all target solutions, the resulting matrix T constitutes a valid directed acyclic graph where each element $t_{i,j}$ is the volume of liquid to transfer from s_i to s_j to yield all target solutions in **S**.

We note an additional step in the code implementation that improves accuracy when mixing a solution with trace components. Prior to solving for t_i by NNLS, the solution matrix **S** is temporarily normalized such that the smallest value is equal to one. This is to avoid rounding issues in the NNLS solver, which we found to be common when some elements of **S** were very small ($< 1 \times 10^{-4}$). Each solution from NNLS is corrected to undo the effect of this normalization before proceeding.

8.2.3 Determining the Sequence of Volume Transfers

The *transfer graph* **T** is missing two critical components for generating a usable of volume transfers. First, the sequence of volume transfers must be determined, as transfers for some targets require that other targets have already been prepared. This sequence is implicit in the structure of the graph, and the transfer "generations" are recovered by topological sorting via Kahn's algorithm. [191, 189] Second, the transfer volumes were computed to yield exactly the final volume desired of each target, which does not take into consideration any excess volume required of targets to be transferred to other targets in later "generations". Once the sequence of transfers is recovered, we backgprogagate volume requirements from the last transfer generation up to the initial generation to determine the maximum volume of each stock and target required to end with the target volumes.

The sequence of volume transfers is recovered using Kahn's algorithm. [191] At a high

level, the algorithm analyzes the number of incoming edges (ie incoming volume) into each node (ie solution) of **T** to find "generations" of nodes such that nodes of the first generation do not have any incoming edges, and nodes of subsequent generations have incoming edges only from nodes of earlier generations. Topological sorting requires that the graph **T** is acyclic, meaning that there must be at least one node with no incoming edges. This is guaranteed in our scenario, as our process begins with stock solutions whose nodes in **T** will not have incoming edges. Stock solutions do not require any incoming volume transfers, and in practice our first generation will always be the set of stock solutions. Within each generation, the sequence in which transfers are made has no impact on the resulting mixtures.

Given the generational sequence of volume transfers, we can now determine the maximum volume required of each target solutions such that, after the final generation of mixing has completed, we retain the target volume of each target solution. This maximum volume is also the initial volume we must produce of each solution – after the solution is mixed within its generation, its volume will only be reduced to form dependent solutions in future generations. We begin by row-normalizing the transfer graph T such that the total incoming flow to each node (solution) sums to one, which we call T^{norm}. We also define the *initial volumes*

$$v^{initial} = v^{target} \in R^s, \text{ where} v_i^{initial}$$

is the initial volume to be prepared of solution s_i. The *target volumes* v^{target} is an analogous vector with the final volumes desired of each solution. We traverse the mixing hierarchy from last to first generation. Within each generation, for each solution s_i we increment $v^{initial}$ by the incoming volumes for s_i, calculated as $v_i^{initial}\ T_i^{norm}$. After the hierarchy traversal is complete, the transfer volumes required to form s_i are computed by $v_i^{initial} T_i^{norm}$.

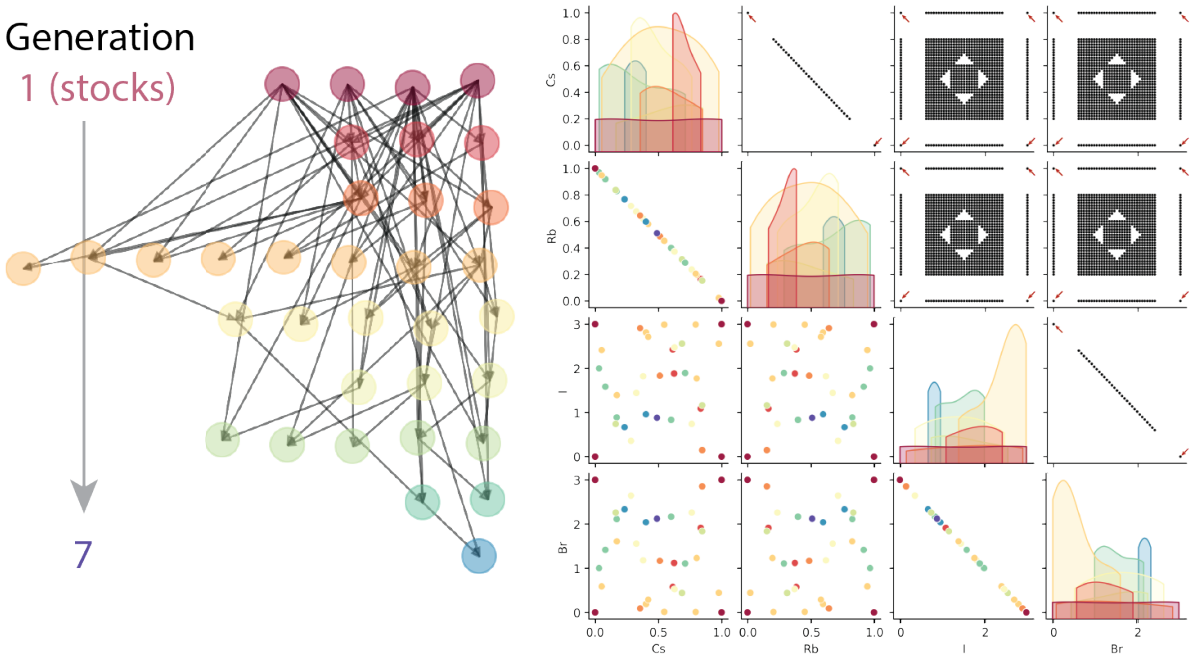

Figure 8.1. *Covering a Component Space with MixSol*: This figure highlights MixSol's capabilities in both offline and online settings. The upper right set of plots in (b) shows all points in component space that can be reached in a single mixture of the four stock solutions (marked with red arrows) under the constraints of a minimum pipetting volume of 20% of the target volume and a precision of 1% of the target volume. The bottom left set of plots in (b) shows a set of targets that can be reached from the same four stocks with zero waste solution. The color represents the mixing generation at which each target can be reached.Along the diagonal are distributions over each component dimension that are accessed per generation. (a) shows a the directed graph of volume transfers, ordered from top to bottom by mixing generation and colored to match the points shown in (b)

8.3 Using MixSol in Experiments

MixSol enables automation of the mixture planning process in both online and offline experimentation paradigms. The majority of research happens in an offline setting, in which the experimental design, execution, and analysis steps occur independently of one another. A researcher who plans their experiment at their desk, runs the experiment in the lab, then analyzes the data back at their desk is operating in an offline paradigm. In an online setting, analysis results are parsed to automatically design and propose further experiments, closing the loop between these steps. A robotic platform that continuously executes experiments, processes data,

and plans new experiments via Bayesian Optimization is operating in an online paradigm. In the offline setting, MixSol saves time and improves material efficiency. In the online setting, MixSol is a necessary component to ensure smooth, unattended operation.

8.3.1 MixSol in an Offline Setting

In an offline setting, a user will define a set of stock solutions and target solutions they would like to achieve. Solutions are each defined by the user in terms of solute molarities, solvent fractions. For each target solution, the user additionally provides a desired target volumes. Then, given a minimum volume transfer and threshold mixture accuracy, MixSol will attempt to compute a sequence of volume transfers to yield the target solutions. The threshold mixture accuracy is computed in terms of percent error of any single component (solute or solvent fraction) – for example, with an accuracy of 0.001, all components must be within 0.1% of the target value to consider a mixture successful. If successful, the results can be retrieved in a variety of ways: a set of text instructions, a visual graph of volume transfers (Figure 8.1a), or a set of machine-ready instructions in the JavaScript Object Notation (JSON) format. [179] The text instructions and visual graph are intended for the human user, where the graph gives a high-level overview of the mixing strategy and the text instructions can be printed and brought into the lab for execution. A large segment of offline solution-based experiments leverage liquid handlers to precisely execute a series of mixtures. The JSON format is chosen to facilitate simple integration of MixSol into automation software, and can easily be restructured into the format required for a given tool (for example, Comma-Separated Value (CSV) files are common inputs for liquid handlers).

In some scenarios, MixSol will be unable to find a set of volume transfers that satisfy the constraints imposed by the pipetting and desired volumes. A simple visual of this issue is given in the upper corner of Figure 8.1b, which shows the regions of component spaces accessible from a set of four stock solutions. Regions near the stocks themselves are not accessible, as the minimum pipetting volume (in this case, 20 microliters) prevents such small fractions of the

stock from contributing target volume (100 microliters). An user can address these issues in three ways. First, the target volume of the target solution in question can be increased, such that the minimum pipetting volume is a smaller fraction of the total volume; this enables one to reach points closer in component space to the stock itsef. Second, an intermediate target solution can be introduced to act as a stepping stone between the available stocks and inaccessible regions of component space. Finally, the set of stock solutions can be adjusted to make desired regions of component space more accessible. These steps are currently left to the user to apply, though MixSol does identify exactly which targets are inaccessible to facilitate informed adjustment by the user. Future work may focus on suggestion or even automation of minimum adjustments required to make an infeasible set of stocks and targets feasible.

8.3.2 MixSol in an Online Setting

In an online setting, a user will have define a search space from which the automated experimentation platform can select points to evaluate. For solution-based mixing online experiments, some of these search dimensions will involve components (solutes or solvents) contained within the stock solutions. From a purely mathematical standpoint, the stock solutions form a convex hull in component space, and any target solution within this hull can be accessed via mixing. In practice, however, the accuracy, minimum pipetting volume, and desired volume of each target solution together place limits on the regions within the convex hull that can be experimentally accessed. Given a set of stock solutions and the aforementioned constraints, MixSol can enumerate the total set of accessible targets (upper half of Figure 8.1b). The automated platform can then select from this set without any risk of selecting points that may lie within the convex hull of the stock solutions but are not experimentally accessible. The rest of the MixSol workflow remains the same as in the offline setting.

8.3.3 MixSol for Weighing Solid Reagents to Form Solutions

A subset of MixSol's algorithm for volume transfer planning is equivalent to the algorithm required to compute masses of solid reagents required to form a target solution of a target volume. We treat the reagents as stock "solutions" with solute components at molarities set to the molar mass of the reagents. Then as before we use NNLS to compute the masses (instead of volumes) of each reagent to be mixed to form the desired solution of a user-defined target volume. This is a convenient feature to aid in the preparation of stock solutions for both offline and online experiments.

8.4 Conclusion

Solution-based studies present a convenient and simple way to explore a continuum of solutions, as a few starting solutions can be mixed to achieve desired target solutions. MixSol automates the calculation of volume transfers that generate these target solutions from the starting solutions. The automation of this step makes new types of experiments practical, whether operating in offline and online formats. In offline operation, MixSol can provide significant time savings in experimental planning for researchers who want to test mixtures with irregular spacing across a component space. Additionally, MixSol deterimines sequences of volume transfers that require no volume overhead, reducing waste and preserving potentially expensive reagents. In online operation, the automation of this planning step has obvious value – an automated experimentation platform has to determine all aspects of the experiment on the fly. Furthermore, MixSol can enumerate the total set of targets that can be accessed from the starting solutions while respecting the constraints of the pipetting hardware, ensuring that only possible experiments are allowed in the design space. MixSol consolidates established mathematical approaches for mixture calculation into a usable package tailor-made for solution-based experimental design, providing a critical component of high-throughput, solution-based experimentation platforms.

8.5 Acknowledgments

Chapter 8, in part, is currently being prepared for submission as ”MixSol: Planning Volume Transfers to Reach Arbitrary Mixtures From Stock Solutions with Pipette Constraints and Minimal Waste” by Kumar, R. E. and Fenning, D. P. The dissertation author is the primary investigator and author of this material.

Chapter 9

Robotic High-Throughput Screening Identifies Durable Halide Perovskite Absorbers for Tandem Photovoltaics

While significant and rapid development has been made in single junction perovskite devices, the most direct path to commercial deployment is as a top cell in perovskite silicon tandems [192]. Tandem photovoltaics present an attractive route due to their high theoretical power conversion efficiencies (PCE) which can result in overall lower balance of system costs [193, 194]. Perovskite absorbers are uniquely positioned to serve as tandem partners in photovoltaic given their relatively low production costs, tunable bandgaps, and sharp optical absorption edges [195, 196, 93]. However, the implementation of wide bandgap perovskites suitable for perovskite-silicon tandems ($Eg > 1.6eV$)[197, 198] has proved challenging; these absorbers typically suffer from phase segregation, especially under illumination, leading to large open-circuit voltage (V_{OC}) deficits and rapid degradation of device performance [199]. Adjustments to the intrinsic properties of perovskite absorbers (carrier mobility/lifetime, bandgap, thermal/structural stability, etc..) can be achieved through mixed perovskite absorbers [100]. For single junction application, the so-called ”kitchen-sink” or ”triple cation” family of compositions has dominated the best-performing and most-stable reports. There remain large, unexplored regions in the halide perovskite composition space with several potentially viable candidates among $FAPbI_3$-based perovskites.

With PASCAL, we fabricate and measure samples at a rate of up to 10^3 samples/day. As a proof of concept, we fabricate and test films of 83 unique compositions in the $MA_xFA_{0.78}Cs_{0.22-x}Pb(I_{0.8-y-z}Br_yCl_z)_3$ space in under 48 cumulative hours, evaluating the films on bandgap, photoluminescence, and stability against intense illumination and thermal stress to establish the tradeoffs made between these properties across the space. From these results we divide the compositional space into four regions of durability behavior, and within each region identify Pareto-optimal compositions which promise the highest potential open circuit voltages with bandgaps closest to the 1.67 eV target for perovskite-on-silicon tandems. In summary, we offer a list of promising absorber compositions for development of top cells on silicon bottom cells, demonstrating the power of robotic screening for design of halide perovskites.

9.1 Motivation

9.2 Experimental Methods

9.2.1 Preparation of Absorber Stock Solutions

Eight ”endpoint” stock solutions were prepared to reach a nominal composition of $MA_xFA_{0.78}Cs_{0.22-x}Pb(I_{0.8-y-z}Br_yCl_z)_3$, where, for (x,y,z), the solutions were (0,0.1,0), (0, 0.2, 0), (0,0,0.1), (0,0.1,0.1), (0.1,0.1,0), (0.1, 0.2, 0), (0.1,0,0.1), and (0.1,0.1,0.1). All solutions were prepared at 1.2 M in a 3:1 volume ratio of DMF:DMSO using MAI (GreatCell), FAI (GreatCell), CsI (Sigma, 99.999%), PbI_2 (Sigma, 99.999%), $PbBr_2$ (Sigma, 99.999%), and $PbCl_2$ (Sigma, 99.999%). PbI_2 was added in 9% excess to the nominal amount. Solutions were vortexed until no solids were visible (15-20 minutes), heated to 85°Cfor 10 minutes, allowed to cool down to room temperature, then filtered through a 0.20 micron filter. Finally, these eight ”endpoint” solutions were mixed in a polycarbonate 96-well plate by an Opentrons OT2 liquid handler to achieve the target compositions for the screening experiments. All steps were performed within a nitrogen-filled glovebox.

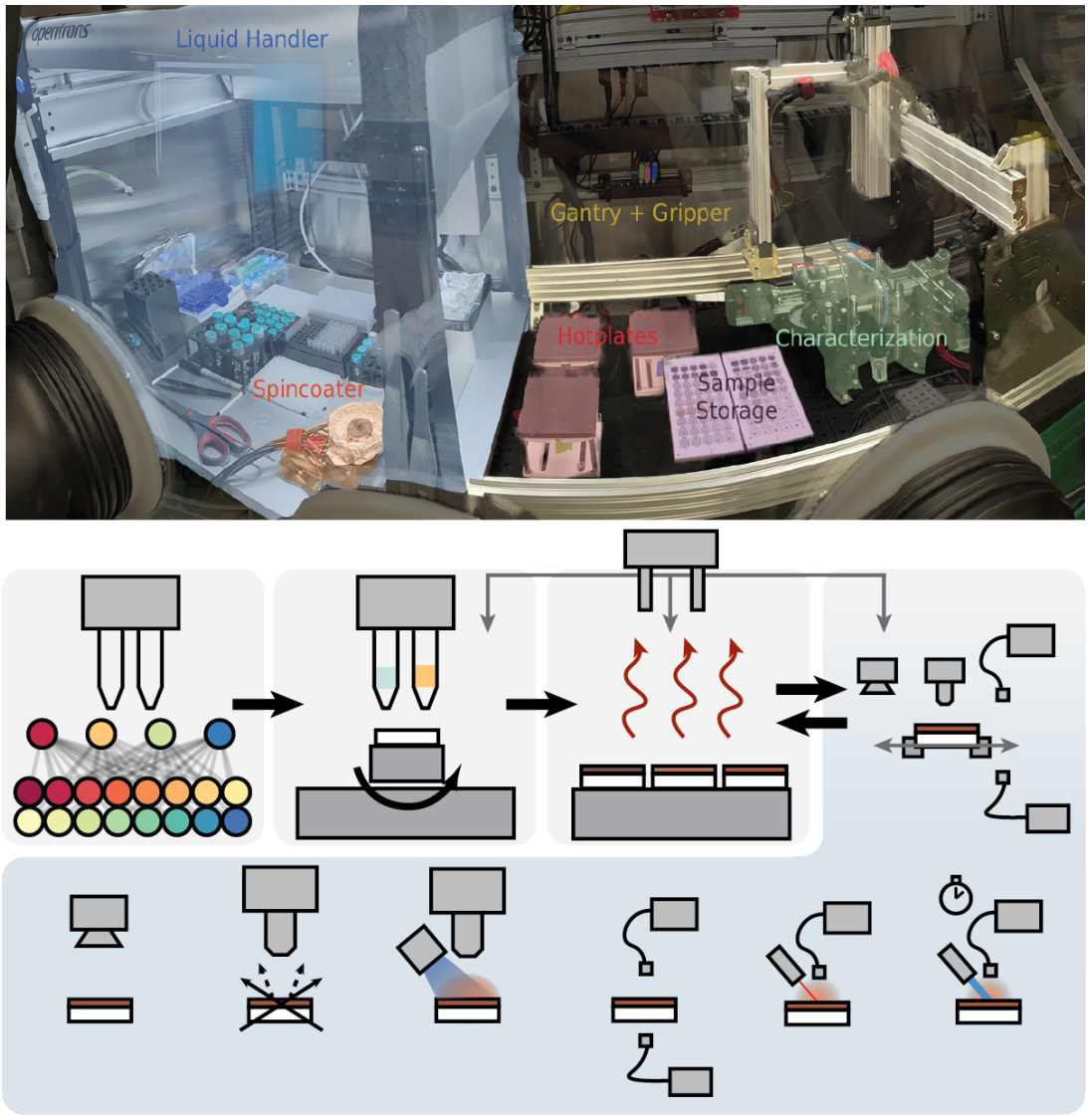

Figure 9.1. (a) False-colored image of the Perovskite Automated Solar Cell Assembly Line (PASCAL) with the various hardware stations labeled. (b) Workflow for a typical experiment.Schematics are shown for the characterization techniques present on the characterization line.)

9.2.2 Film Fabrication

1x1 cm glass slides were cleaned via sequential sonication steps each with a duration of 15 minutes in the following order: 5 v/v % Hellmanax (Sigma) in DI water, DI water, acetone, ethanol, and isopropyl alcohol. After drying with a filtered compressed dry air gun, the samples were treated by UV-ozone for 20 minutes under an oxygen flow of 5 scfm. Upon completion, the

substrates were immediately moved into the glovebox containing the robotic platform for film deposition.

Films were fabricated by spincoating on the robotic platform. Specifically, 20 microliters of absorber solution were dispensed statically, followed by spinning at 3000 rpm for 50 seconds. 80 microliters of methyl acetate was dispensed from 2 mm above the spinning substrate at a rate of 100 microliters/second with 22 seconds remaining in the 3000 rpm spin step. After the spin completes, the sample is immediately moved to a hotplate and annealed at 100°Cfor 30 minutes, and is finally moved to an aluminum-floored sample storage tray to cool to room temperature.

9.2.3 Characterization

All characterization is performed at least 3 minutes after the glass slide has moved onto the aluminum cooling tray. Once cooled, the sample is transferred to a linear stage, which carries the sample through a series of stations.

Photoluminescence

Photoluminescence spectra are acquired using a 0.9 watt 632 nm laser as an excitation source. Spectra are fit by single gaussians (cts vs eV) to extract PL intensity, center emission energy, and full-width half-max.

Transmittance

Transmission spectroscopy is used to estimate the optical bandgap using Tauc analysis [200, 201] assuming a direct bandgap material.

Photostability

Series of photoluminescence spectra are acquired at two second intervals using a focused 0.9 watt 450 nm laser as an excitation source. The focused power is equivalent to about four suns intensity. Individual spectra are fit by single gaussians (cts vs eV) to extract PL intensity,

center emission energy, and full-width half-max, and these extracted parameters are compared over time to evaluate film stability.

Thermal Stability

A subset of the films are measured by transmittance and photoluminescence spectroscopy at 1.5 hour intervals over the course of heating at 85°Con a hotplate in a nitrogen glovebox. Films are moved to the aluminum storage tray for at least 5 minutes before each measurement to cool to room temperature, measured, and then returned to the hot plate. While many samples are tracked for over 16 hours, some were dropped as early as the 6 hour measurement by the robot gripper in the course of the experiment. We therefore draw comparisons using only the first 4.5 hours shared by all tested samples.

9.3 Results and Discussion

9.3.1 PASCAL Workflow

PASCAL consists of five primary components: a liquid handler (Opentrons OT2) to mix and spincoat solutions, an array of three hotplates to anneal samples and perform thermal degradation tests, a characterization train to measure optical spectra and take images of each sample, storage trays to hold substrates and completed samples, and a carterian gantry with a parallel gripper to move samples between stations (Figure 9.1a). The spincoater was custom built to fit in one of the liquid handler deck slots such that the liquid handler can pipette directly onto it. All components are housed inside a nitrogen glovebox to enable work on halide perovskites, which are sensitive to both oxygen and humidity exposure. The overall system is controlled from one computer using a custom Python library. This library is publically available, but is heavily tailored to PASCAL; some of the generally useful components, specifically those for planning of mixtures between stock solutions and targets and for job scheduling for parallel job execution, are available as standalone Python packages (MixSol and Roboflo as discussed earlier..

A typical compositional screening experiment begins with the interpolation of stock

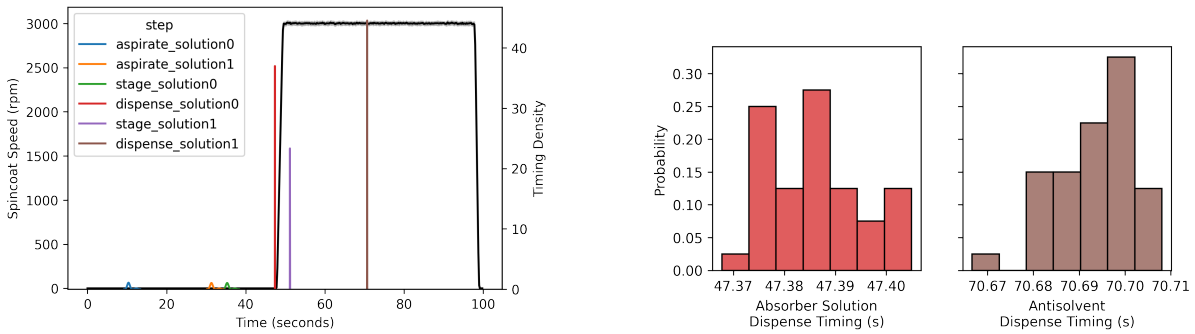

Figure 9.2. (a) Representative distribution of spincoating timings over 45 samples. The black line represents the average recorded spincoating speed (rpm) vs time, with shading representing the standard deviation in rpm. The kernel density plots represent timing distributions for the steps performed by the liquid handler during spincoating, where each individual distribution is normalized such that the area under the curve is equal to one. (b) histograms corresponding to the timings of the solution dispense times in (a).

solutions into target solutions (Figure 9.1b). All compositions in our study were reached by mixing eight ”endpoint” solutions that bound the compositional space, mixed in a 96-well plate by the liquid handler. Next, a glass substrate is transferred to the spincoater chuck by the robot arm. The spincoater chuck incorporates an indexed encoder such that it can be rotated to a known position, which is necessary for the parallel gripper to pick up the square sample substrates. During spincoating, PASCAL affords greater precision and recording of this critical step than is possible with human operation. The dispense height and rate are precisely controlled, and the dispense timing is repeatable to within 30 milliseconds (Figure 9.2). After spincoating, the sample is transferred to one of three hotplates (depending on the set temperature), annealed, then transferred to the storage tray to cool to room temperature prior to characterization. PASCAL's characterization line consists of cameras, LED and laser excitation sources, a halogen lamp, and a spectrometer to allow for a variety of measurements to be made. Additionally, the characterization line has a linear stage to carry one sample between the various stations, allowing sample transfers between stations during characterization step (which can take many minutes) to be decoupled from transfers between the fabrication steps (which can occur every ten seconds or so when operating at maximum capacity). PASCAL works on many samples in parallel, with

typical experiments requiring about 4 hours for fabrication and characterization of 45 samples (example job schedule in Figure 9.3).

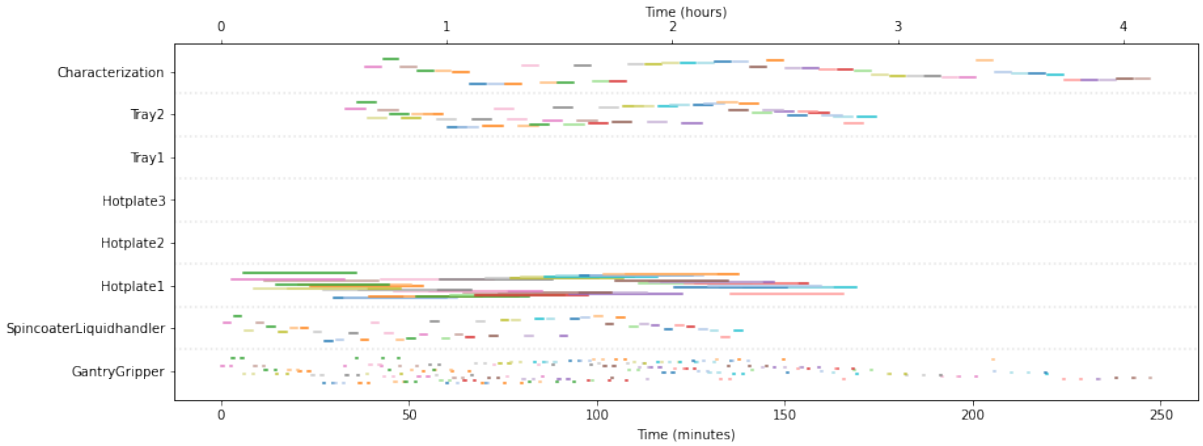

Figure 9.3. Typical job schedule for a compositional screening experiment of 45 samples. The rows correspond to the independent hardware workers in PASCAL. Colored lines indicate the duration of individual tasks on the, with each color representing a sample (note that colors repeat, as this colormap has only 20 unique colors).

The remainder of this work is a case study demonstrating the capability of PASCAL. We fabricate and test compositions over a compositional domain of interest for wide-bandgap solar absorbers, with the eventual goal of developing perovskite-on-silicon tandem cells. The data discussed were generated in two campaigns of 3-4 batches of 45 samples each. Each campaign covered the same compositional space but with different meshes, leading to irregular sampling of the total space. Nevertheless, these screening data allow us to evaluate absorber compositions on a variety of dimensions of merit prior to investing the additional effort of cell fabrication and optimization.

9.3.2 Photovoltaic Figures of Merit

Bandgap

The bandgap of thin films across our compositional space range from 1.55 to 1.72 eV (Figure 9.4a). The dominant trends in bandgap arise, expectedly, from variations in the halide composition at the X-site. [cite bandgap comes from B-X primarily] The bandgap widens with

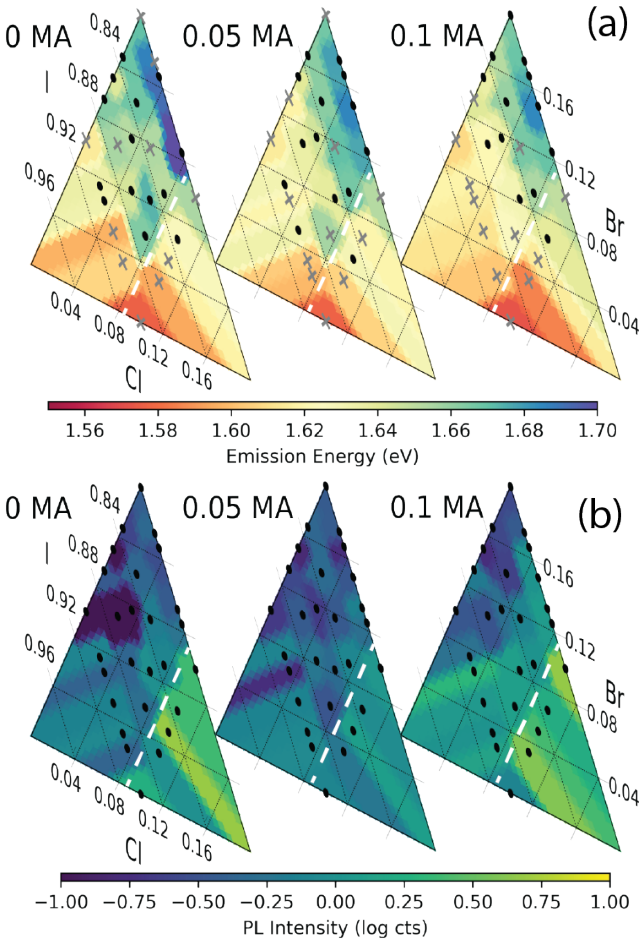

Figure 9.4. Photoluminescence (a) emission energy and (b) intensity for perovskite thin films across the tested compositional space. The dashed lines indicate a change in trend along the chlorine axis.

increasing bromine fraction (moving towards the top corner of the ternary diagrams). With increasing chlorine content (moving towards the bottom right corner), however, the bandgap initially widens until chlorine comprises 7% of the halide content, after which the bandgap redshifts (dashed lines in Figure 9.4a). This is consistent with previous literature reports probing the solubility of chlorine in similar composition spaces where, past a certain percentage, chlorine addition causes compositional segregation into lower and higher chlorine regions and a net redshift in bandgap.[202] Interestingly, we observe this redshift in all 10% Cl compositions except those with the highest bromine content (10% Br) regardless of A-site composition, suggesting that the solubility limit of chlorine in this system is increased by bromine addition. The composition of the A-site also affects the material bandgap. As we increase methyl ammonium content (and accordingly decrease cesium content), the bandgap narrows slightly.

Photoluminescence Intensity to Approximate Relative Open Circuit Voltage

The photoluminescence intensity of films across the compositional space is shown in Figure 9.4 b. Transmittance spectra show that absorbance at the excitation wavelength (625 nm) does not vary across samples [make SI figure], implying that the photoluminescence intensity measured here is proportional to the external radiative efficiency (ERE) of the absorbers. As higher ERE is proportional to the open-circuit voltage expected from a photovoltaic cell [203], we use these photoluminescence data to rank compositions for future cell development. Broadly, compositions with greater than 10% bromine content display poor photoluminescence intensity, and compositions with greater than 7% chlorine display the greatest photoluminescence intensity. [discussion on chlorine segregation -¿ passivation, chlorine contributes to crystallization process/grain growth, etc]. Despite these broad trends, the actual data are rife with local maxima, and it may be the case that narrow windows in halide composition space provide opportunity for cells.

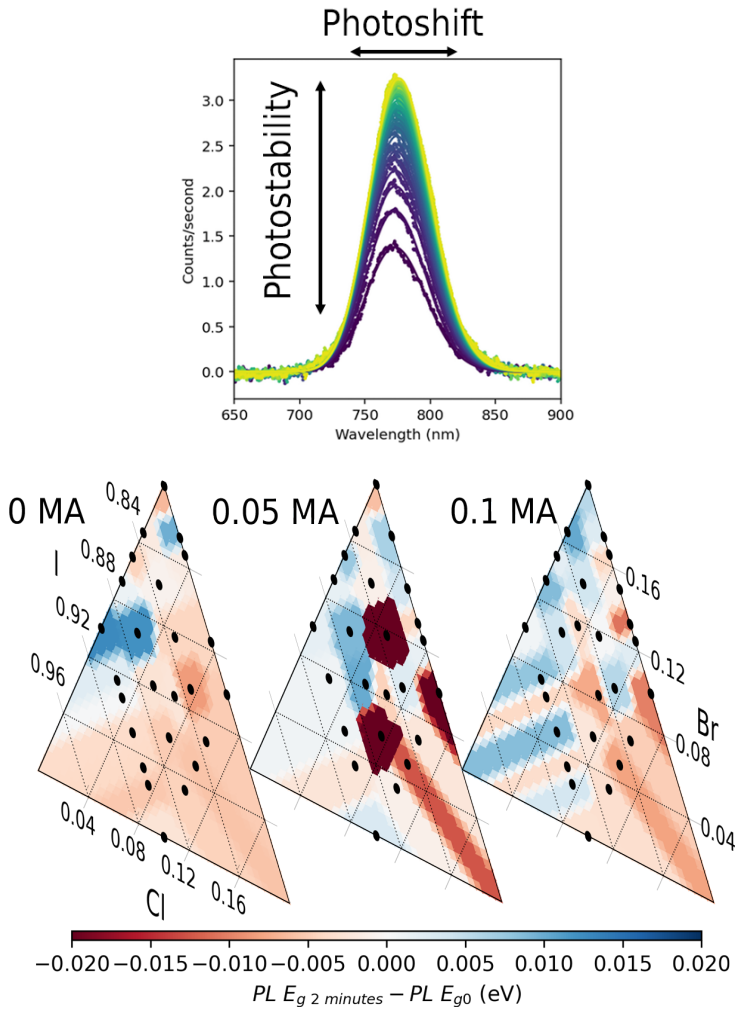

Figure 9.5. (a) Example series of photoluminescence measurements and gaussian fits used to evaluate emission photostability. (b) Shift in emission center after two minutes of exposure to intense (4 suns equivalent) 405 nm illumination.

9.3.3 Absorber Durability

Photoinduced Degradation

We test the photostability of our thin films by recording changes in photoluminescence spectra over 2 minutes of constant irradiation by a blue laser (405 nm), with power equivalent to ˜4 suns. [4/27/2022: Different from methods section? - MK] From these spectra, we extract the changes in both emission intensity and energy to evaluate a composition's photostability (Figure 9.5a).

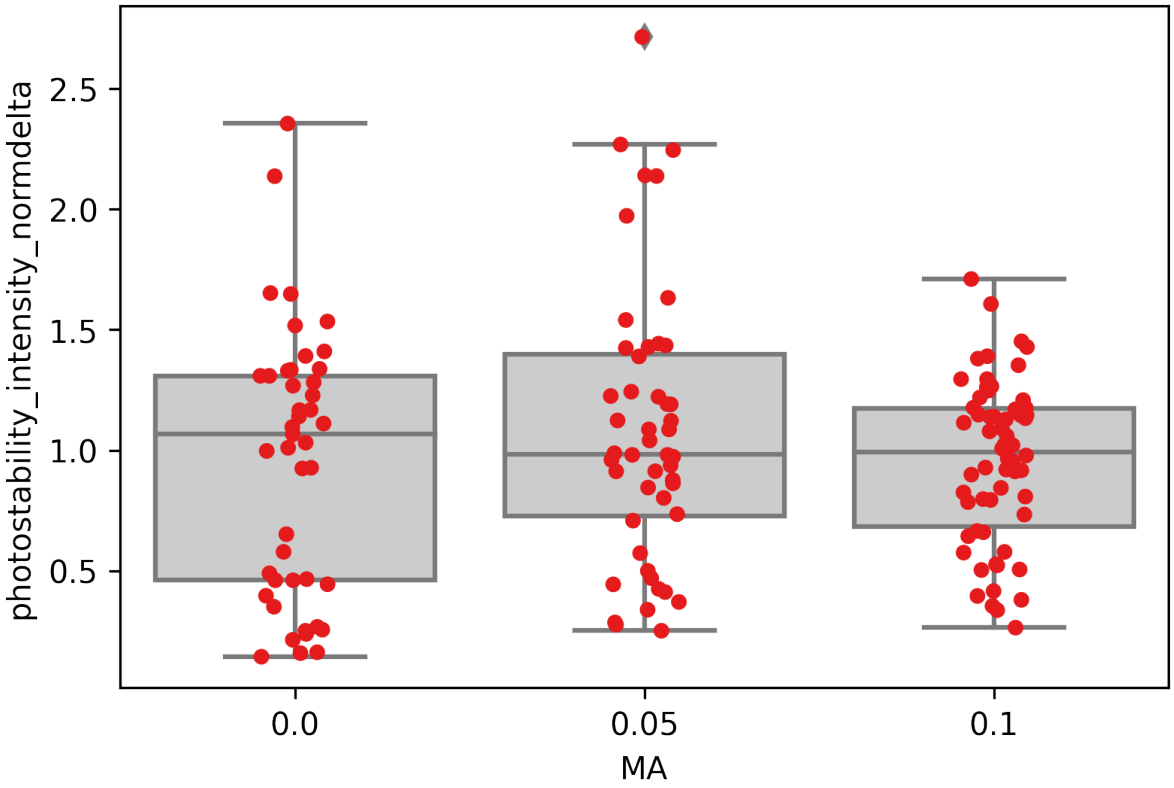

Figure 9.6. Distribution of normalized photoluminescence intensity change of films after two minutes of exposure to 4 suns equivalent 405 nm light.

Films across the composition space were seen to either “photobleach” or “photobrighten”, with final photoluminescence intensities ranging from 10% to 200% of the initial intensity (Figure PSa). We refer to this metric as photointensity. As with the PL data, the photo brightening landscape is mottled yet still reveals broad compositional trends. Compositions with ¿10% bromine mostly lose emission intensity under photoexposure. All but one photobrightening composition contain chlorine, with the largest increases in emission intensity occurring in compositions with ¿5% chlorine. As methylammonium loading increases, we see a slight narrowing in the distribution of intensity changes (p=0.008 by the Brown-Forsythe test, Figure 9.6 [204]), suggesting that the A-site composition contributes to stability of emission intensity under intense illumination[205].

Films were seen to either blueshift or redshift in emission energy under photoexposure, with all but three films shifting by less than 25 meV in either direction (Figure 9.5b). Broadly, we observe that compositions with higher chlorine fractions tend to redshift more after photoexposure (by about -10 meV/%Cl, p = 0.011, Figure 9.7).

Thermal Degradation

We test the thermal stability of our thin films by recording changes in photoluminescence spectra periodically during heating at 85°Cin a nitrogen environment. Photoluminescence intensity reduces for all films, with the majority of the reduction occuring after the first 1.5 hours of heating (Figure 9.9a). At 0 and 5% MA content, the films with the highest bromine fractions showed the most loss of photoluminescence intensity, dropping by up to three orders of magnitude (Figure 9.10). At 10% MA content, however, there is no clear relationship between halide composition and intensity loss. Averaging over all halide compositions, higher methylammonium content leads to greater losses in photoluminescence intensity after thermal degradation.

Emission energy is seen to either redshift or blueshift, with the rate of shift varying across compositions as well (Figure 9.9b). Most films blueshifted, with those with 5% or higher

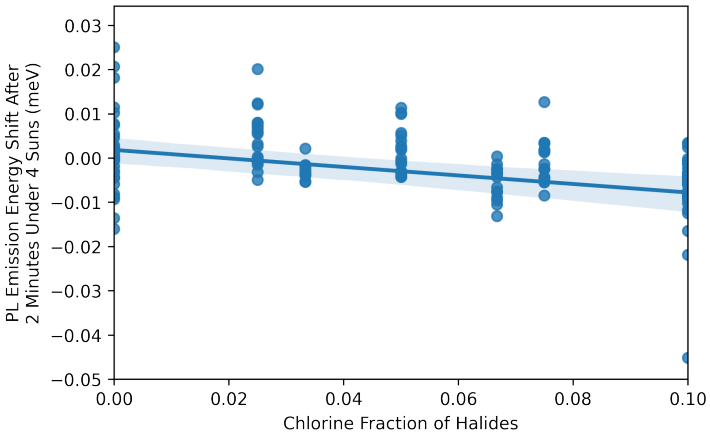

OLS Regression Results

Dep. Variable:	photostability_peakev_delta	**R-squared:**	0.041
Model:	OLS	**Adj. R-squared:**	0.035
Method:	Least Squares	**F-statistic:**	6.555
Date:	Sat, 21 May 2022	**Prob (F-statistic):**	0.0114
Time:	21:09:15	**Log-Likelihood:**	410.10
No. Observations:	155	**AIC:**	-816.2
Df Residuals:	153	**BIC:**	-810.1
Df Model:	1		
Covariance Type:	nonrobust		

	coef	**std err**	**t**	**P>|t|**	**[0.025**	**0.975]**
const	0.0018	0.002	0.775	0.440	-0.003	0.006
Cl	-0.0962	0.038	-2.560	0.011	-0.170	-0.022

Omnibus:	240.767	**Durbin-Watson:**	2.061
Prob(Omnibus):	0.000	**Jarque-Bera (JB):**	20453.396
Skew:	-6.780	**Prob(JB):**	0.00
Kurtosis:	57.618	**Cond. No.**	27.2

Figure 9.7. (a) Linear fit of photoluminescence emission energy shift against chlorine fraction for all films, and (b) fit statistics for the regression shown in (a). The points at each chlorine loading vary in bromine, chlorine, and methylammonium content.

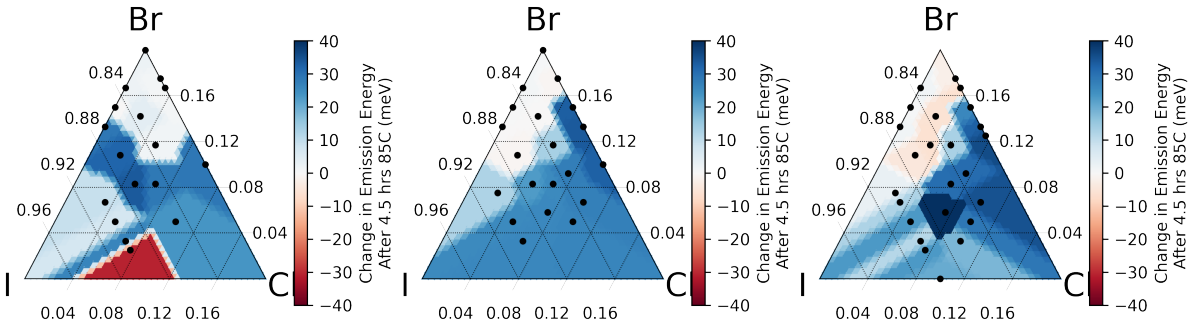

Figure 9.8. Shift in photoluminescence emission energy for films after exposure to 85°C.

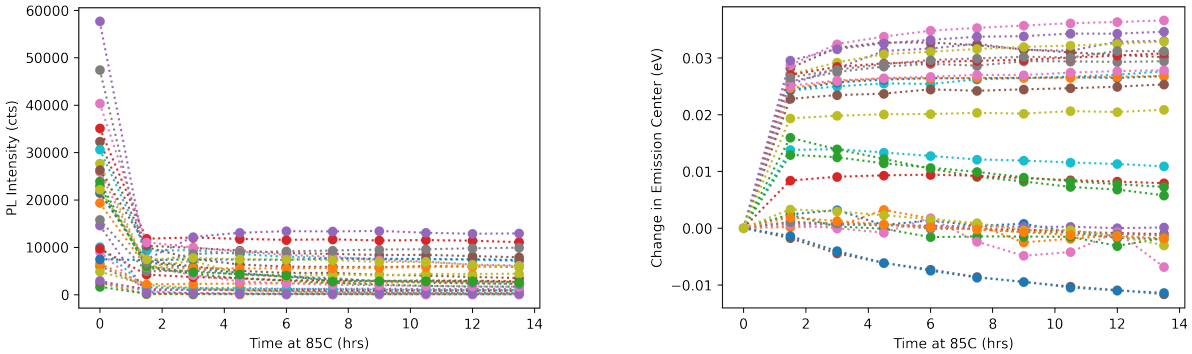

Figure 9.9. (a) Photoluminescence intensity and (b) change in emission energy for films of various compositions undergoing thermal degradation at 85°C in a nitrogen environment.

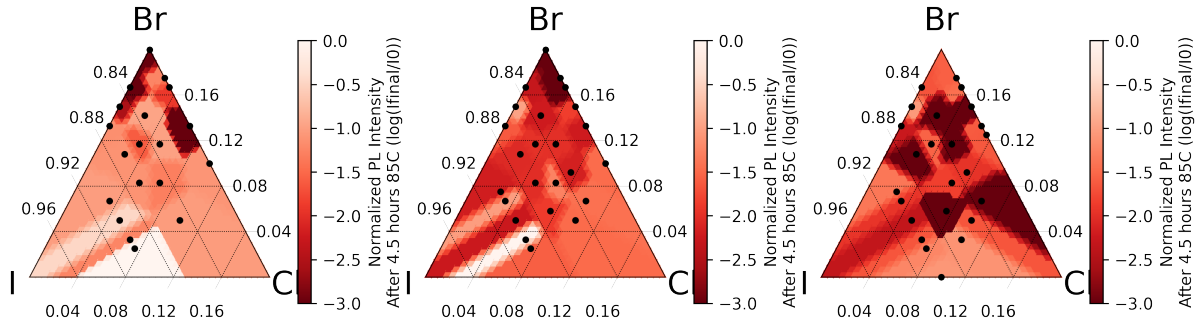

Figure 9.10. Normalized photoluminescence intensity of films after 4.5 hours of exposure to 85°C under a nitrogen environment. Darker red here represents a greater loss of intensity.

chlorine loading show the largest blueshift (up to 40 meV after 4.5 hours, Figure 9.8). Films with over 10% bromine and under 5% chlorine slightly redshifted (up to 10 meV after 4.5 hours). The methylammonium content was not seen to have an effect on emission energy shifts during thermal degradation, likely due to the moderate 85°C temperature applied.

9.3.4 Parsing the Screening Data

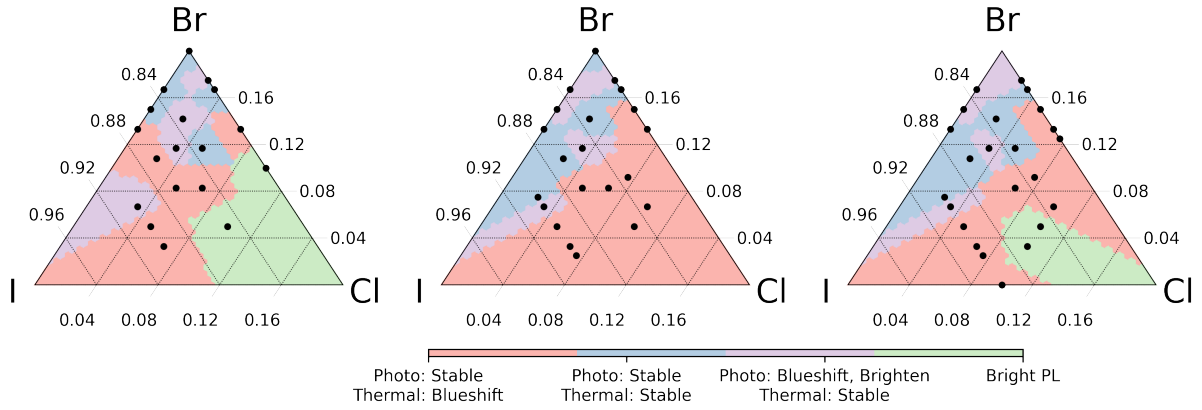

Figure 9.11. Segmentation of the compositional space into four distinct behavior regions, labeled on the colorbar. The broad behavioral trends for the four regions are labeled in on the colorbar: the red, blue, and purple regions are distinct in their response to photo and thermal stress, whereas the green region displays uniquely high photoluminescence intensity.

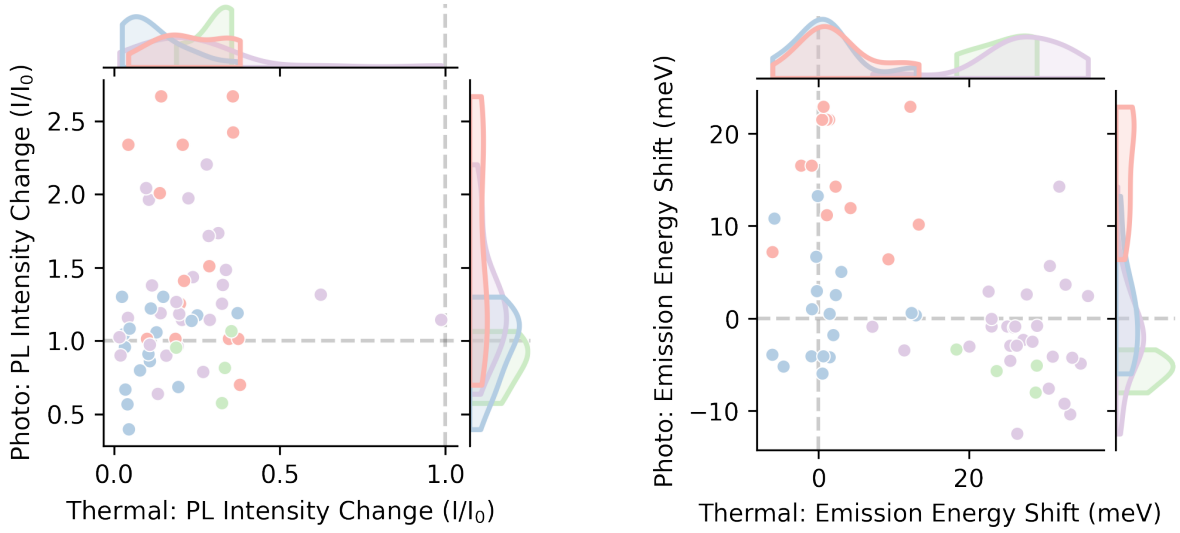

Figure 9.12. Scatterplots representing the 4 durability dimensions on which K-Means Clustering was performed to segment the compositional space into four distinct regions. Each point represents a unique absorber composition and is colored by the cluster to which that composition is assigned. The left plots display emission energy shifts under thermal and photo degradation, while the right plot shows normalized emission intensity changes under thermal and photo degradation.

Segmenting the Compositional Space into Regions of Distinct Behavior

The screening data provide multiple dimensions over which the tested absorber compositions can be compared. We use K-Means Clustering (KMC) to segment the overall compositional space into four regions of distinct behavior. Specifically, we select five screening metrics which capture the durability and potential performance of the absorbers: thermal stability (by changes in emission intensity and energy), photostability (by changes in emission intensity, and energy), and the initial photoluminescence intensity (SI Figure 9.12). The number of clusters was selected by trial-and-error – fewer than four clusters grouped disparate compositions together, while greater than four clusters only divided clusters in spurious ways that were not meaningful in our context of absorber screening. Note that the composition was not used for clustering, and that KMC does not require clusters to be contiguous in the compositional space; that KMC naturally partitioned the compositional space into four contiguous regions suggests that the total screening

data vary smoothly as composition is changed.

From the clustering process, we identify four distinct regions of absorber behavior, two of which are particularly interesting for tandem development. First, we see that many absorbers with the highest (10%) chlorine content have sufficiently high photoluminescence intensity to distinguish them from the rest of the compositions (green region in Figure 9.11). The remaining three regions are distinguished not by photoluminescence intensity, but by absorber stability against thermal and photo stressors. Compositions with over 4% chlorine tend to have a stable emission center under photoexposure, but blueshift in emission under heating. At lower chlorine loadings, the films have a stable emission energy under heating; of these compositions, some are also stable under photoexposure (blue regions), while the others blueshift and brighten in emission under photoexposure (purple regions). The purple regions exist at the boundary between blue and red regions, suggesting that the photobrightening emission behavior is a transitional property between thermally stable and thermally unstable compositions.

The methylammonium content on the absorber's A-site plays a significant role in shifting the boundaries of these four behavior regions. Most notably, the stable blue region grows with increasing methylammonium (10%) content, reducing the thermally unstable red region accordingly. The green "bright photoluminescence" region does not move with methylammonium loading, suggesting that this brightening effect is more a consequence of the halide fraction than the A-site composition.

Pareto-Optimal Compositions Within Each Segment

Armed with a segmented compositional space, we use our two main photovoltaic figures of merit – bandgap and photoluminescence intensity – to identify from each segment the most interesting compositions for investigation in perovskite-on-silicon tandems. Specifically, we select pareto-optimal compositions from each compositional segment, optimizing for proximity to the target top-cell bandgap (1.67 eV) and photoluminescence intensity (which suggests the potential open-circuit voltage of the absorber in a tandem cell) (Figure 9.13). The compositions

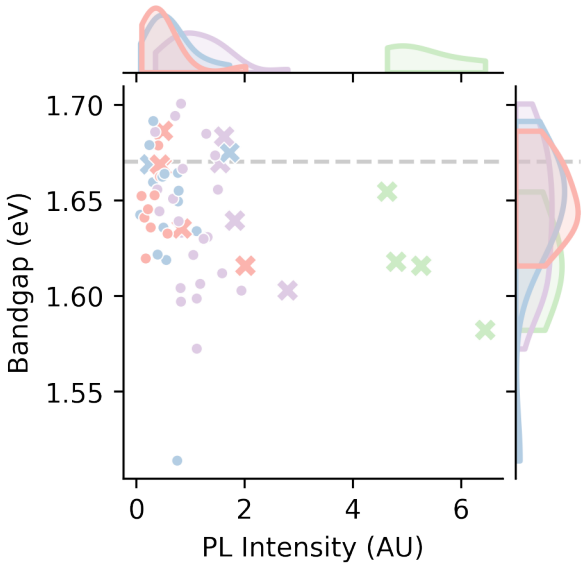

Figure 9.13. Pareto front scatterplots for the four clusters. Crosses are the pareto optimal points, and dots are the dominated points. The horizontal dashed line represents the target bandgap, the distance to which we minimize in our pareto optimization.

we suggest for further exploration are given in Table 9.1.

9.3.5 Reliability of the Screening Data

One of the primary value propositions of robotics for lab automation is superhuman precision and repeatibility. This is especially critical in the investigation of halide perovskites, which suffer from repeatability issues due to a variety of factors. The processing window for typical perovskite film fabrication is small, owing to the kinetic nature of the antisolvent-based crystal formation process. Slight variations in the spincoating procedure, such as the timing and rate of antisolvent dispensal, can significantly affect the behavior of resulting films. [206, 207, 208] The solid precursors used to fabricate perovskite thin films vary in quality from lot to lot, with potentially outsize influences on the performance of the films. [209].

These problems are avoided in our robotic workflow, in which are able to maintain precise control over all aspects of fabrication (Figure 9.2) and complete all experiments with small volumes of solutions generated from the same lot of precursors. Despite these factors,

Region	MA	I	Br	Cl	Eg (eV)	PL (a.u.)
Bright PL	0.1	0.867	0.033	0.1	1.582	6.450
	0.1	0.85	0.05	0.1	1.616	5.268
	0	0.85	0.05	0.1	1.618	4.806
	0	0.8	0.1	0.1	1.654	4.639
Photo: Stable Thermal: Stable	0	0.833	0.167	0	1.669	0.258
	0.1	0.8	0.167	0.033	1.675	1.725
Photo: Blueshift, Thermal: Stable	0.1	0.9	0.067	0.033	1.616	2.021
	0.1	0.85	0.117	0.033	1.635	0.843
	0	0.833	0.142	0.025	1.667	0.475
	0.1	0.8	0.175	0.025	1.669	0.440
	0	0.8	0.175	0.025	1.686	0.498
Photo: Stable Thermal: Blueshift	0.1	0.9	0.033	0.067	1.603	2.800
	0.1	0.833	0.067	0.1	1.639	1.826
	0.1	0.8	0.125	0.075	1.669	1.556
	0.1	0.8	0.133	0.067	1.683	1.627

Table 9.1. Pareto-optimal compositions within each durability cluster.

we still observe some variation in the films made by PASCAL. We evaluate repeatability by the coefficient of variation (CV) in various measurements of five films each of six unique compositions within our compositional space (Figure 9.14). Measures of material bandgap are most consistent, with average CV of 0.1% for photoluminescence emission energy and 0.3% for optical bandgap estimated from transmittance data. The intensity of photoluminescence varies with an average CV of 10%; this greater variation is to be expected, as radiative recombination rates within the films are sensitive to interfaces and defect states that do not affect the bulk material bandgap. More variable still are the measures of photostability. The magnitude of intensity or emission energy changes vary with CV's of 20-30%, while the rates of these changes vary with CV's of 70-100%. We expect that these photostability measures are driven by the nature of the film surfaces, as isolated tests of photostability before and after a surface treatment with phenethylammonium iodide (PEAI) show the surface passivation agent to greatly stabilize the film under photoexposure.

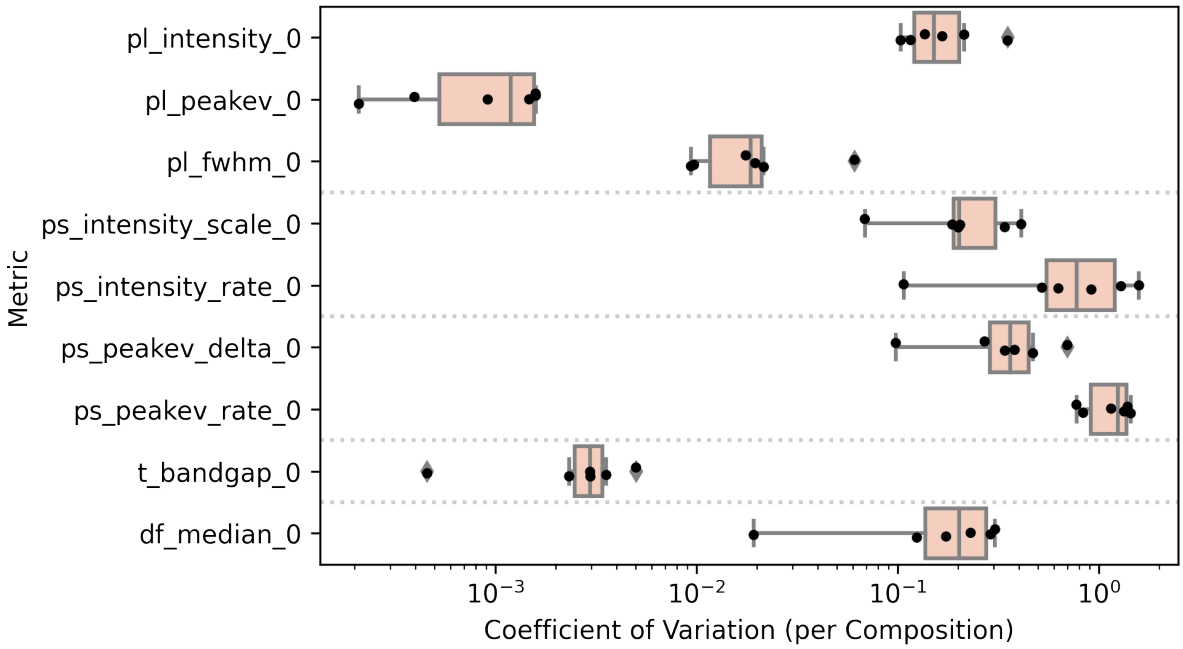

Figure 9.14. Distributions of coefficients of variation (CV) for features extracted from measurements on the PASCAL characterization line. Each dot represents the CV for five films fabricated and tested of a single composition. The box plots therefore show the distribution of CV for each of the features labeled on the y-axis. Features between the dotted lines are extracted from the same characterization mode. From top to bottom, the features are: 1) intensity, 2) emission energy, and 3) full-width half max of the photoluminescence spectra. 4) normalized intensity (I/I_0), 5) rate of intensity change (k from an exponential decay fit $I = I_0 e^{-k/T}$), 6) change in emission energy ($E - E_0$), and 7) rate of energy change across two minutes of exposure to 4 suns 405 nm light. 8) bandgap of the films, measured from Tauc analysis of transmittance spectra. 9) a metric of film roughness from the darkfield imaging.

9.4 Conclusion

Our experimental screening results lay the foundation for informed development of wide bandgap halide perovskite absorbers for perovskite-on-silicon tandems. We confirm that chlorine addition does widen the absorber bandgap to a point, identifying a solubility limit of chlorine in our ”kitchen-sink” inspired compositional space. Many compositions are shown to have suitable bandgaps for top cells, using addition of bromine, chlorine, or both to the prototypical iodine perovskite. A small amount of chlorine addition greatly increases the photoluminescence, implying that chlorine addition is important to maximize the open-circuit voltage of top cells. Too

much chlorine, however, reduces the thermal stability of the films. Using the photoluminescence intensity, photostability, and thermal stability, the tested compositions broadly fall into four regions of behavior, within each we have cooptimized bandgap and photoluminescence intensity to identify the most promising absorber compositions for further investigation.

Beyond the screening results, our work shows the value of automation in investigation of halide perovskites. The total data discussed in this work were acquired over about 48 hours of machine time using about 10 milliliters of precursor solutions. The throughput, material efficiency, and process precision afforded by PASCAL mitigate practical issues of variability in precursors, degradation of stock solutions, and operator error that plague studies of spincoated halide perovskites. These factors provide us with confidence that the trends identified by our screening reflect composition-driven material behavior.

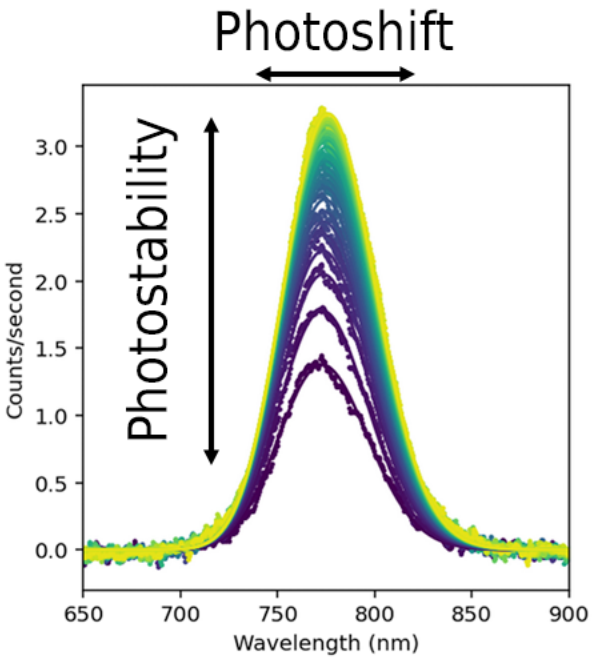

Figure 9.15. Example of a single photostability measurement. Each photoluminescence spectrum plotted above is acquired in sequence for 2 seconds, totaling 60 spectra for 2 minutes of constant illumination by the 4-suns 405nm laser degradation/excitation source. Gaussian fits to each individual spectrum are used to extract the emission energy, intensity, and full-width half-max, which are in turn tracked over the 2 minutes to gauge sample photostability.

9.5 Acknowledgements

Chapter 9, in part, is currently being prepared for submission as ”Robotic High Throughput Screening Identifies Durable Halide Perovskite Absorbers for Tandem Photovoltaics” by Kumar, R. E., Kodur, M., Cakan, Deniz N., and Fenning, D. P. The dissertation author is the primary investigator and author of this material.

Chapter 10

Conclusion

This thesis consists of both technical and scientific contributions.

The technical contributions fall under three thrusts. First, I presented a nondestructive method for quantitative mapping of water content within industry-standard silicon photovoltaic modules (Chapter 2). This enables for direct measurement of moisture ingress, which has otherwise remained a somewhat hidden variable during the accelerated environmental tests relied upon by industry and academic researchers of photovoltaic durability. Second, I constructed a ray-tracing method for the correlation of sequential spatially-resolved measurements of a given sample (Chapter 5). This enables us to register multimodal microscopy data which are each systematically corrupted by geometric factors and local probe-sample interactions, ultimately enabling us to draw the correlations such as structure-property relationships that are integral to the study of materials. Third, I developed a platform for automated fabrication and testing of spin-coated optoelectronic thin films (Chapter 6). Beyond the hardware, I presented software tools to enable facile use of the tool by experimentalists. MixSol plans solution mixing paths from arbitrary sets of available solutions to target solutions, which has value to any researcher or automation plaform that works on solution-based processes (Chapter 8). Roboflo creates job schedules for materials automation platforms, improving the efficiency of said platforms by allowing many experiments to be run in parallel (Chapter 7). Roboflo is designed and closed-loop automation in mind, and is capable of scheduling new jobs around existing jobs. These steps are

critical to realizing the potential of lab automation platforms in general. As such, the software tools described in this dissertation are all publicly available and actively maintained on GitHub.

The scientific contributions also fall under three thrusts. In Chapter 3 I quantified local correlations between moisture content and performance losses in silicon photovoltaic modules. While studies of moisture on module durability are common, results are almost entirely evaluated on overall module performance losses, which we show to arise from a set of distinct degradation modes within a given module. Dissection of the local performance losses allows us to determine the contribution of each mode to the overall module performance loss. Furthermore, we show how these distinct modes present as a function of the temperature and humidity of the module environment, and as a function of the module architecture. The results of this study should inform choice of module architecture by deployment environment. In Chapter 4, I show the interplay of structure, composition, optoelectronics, and stability in europium-doped cesium lead bromide perovskite. These results show that europium addition reduces nanoscopic structural disorder within the perovskite, improving luminescence and increasing the x-ray hardness of the material – the combination of which shows Eu:$CsPbBr_3$ to be a promising material for construction of high-energy photon detectors. In Chapter 9, I experimentally screen a large number of halide perovskite compositions for potential application as wide-bandgap top cells in perovskite-on-silicon tandem photovoltaic cells. If halide perovskites are to be deployed industrially as photovoltaics, this is the likely application. Our screening evaluates absorbers not only on figures of merit for initial performance (photoluminescence intensity), but on measures of stability to stressors expected during operation (illumination and heat). This combined set of metrics is required to ensure that the downstream development from films to full solar cells – a costly endeavor – is focused on compositions that are both stable and performant.

Bibliography

[1] C. J. Rhodes, "Solar energy: principles and possibilities," *Science progress*, vol. 93, no. 1, pp. 37–112, 2010.

[2] M. R. Hannah Ritchie and P. Rosado, "Energy," *Our World in Data*, 2020. https://ourworldindata.org/energy.

[3] D. U.S., "The sunshot 2030 goals: 3¢ per kilowatt hour for pv and 5 ¢ per killowatt hour for dispatchable csp," p. 2–6, 2017.

[4] M. Woodhouse, R. Jones-Albertus, D. Feldman, R. Fu, K. Horowitz, D. Chung, D. Jordan, and S. Kurtz, "The role of advancements in solar photovoltaic efficiency, reliability, and costs," *NREL*, p. 38, 2016.

[5] S. R. Wenham and M. A. Green, "Silicon solar cells," *Progress in Photovoltaics: Research and Applications*, vol. 4, no. 1, p. 3–33, 1996.

[6] W. Shockley and H. J. Queisser, "Detailed balance limit of efficiency of ¡i¿p-n¡/i¿ junction solar cells," *Journal of Applied Physics*, vol. 32, no. 3, p. 510–519, 1961.

[7] A. Kojima, K. Teshima, Y. Shirai, and T. Miyasaka, "Organometal halide perovskites as visible-light sensitizers for photovoltaic cells," *Journal of the American Chemical Society*, vol. 131, no. 17, pp. 6050–6051, 2009. PMID: 19366264.

[8] H. Min, D. Y. Lee, J. Kim, G. Kim, K. S. Lee, J. Kim, M. J. Paik, Y. K. Kim, K. S. Kim, M. G. Kim, T. J. Shin, and S. Il Seok, "Perovskite solar cells with atomically coherent interlayers on sno2 electrodes," *Nature*, vol. 598, no. 7881, pp. 444–450, 2021.

[9] B. Saparov and D. B. Mitzi, "Organic-Inorganic Perovskites: Structural Versatility for Functional Materials Design," *Chemical Reviews*, vol. 116, no. 7, pp. 4558–4596, 2016.

[10] M. Saliba, C. M. Wol, M. Stolterfoht, N. Phung, S. Albrecht, D. Neher, and A. Abate, "How to Make over 20% E ffi cient Perovskite Solar Cells in Regular (n i p) and Inverted (p i n) Architectures," *Chemistry of Materials*, vol. 30, pp. 4193–4201, 2018.

[11] S. P. Dunfield, L. Bliss, F. Zhang, J. M. Luther, K. Zhu, M. F. A. M. Hest, M. O. Reese, and J. J. Berry, "From defects to degradation: A mechanistic understanding of degradation in perovskite solar cell devices and modules," *Advanced Energy Materials*, vol. 10, no. 26, p. 1904054, 2020.

[12] S. Macpherson, T. A. S. Doherty, A. J. Winchester, S. Kosar, D. N. Johnstone, Y.-H. Chiang, K. Galkowski, M. Anaya, K. Frohna, A. N. Iqbal, S. Nagane, B. Roose, Z. Andaji-Garmaroudi, K. W. P. Orr, J. E. Parker, P. A. Midgley, K. M. Dani, and S. D. Stranks, "Local nanoscale phase impurities are degradation sites in halide perovskites," *Nature*, 2022.

[13] M. V. Khenkin, E. A. Katz, A. Abate, G. Bardizza, J. J. Berry, C. Brabec, F. Brunetti, V. Bulović, Q. Burlingame, A. Di Carlo, R. Cheacharoen, Y.-B. Cheng, A. Colsmann, S. Cros, K. Domanski, M. Dusza, C. J. Fell, S. R. Forrest, Y. Galagan, D. Di Girolamo, M. Grätzel, A. Hagfeldt, E. von Hauff, H. Hoppe, J. Kettle, H. Köbler, M. S. Leite, S. Liu, Y.-L. Loo, J. M. Luther, C.-Q. Ma, M. Madsen, M. Manceau, M. Matheron, M. McGehee, R. Meitzner, M. K. Nazeeruddin, A. F. Nogueira, Odabaşı, A. Osherov, N.-G. Park, M. O. Reese, F. De Rossi, M. Saliba, U. S. Schubert, H. J. Snaith, S. D. Stranks, W. Tress, P. A. Troshin, V. Turkovic, S. Veenstra, I. Visoly-Fisher, A. Walsh, T. Watson, H. Xie, R. Yıldırım, S. M. Zakeeruddin, K. Zhu, and M. Lira-Cantu, "Consensus statement for stability assessment and reporting for perovskite photovoltaics based on isos procedures," *Nature Energy*, vol. 5, no. 1, p. 35–49, 2020.

[14] N. Li, X. Niu, Q. Chen, and H. Zhou, "Towards commercialization: The operational stability of perovskite solar cells," *Chemical Society Reviews*, vol. 49, no. 22, pp. 8235–8286, 2020.

[15] J. H. Wohlgemuth and S. Kurtz, "Using accelerated testing to predict module reliability," in *Conference Record of the IEEE Photovoltaic Specialists Conference*, pp. 003601–003605, IEEE, 2011.

[16] P. Hacke, S. Spataru, K. Terwilliger, G. Perrin, S. Glick, S. Kurtz, and J. Wohlgemuth, "Accelerated testing and modeling of potential-induced degradation as a function of temperature and relative humidity," *IEEE Journal of Photovoltaics*, vol. 5, no. 6, p. 1549–1553, 2015.

[17] M. D. Kempe, G. J. Jorgensen, K. M. Terwilliger, T. J. McMahon, C. E. Kennedy, and T. T. Borek, "Acetic acid production and glass transition concerns with ethylene-vinyl acetate used in photovoltaic devices," *Solar Energy Materials and Solar Cells*, vol. 91, no. 4, p. 315–329, 2007.

[18] G. TamizhMani and J. Kuitche, "Accelerated Lifetime Testing of Photovoltaic Modules Solar America Board for Codes and Standards," *Solar ABC*, no. July, p. 106, 2013.

[19] C. Peike, S. Hoffmann, P. Hülsmann, B. Thaidigsmann, K. A. Weiß, M. Koehl, and P. Bentz, "Origin of damp-heat induced cell degradation," *Solar Energy Materials and Solar Cells*, vol. 116, p. 49–54, 2013.

[20] M. Quintana, D. King, T. McMahon, and C. Osterwald, "Commonly observed degradation in field-aged photovoltaic modules," pp. 1436–1439, 2003.

[21] B. A. Gwandu and D. J. Creasey, "Humidity: A factor in the appropriate positioning of a photovoltaic power station," *Renewable Energy*, vol. 6, pp. 313–316, apr 1995.

[22] H. A. Kazem, "Effect of Humidity on Photovoltaic Performance Based on Experimental Study," *International Journal of Applied Engineering Research*, vol. 10, no. 23, pp. 4357–43577, 2016.

[23] M. Bora, S. Pop, R. Schulze, M. Rowell, and D. Harwood, "Moisture content imaging in glass-glass and glass-backsheet photovoltaic mini-modules," in *Moisture content imaging in glass-glass and glass-backsheet photovoltaic mini-modules*, vol. 2020 47th IEEE Photovoltaic Specialists Conference (PVSC), pp. 1485–1488, IEEE, 2020.

[24] M. Bora, V. Lordi, and J. B. Varley, "Water ingress mapping in photovoltaic module packaging materials," vol. 2018 IEEE 7th World Conference on Photovoltaic Energy Conversion, p. 1252–1254, 2018.

[25] J. Hepp, A. Vetter, S. Langner, M. Woiton, G. Jovicic, K. Burlafinger, J. A. Hauch, C. Camus, H.-J. Egelhaaf, and C. J. Brabec, "Infrared Absorption Imaging of Water Ingress Into the Encapsulation of (Opto-)Electronic Devices," *IEEE Journal of Photovoltaics*, vol. PP, pp. 1–7, 2018.

[26] J. Kapur, K. Proost, C. A. Smith, and E. I. D. D. Nemours, "Determination of moisture ingress through various encapsulants in glass/glass laminates," *Conference Record of the IEEE Photovoltaic Specialists Conference*, vol. 1, pp. 001210–001214, 2009.

[27] C. Peike, T. Kaltenbach, K.-A. Weiß, and M. Koehl, "Non-destructive degradation analysis of encapsulants in PV modules by Raman Spectroscopy," *Solar Energy Materials and Solar Cells*, vol. 95, pp. 1686–1693, jul 2011.

[28] T. Carlsson, P. Konttinen, U. Malm, and P. Lund, "Absorption and desorption of water in glass/ethylene-vinyl-acetate/glass laminates," *Polymer Testing*, vol. 25, no. 5, pp. 615–622, 2006.

[29] M. Jankovec, F. Galliano, E. Annigoni, H. Y. Li, F. Sculati-Meillaud, L.-E. Perret-Aebi, C. Ballif, and M. Topic, "¡italic¿in-situ¡/italic¿ monitoring of moisture ingress in pv modules using digital humidity sensors," *IEEE Journal of Photovoltaics*, vol. 6, no. 5, p. 1152–1159, 2016.

[30] M. D. Kempe, "Modeling of rates of moisture ingress into photovoltaic modules," *Solar Energy Materials and Solar Cells*, vol. 90, no. 16, pp. 2720–2738, 2006.

[31] P. Hülsmann and K.-A. A. Weiss, "Simulation of water ingress into PV-modules: IEC-testing versus outdoor exposure," may 2015.

[32] M. Owen-Bellini, D. B. Sulas-Kern, G. Perrin, H. North, S. Spataru, and P. Hacke, "Methods for in situ electroluminescence imaging of photovoltaic modules under varying environmental conditions," *IEEE Journal of Photovoltaics*, vol. 10, no. 5, p. 1254–1261, 2020.

[33] D. B. Sulas-Kern, S. Johnston, M. Owen-Bellini, K. Terwilliger, J. Meydbray, L. Spinella, A. Sinha, L. T. Schelhas, and D. C. Jordan, "Uv-fluorescence imaging of silicon pv modules after outdoor aging and accelerated stress testing," in *UV-Fluorescence Imaging of Silicon PV Modules After Outdoor Aging and Accelerated Stress Testing*, vol. 2020 47th IEEE Photovoltaic Specialists Conference (PVSC), pp. 1444–1448, IEEE, 2020.

[34] R. Bhoopathy, O. Kunz, M. Juhl, T. Trupke, and Z. Hameiri, "Outdoor photoluminescence imaging of photovoltaic modules with sunlight excitation," *Progress in Photovoltaics: Research and Applications*, vol. 26, no. 1, p. 69–73, 2018.

[35] J. Karas, L. Michaelson, K. Munoz, M. Jobayer Hossain, E. Schneller, K. O. Davis, S. Bowden, and A. Augusto, "Degradation of copper-plated silicon solar cells with damp heat stress," *Progress in Photovoltaics: Research and Applications*, vol. 28, no. 11, p. 1175–1186, 2020.

[36] M. D. Kempe, "Modeling of rates of moisture ingress into photovoltaic modules," *Solar Energy Materials and Solar Cells*, vol. 90, no. 16, p. 2720–2738, 2006.

[37] N. Bosco, M. Springer, and X. He, "Viscoelastic material characterization and modeling of photovoltaic module packaging materials for direct finite-element method input," *IEEE Journal of Photovoltaics*, vol. 10, no. 5, p. 1424–1440, 2020.

[38] G. Oreski, A. Mihaljevic, Y. Voronko, and G. C. Eder, "Acetic acid permeation through photovoltaic backsheets: Influence of the composition on the permeation rate," *Polymer Testing*, vol. 60, 2017.

[39] A. Mannodi-Kanakkithodi, R. Kumar, D. Fenning, and M. Chan, "First principles modeling of polymer encapsulant degradation in si photovoltaic modules.," *Phys Chem Chem Phys*, 2021.

[40] O. Hasan and A. F. Arif, "Performance and life prediction model for photovoltaic modules: Effect of encapsulant constitutive behavior," *Solar Energy Materials and Solar Cells*, vol. 122, p. 75–87, 2014.

[41] M. Gagliardi, P. Lenarda, and M. Paggi, "A reaction-diffusion formulation to simulate eva polymer degradation in environmental and accelerated ageing conditions," *Solar Energy Materials and Solar Cells*, vol. 164, p. 93–106, 2017.

[42] B. Han and D.-S. Kim, "Moisture ingress, behavior, and prediction inside semiconductor packaging: A review," *Journal of Electronic Packaging*, 2017.

[43] L. Papargyri, M. Theristis, B. Kubicek, T. Krametz, C. Mayr, P. Papanastasiou, and G. E. Georghiou, "Modelling and experimental investigations of microcracks in crystalline silicon photovoltaics: A review," *Renewable Energy*, vol. 145, p. 2387–2408, 2020.

[44] G. E. Walrafen and E. Pugh, "Raman Combinations and Stretching Overtones from Water, Heavy Water, and NaCl in Water at Shifts to ca. 7000 cm ⁻¹," *Journal of Solution Chemistry*, vol. 33, pp. 81–97, jan 2004.

[45] M. D. Kempe, "Control of moisture ingress into photovoltaic modules," *31st IEEE Photovoltaic Specialists Conference*, no. February, pp. 503–506, 2005.

[46] J. a. Curcio and C. C. Petty, "The Near Infrared Absorption Spectrum of Liquid Water," *Journal of the Optical Society of America*, vol. 41, no. 5, p. 302, 1951.

[47] A. Savitsky and M. J. Golay, "Smoothing and Differentiation of Data by Simplified Least Squares Procedures," *Analytical Chemistry*, vol. 36, no. 1, pp. 1627–1638, 1964.

[48] Y. Ren, M. Shimoyama, T. Ninomiya, K. Matsukawa, H. Inoue, I. Noda, and Y. Ozaki, "Two-dimensional near-infrared correlation spectroscopy studies on composition-dependent spectral variations in ethylene/vinyl acetate copolymers: Assignments of bands due to ethylene units in amorphous, disordered, and orthorhombic crystalline phases," *Applied Spectroscopy*, vol. 53, no. 8, pp. 919–926, 1999.

[49] K. Morokuma, "Molecular Orbital Studies of Hydrogen Bonds. III. C=O···H–O Hydrogen Bond in H ₂ CO···H ₂ O and H ₂ CO···2H ₂ O," *The Journal of Chemical Physics*, vol. 55, no. 3, pp. 1236–1244, 1971.

[50] B. Nelander, "Infrared spectrum of the water formaldehyde complex in solid argon and solid nitrogen," *The Journal of Chemical Physics*, vol. 72, no. 1, pp. 77–84, 1980.

[51] G. R. Strobl and W. Hagedorn, "Raman Spectroscopic Method for Determining the Crystallinity of Polyethylene.," *AIP Conf Proc*, vol. 16, no. 7, pp. 1181–1193, 1978.

[52] M. Mizushima, T. Kawamura, K. Takahashi, and K. H. Nitta, "In situ near-infrared spectroscopic studies of the structural changes of polyethylene during melting," *Polymer Journal*, 2012.

[53] S. Watanabe, J. Dybal, K. Tashiro, and Y. Ozaki, "A near-infrared study of thermally induced structural changes in polyethylene crystal," *Polymer*, vol. 47, no. 6, pp. 2010–2017, 2006.

[54] V. Thomsen, D. Schatzlein, and D. Mercuro, "Limits of Detection in Spectroscopy," *Dictionary of Statistics & Methodology*, vol. 18, no. 12, pp. 112–114, 2015.

[55] J. Samenow, "Iran city hits suffocating heat index of 165 degrees, near world record," jul 2015.

[56] R. E. Kumar, G. V. Gastrow, J. Leslie, R. Meier, M. I. Bertoni, and D. P. Fenning, "Quantitative determination of moisture content in solar modules by short-wave infrared reflectometry," *IEEE Journal of Photovoltaics*, vol. 9, no. 6, p. 1748–1753, 2019.

[57] C. Shen, H. Kampwerth, M. Green, T. Trupke, J. Carstensen, and A. Schütt, "Spatially resolved photoluminescence imaging of essential silicon solar cell parameters and comparison with cello measurements," *Solar Energy Materials and Solar Cells*, vol. 109, p. 77–81, 2013.

[58] N. Otsu, "A threshold selection method from gray-level histograms," *IEEE transactions on systems, man, and cybernetics*, vol. 9, no. 1, p. 62–66, 1979.

[59] A. M. Jeffries, T. Nietzold, L. T. Schelhas, and M. I. Bertoni, "Corrosion of novel reactive silver ink and commercial silver-based metallizations in diluted acetic acid," *Solar Energy Materials and Solar Cells*, vol. 223, p. 110900, 2021.

[60] H. B. Mann and D. R. Whitney, "On a test of whether one of two random variables is stochastically larger than the other," *The annals of mathematical statistics*, p. 50–60, 1947.

[61] I. Duerr, J. Bierbaum, J. Metzger, J. Richter, and D. Philipp, "Silver grid finger corrosion on snail track affected pv modules–investigation on degradation products and mechanisms," *Energy Procedia*, vol. 98, p. 74–85, 2016.

[62] A. M. Jeffries and M. I. Bertoni, "Reactive silver ink as a novel low-temperature metallization: Monitoring corrosion," in *Reactive Silver Ink as a Novel Low-Temperature Metallization: Monitoring Corrosion*, vol. 2018 IEEE 7th World Conference on Photovoltaic Energy Conversion (WCPEC)(A Joint Conference of 45th IEEE PVSC, 28th PVSEC 34th EU PVSEC), pp. 1013–1017, IEEE, 2018.

[63] S. K. Tippabhotla, N. G. Diesta, X. Zhang, S. Sridhara, C. Stan, N. Tamura, A. A. Tay, and A. Budiman, "Thermomechanical residual stress evaluation in multi-crystalline silicon solar cells of photovoltaic modules with different encapsulation polymers using synchrotron x-ray microdiffraction," *Solar Energy Materials and Solar Cells*, vol. 193, p. 387–402, 2019.

[64] S. Dietrich, M. Pander, M. Sander, S. H. Schulze, and M. Ebert, "Mechanical and thermomechanical assessment of encapsulated solar cells by finite-element-simulation," in *Mechanical and thermomechanical assessment of encapsulated solar cells by finite-element-simulation* (N. G. Dhere, J. H. Wohlgemuth, and K. Lynn, eds.), SPIE, 2010.

[65] A. J. Beinert, P. Romer, M. Heinrich, M. Mittag, J. Aktaa, and D. H. Neuhaus, "The effect of cell and module dimensions on thermomechanical stress in pv modules," *IEEE Journal of Photovoltaics*, vol. 10, no. 1, p. 70–77, 2020.

[66] F. Kraemer and S. Wiese, "Assessment of long term reliability of photovoltaic glass–glass modules vs. glass-back sheet modules subjected to temperature cycles by fe-analysis," *Microelectronics Reliability*, vol. 55, no. 5, p. 716–721, 2015.

[67] L. Rendler, P. Romer, A. Beinert, J. Walter, S. Stecklum, A. Kraft, U. Eitner, and S. Wiese, "Thermomechanical stress in solar cells: Contact pad modeling and reliability analysis," *Solar Energy Materials and Solar Cells*, vol. 196, p. 167–177, 2019.

[68] P. Chaturvedi, B. Hoex, and T. M. Walsh, "Broken metal fingers in silicon wafer solar cells and pv modules," *Solar Energy Materials and Solar Cells*, vol. 108, p. 78–81, 2013.

[69] F. Kraemer, J. Seib, E. Peter, and S. Wiese, "Mechanical stress analysis in photovoltaic cells during the string-ribbon interconnection process," in *Mechanical stress analysis in photovoltaic cells during the string-ribbon interconnection process*, vol. 2014 15th International Conference on Thermal, Mechanical and Mulit-Physics Simulation and Experiments in Microelectronics and Microsystems (EuroSimE), pp. 1–7, IEEE, 2014.

[70] M. Sander and S. Dietrich, "Influence of manufacturing processes and subsequent weathering on cell cracks in pv modules," *28th EU PVSEC*, 2013.

[71] V. Handara, I. Radchenko, S. Tippabhotla, K. R.Narayanan, G. Illya, M. Kunz, N. Tamura, and A. Budiman, "Probing stress and fracture mechanism in encapsulated thin silicon solar cells by synchrotron x-ray microdiffraction," *Solar Energy Materials and Solar Cells*, vol. 162, p. 30–40, 2017.

[72] ITRPV, "International technology roadmap for photovoltaic 2020," 2020.

[73] M. T. Zarmai, N. Ekere, C. Oduoza, and E. H. Amalu, "A review of interconnection technologies for improved crystalline silicon solar cell photovoltaic module assembly," *Applied Energy*, vol. 154, p. 173–182, 2015.

[74] M. Kreuzer, S. Stamenković, S. Chen, P. Andjus, and T. Dučić, "Lipids status and copper in a single astrocyte of the rat model for amyotrophic lateral sclerosis: Correlative synchrotron-based x-ray and infrared imaging.," *J Biophotonics*, vol. 13, no. 10, p. e202000069, 2020.

[75] B. De Samber, R. Evens, K. De Schamphelaere, G. Silversmit, B. Masschaele, T. Schoonjans, B. Vekemans, C. R. Janssen, L. Van Hoorebeke, I. Szalóki, F. Vanhaecke, G. Falkenberg, and L. Vincze, "A combination of synchrotron and laboratory x-ray techniques for studying tissue-specific trace level metal distributions in daphnia magna," *Journal of Analytical Atomic Spectrometry*, vol. 23, no. 6, p. 829, 2008.

[76] *Co-registration of Synchrotron Radiation-microCT and micro-MRI images: a new method for the complete characterization of newly-formed bone*, vol. Proc. Intl. Soc. Mag. Reson. Med 22, 2014.

[77] *The Impacts and Origins of A-site Instability in Formamidinium-Cesium Lead Iodide Perovskite Solar Cells Under Extended Operation*, vol. 2020 47th IEEE Photovoltaic Specialists Conference (PVSC), IEEE, 2020.

[78] X. L. Quinn, R. E. Kumar, M. Kodur, D. N. Cakan, Z. Cai, T. Zhou, M. V. Holt, and D. P. Fenning, "Europium addition reduces local structural disorder and enhances photoluminescent yield in perovskite cspbbr 3," *Adv. Optical Mater.*, p. 2002221, 2021.

[79] M. Kodur, R. E. Kumar, Y. Luo, D. N. Cakan, X. Li, M. Stuckelberger, and D. P. Fenning, "X-ray microscopy of halide perovskites: Techniques, applications, and prospects," *Advanced Energy Materials*, vol. 10, no. 26, pp. 1–25, 2020.

[80] Y. Luo, S. Aharon, M. Stuckelberger, E. Magaña, B. Lai, M. I. Bertoni, L. Etgar, and D. P. Fenning, "The Relationship between Chemical Flexibility and Nanoscale Charge Collection in Hybrid Halide Perovskites," *Advanced Functional Materials*, vol. 28, p. 1706995, may 2018.

[81] B. M. West, M. Stuckelberger, A. Jeffries, S. Gangam, B. Lai, B. Stripe, M. I. Bertoni, J. Maser, V. Rose, S. Vogt, M. I. Bertoni, IUCr, J. Maser, V. Rose, S. Vogt, and M. I. Bertoni, "X-ray fluorescence at nanoscale resolution for multicomponent layered structures: A solar cell case study," *Journal of Synchrotron Radiation*, vol. 24, pp. 288–295, jan 2017.

[82] M. Stuckelberger, B. West, T. Nietzold, B. Lai, J. M. Maser, V. Rose, and M. I. Bertoni, "Engineering solar cells based on correlative X-ray microscopy," *Journal of Materials Research*, vol. 32, pp. 1825–1854, may 2017.

[83] Y. Zhou, H. Zhou, J. Deng, W. Cha, and Z. Cai, "Decisive structural and functional characterization of halide perovskites with synchrotron," *Matter*, vol. 2, p. 360–377, 2020.

[84] B. Beckhoff, B. Kanngießer, N. Langhoff, R. Wedell, and H. Wolff, *Handbook of Practical X-Ray Fluorescence Analysis*. Springer Science Business Media, 2007.

[85] P. Pfalzer, J. P. Urbach, M. Klemm, S. Horn, M. L. Den Boer, A. I. Frenkel, and J. P. Kirkland, "Elimination of self-absorption in fluorescence hard-x-ray absorption spectra," *Physical Review B - Condensed Matter and Materials Physics*, vol. 60, no. 13, p. 9335–9339, 1999.

[86] S.-M. Bak, Z. Shadike, R. Lin, X. Yu, and X.-Q. Yang, "In situ/operando synchrotron-based x-ray techniques for lithium-ion battery research," *NPG Asia Materials*, vol. 10, no. 7, pp. 563–580, 2018.

[87] D. A. Shapiro, Y.-s. S. Yu, T. Tyliszczak, J. Cabana, R. Celestre, W. Chao, K. Kaznatcheev, A. L. D. Kilcoyne, F. Maia, S. Marchesini, Y. S. Meng, T. Warwick, L. L. Yang, and H. A. Padmore, "Chemical composition mapping with nanometre resolution by soft x-ray microscopy," *Nature Photonics*, vol. 8, no. 10, p. 765–769, 2014.

[88] F. Meirer and B. M. Weckhuysen, "Spatial and temporal exploration of heterogeneous catalysts with synchrotron radiation," *Nature Reviews Materials*, vol. 3, no. 9, p. 324–340, 2018.

[89] J. Becher, T. L. Sheppard, Y. Fam, S. Baier, W. Wang, D. Wang, S. Kulkarni, T. F. Keller, M. Lyubomirskiy, D. Brueckner, M. Kahnt, A. Schropp, C. G. Schroer, and J.-D. Grunwaldt, "Mapping the pore architecture of structured catalyst monoliths from nanometer to centimeter scale with electron and x-ray tomographies," *The Journal of Physical Chemistry C*, vol. 123, no. 41, p. 25197–25208, 2019.

[90] J. Deng, Y. H. Lo, M. Gallagher-Jones, S. Chen, A. Pryor, Q. Jin, Y. P. Hong, Y. S. G. Nashed, S. Vogt, J. Miao, and C. Jacobsen, "Correlative 3d x-ray fluorescence and

ptychographic tomography of frozen-hydrated green algae," *Science Advances*, vol. 4, no. 11, p. 1–11, 2018.

[91] J. Bruley, M. J. Highland, S. O. Hruszkewycz, I. McNulty, C. E. Murray, M. V. Holt, A. Tripathi, P. H. Fuoss, O. G. Shpyrko, J. Holt, C. E. Murray, J. Bruley, J. Holt, A. Tripathi, O. G. Shpyrko, I. McNulty, M. J. Highland, and P. H. Fuoss, "Quantitative Nanoscale Imaging of Lattice Distortions in Epitaxial Semiconductor Heterostructures Using Nanofocused X-ray Bragg Projection Ptychography (SI)," *Nano Letters*, vol. 12, no. 10, pp. 5148–5154, 2012.

[92] B. R. Sutherland and E. H. Sargent, "Perovskite photonic sources," *Nature Photonics*, vol. 10, no. 5, pp. 295–302, 2016.

[93] S. De Wolf, J. Holovsky, S. J. Moon, P. Löper, B. Niesen, M. Ledinsky, F. J. Haug, J. H. Yum, and C. Ballif, "Organometallic halide perovskites: Sharp optical absorption edge and its relation to photovoltaic performance," *Journal of Physical Chemistry Letters*, vol. 5, no. 6, pp. 1035–1039, 2014.

[94] S. D. Stranks, V. M. Burlakov, T. Leijtens, J. M. Ball, A. Goriely, and H. J. Snaith, "Recombination kinetics in organic-inorganic perovskites: Excitons, free charge, and subgap states," 2014.

[95] H. J. Snaith, A. Abate, J. M. Ball, G. E. Eperon, T. Leijtens, N. K. Noel, S. D. Stranks, J. T.-W. W. Wang, K. Wojciechowski, and W. Zhang, "SP: Anomalous hysteresis in perovskite solar cells," *Journal of Physical Chemistry Letters*, vol. 5, pp. 1511–1515, may 2014.

[96] S. D. Stranks, G. E. Eperon, G. Grancini, C. Menelaou, M. J. Alcocer, T. Leijtens, L. M. Herz, A. Petrozza, and H. J. Snaith, "Electron-hole diffusion lengths exceeding 1 micrometer in an organometal trihalide perovskite absorber," *Science*, vol. 342, no. 6156, pp. 341–344, 2013.

[97] C. Sun, Y. Zhang, C. Ruan, C. Yin, X. Wang, Y. Wang, and W. W. Yu, "Efficient and stable white leds with silica-coated inorganic perovskite quantum dots," *Advanced Materials*, vol. 28, no. 45, pp. 10088–10094, 2016.

[98] Y. Zhang, W. Luo, C. Wang, Y. Li, C. Chen, J. Song, J. Dai, E. M. Hitz, S. Xu, C. Yang, Y. Wang, and L. Hu, "High-capacity, low-tortuosity, and channel-guided lithium metal anode," *Proceedings of the National Academy of Sciences*, vol. 114, no. 14, pp. 3584–3589, 2017.

[99] A. Swarnkar, R. Chulliyil, V. K. Ravi, M. Irfanullah, A. Chowdhury, and A. Nag, "Colloidal cspbbr3 perovskite nanocrystals: Luminescence beyond traditional quantum dots," *Angewandte Chemie - International Edition*, vol. 54, no. 51, pp. 15424–15428, 2015.

[100] M. Saliba, S. M. Wood, J. B. Patel, P. K. Nayak, J. Huang, J. A. Alexander-Webber, B. Wenger, S. D. Stranks, M. T. Hörantner, J. T. W. Wang, R. J. Nicholas, L. M. Herz,

M. B. Johnston, S. M. Morris, H. J. Snaith, and M. K. Riede, "Structured organic-inorganic perovskite toward a distributed feedback laser," *Advanced Materials*, vol. 28, no. 5, pp. 923–929, 2016.

[101] M. Zhang, H. Yu, M. Lyu, Q. Wang, J.-H. Yun, and L. Wang, "Composition-dependent photoluminescence intensity and prolonged recombination lifetime of perovskite ch ¡sub¿3¡/sub¿ nh ¡sub¿3¡/sub¿ pbbr ¡sub¿3x¡/sub¿ cl ¡sub¿x¡/sub¿ films," *Chem. Commun.*, vol. 50, no. 79, p. 11727–11730, 2014.

[102] H. Zhu, Y. Fu, F. Meng, X. Wu, Z. Gong, Q. Ding, M. V. Gustafsson, M. T. Trinh, S. Jin, and X. Y. Zhu, "Lead halide perovskite nanowire lasers with low lasing thresholds and high quality factors," *Nature Materials*, vol. 14, no. 6, pp. 636–642, 2015.

[103] C. C. Stoumpos, C. D. Malliakas, J. A. Peters, Z. Liu, M. Sebastian, J. Im, T. C. Chasapis, A. C. Wibowo, D. Y. Chung, A. J. Freeman, B. W. Wessels, and M. G. Kanatzidis, "Crystal growth of the perovskite semiconductor cspbbr3: A new material for high-energy radiation detection," *Crystal Growth and Design*, vol. 13, no. 7, pp. 2722–2727, 2013.

[104] Y. He, M. Petryk, Z. Liu, D. G. Chica, I. Hadar, C. Leak, W. Ke, I. Spanopoulos, W. Lin, D. Y. Chung, B. W. Wessels, Z. He, and M. G. Kanatzidis, "Cspbbr3 perovskite detectors with 1.4high-energy γ-rays," *Nature Photonics*, 2020.

[105] G. E. Eperon, G. M. Paternò, R. J. Sutton, A. Zampetti, A. A. Haghighirad, F. Cacialli, and H. J. Snaith, "Inorganic caesium lead iodide perovskite solar cells," *Journal of Materials Chemistry A*, vol. 3, no. 39, pp. 19688–19695, 2015.

[106] J. Duan, Y. Zhao, B. He, and Q. Tang, "High-purity inorganic perovskite films for solar cells with 9.72 International Edition, vol. 57, no. 14, pp. 3787–3791, 2018.

[107] J. Liang, C. Wang, Y. Wang, Z. Xu, Z. Lu, Y. Ma, H. Zhu, Y. Hu, C. Xiao, X. Yi, G. Zhu, H. Lv, L. Ma, T. Chen, Z. Tie, Z. Jin, and J. Liu, "All-inorganic perovskite solar cells," *Journal of the American Chemical Society*, vol. 138, no. 49, pp. 15829–15832, 2016.

[108] C. Liu, W. Li, C. Zhang, Y. Ma, J. Fan, and Y. Mai, "All-inorganic cspbi2br perovskite solar cells with high efficiency exceeding 13," *Journal of the American Chemical Society*, vol. 140, no. 11, pp. 3825–3828, 2018.

[109] J. Liang, J. Liu, and Z. Jin, "All-inorganic halide perovskites for optoelectronics: Progress and prospects," *Solar Rrl*, vol. 1, no. 10, p. 1700086, 2017.

[110] Y. Zhao, J. Duan, H. Yuan, Y. Wang, X. Yang, B. He, and Q. Tang, "Using sno2 qds and csmbr3 (m= sn, bi, cu) qds as charge-transporting materials for 10.6%-efficiency all-inorganic cspbbr3 perovskite solar cells with an ultrahigh open-circuit voltage of 1.610 v," *Solar Rrl*, vol. 3, no. 3, p. 1800284, 2019.

[111] A. K. Jena, A. Kulkarni, Y. Sanehira, M. Ikegami, and T. Miyasaka, "Stabilization of α-cspbi3 in ambient room temperature conditions by incorporating eu into cspbi3," *Chemistry of Materials*, vol. 30, no. 19, pp. 6668–6674, 2018.

[112] R. Yuan, L. Shen, C. Shen, J. Liu, L. Zhou, W. Xiang, and X. Liang, "Cspbbr3:: X eu3+ perovskite qd borosilicate glass: A new member of the luminescent material family," *Chemical Communications*, vol. 54, no. 27, pp. 3395–3398, 2018.

[113] C. Li, X. Lu, W. Ding, L. Feng, Y. Gao, and Z. Guo, "Formability of ¡i¿abx¡/i¿ ¡sub¿3¡/sub¿ (¡i¿x¡/i¿ = f, cl, br, i) halide perovskites," *Acta Crystallographica Section B Structural Science*, vol. 64, no. 6, pp. 702–707, 2008.

[114] G. Kieslich, S. Sun, and A. K. Cheetham, "An extended tolerance factor approach for organic-inorganic perovskites," *Chemical Science*, vol. 6, p. 3430–3433, 2015.

[115] C. J. Bartel, C. Sutton, B. R. Goldsmith, R. Ouyang, C. B. Musgrave, L. M. Ghiringhelli, and M. Scheffler, "New tolerance factor to predict the stability of perovskite oxides and halides," *Science Advances*, vol. 5, no. 2, p. eaav0693, 2019.

[116] W. Xiang, Z. Wang, D. J. Kubicki, W. Tress, J. Luo, D. Prochowicz, S. Akin, L. Emsley, J. Zhou, G. Dietler, M. Grätzel, and A. Hagfeldt, "Europium-doped cspbi 2 br for stable and highly efficient inorganic perovskite solar cells," *Joule*, vol. 3, no. 1, pp. 205–214, 2019.

[117] N. Li, Y. Luo, Z. Chen, X. Niu, X. Zhang, J. Lu, R. Kumar, J. Jiang, H. Liu, X. Guo, B. Lai, G. Brocks, Q. Chen, S. Tao, D. P. Fenning, and H. Zhou, "Microscopic degradation in formamidinium-cesium lead iodide perovskite solar cells under operational stressors," *Joule*, vol. 4, no. 8, p. 1743–1758, 2020.

[118] L. Protesescu, S. Yakunin, M. I. Bodnarchuk, F. Krieg, R. Caputo, C. H. Hendon, R. X. Yang, A. Walsh, and M. V. Kovalenko, "Nanocrystals of cesium lead halide perovskites (cspbx 3, x = cl, br, and i): Novel optoelectronic materials showing bright emission with wide color gamut," *Nano Letters*, vol. 15, no. 6, pp. 3692–3696, 2015.

[119] G. Pan, X. Bai, D. Yang, X. Chen, P. Jing, S. Qu, L. Zhang, D. Zhou, J. Zhu, W. Xu, B. Dong, and H. Song, "Doping lanthanide into perovskite nanocrystals: Highly improved and expanded optical properties," *Nano Letters*, vol. 17, no. 12, pp. 8005–8011, 2017.

[120] G. Xiong, L. Yuan, Y. Jin, H. Wu, Z. Li, B. Qu, G. Ju, L. Chen, S. Yang, and Y. Hu, "Aliovalent doping and surface grafting enable efficient and stable lead-free blue-emitting perovskite derivative," *Advanced Optical Materials*, vol. 8, no. 20, p. 2000779, 2020.

[121] L. Wang, H. Zhou, J. Hu, B. Huang, M. Sun, B. Dong, G. Zheng, Y. Huang, Y. Chen, L. Li, Z. Xu, N. Li, Z. Liu, Q. Chen, L. D. Sun, and C. H. Yan, "A eu 3+ -eu 2+ ion redox shuttle imparts operational durability to pb-i perovskite solar cells," *Science*, vol. 363, no. 6424, pp. 265–270, 2019.

[122] P. N. Rudd and J. Huang, "Metal ions in halide perovskite materials and devices," *Trends in Chemistry*, vol. 1, no. 4, pp. 394–409, 2019.

[123] N. Ding, D. Zhou, G. Pan, W. Xu, X. Chen, D. Li, X. Zhang, J. Zhu, Y. Ji, and H. Song, "Europium-doped lead-free cs3bi2br9 perovskite quantum dots and ultrasensitive cu2+ detection," *ACS Sustainable Chemistry and Engineering*, vol. 7, no. 9, pp. 8397–8404, 2019.

[124] S. Yang, H. Zhao, Y. Han, C. Duan, Z. Liu, and S. Liu, "Europium and acetate co-doping strategy for developing stable and efficient cspbi2br perovskite solar cells," *Small*, vol. 15, no. 46, p. 1904387, 2019.

[125] X. Wu, H. Li, K. Wang, X. Sun, and L. Wang, "Ch3nh3pb1-: Xeuxi3 mixed halide perovskite for hybrid solar cells: The impact of divalent europium doping on efficiency and stability," *RSC Advances*, vol. 8, no. 20, pp. 11095–11101, 2018.

[126] P. Khoram, S. Brittman, W. I. Dzik, J. N. Reek, and E. C. Garnett, "Growth and characterization of pdms-stamped halide perovskite single microcrystals," *Journal of Physical Chemistry C*, vol. 120, no. 12, pp. 6475–6481, 2016.

[127] R. D. Shannon, "Revised effective ionic radii and systematic studies of interatomic distances in halides and chalcogenides," *Acta crystallographica section A: crystal physics, diffraction, theoretical and general crystallography*, vol. 32, no. 5, pp. 751–767, 1976.

[128] T. Ungár, "Microstructural parameters from x-ray diffraction peak broadening," *Scripta Materialia*, vol. 51, no. 8 SPEC. ISS., pp. 777–781, 2004.

[129] D. Kim, Y. H. Jin, K. W. Jeon, S. J. S. Kim, S. J. S. Kim, O. H. Han, D. K. Seo, and J. C. Park, "Blue-silica by eu2+-activator occupied in interstitial sites," *RSC Advances*, vol. 5, no. 91, pp. 74790–74801, 2015.

[130] X. Li, Y. Luo, M. V. Holt, Z. Cai, and D. P. Fenning, "Residual nanoscale strain in cesium lead bromide perovskite reduces stability and shifts local luminescence," *Chemistry of Materials*, vol. 31, no. 8, pp. 2778–2785, 2019.

[131] Q. Ye, Y. Zhao, S. Mu, F. Ma, F. Gao, Z. Chu, Z. Yin, P. Gao, X. Zhang, and J. You, "Cesium lead inorganic solar cell with efficiency beyond 18reduced charge recombination," *Advanced Materials*, vol. 31, no. 49, p. 1905143, 2019.

[132] *OASYS: A software for beamline simulations and synchrotron virtual experiments*, Author(s), 2019.

[133] B. Lai and F. Cerrina, "Shadow: A synchrotron radiation ray tracing program," *Nuclear Instruments and Methods in Physics Research Section A: Accelerators, Spectrometers, Detectors and Associated Equipment*, vol. 246, no. 1-3, p. 337–341, 1986.

[134] M. del Rio, N. Canestrari, F. Jiang, and F. Cerrina, "Shadow3: a new version of the synchrotron x-ray optics modelling package.," *J Synchrotron Radiat*, vol. 18, no. Pt 5, p. 708–716, 2011.

[135] B. L. Henke, E. M. Gullikson, and J. C. Davis, "X-ray interactions: photoabsorption, scattering, transmission, and reflection at e= 50-30,000 ev, z= 1-92," *Atomic data and nuclear data tables*, vol. 54, no. 2, p. 181–342, 1993.

[136] D. Pettit and P. Fontana, "Comparison of sodium chloride hopper cubes grown under microgravity and terrestrial conditions.," *NPJ Microgravity*, vol. 5, p. 25, 2019.

[137] A. Kuczumow, Z. Rzączyńska, and M. Szewczak, "Matrix effects in the x-ray fluorescence method," *X-Ray Spectrometry*, vol. 11, no. 3, p. 135–139, 1982.

[138] M. Franzini, L. Leoni, and M. Saitta, "A simple method to evaluate the matrix effects in x-ray fluorescence analysis," *X-ray Spectrometry*, vol. 1, no. 4, p. 151–154, 1972.

[139] J. G. Nagy and D. P. O'Leary, "Restoring images degraded by spatially variant blur," *SIAM Journal on Scientific Computing*, vol. 19, no. 4, p. 1063–1082, 1998.

[140] J. C. Petruccelli, L. Tian, and C. Preza, eds., *Imaging through deconvolution with a spatially variant point spread function*, SPIE, 2021.

[141] *Semi-blind spatially-variant deconvolution in optical microscopy with local point spread function estimation by use of convolutional neural networks*, vol. 2018 25th IEEE International Conference on Image Processing (ICIP), IEEE, 2018.

[142] E. Marchetti, L. M. Close, and J.-P. Véran, eds., *Spatially variant PSF modeling and image deblurring*, SPIE, 2016.

[143] X. Chen, C. Dejoie, T. Jiang, C.-S. Ku, and N. Tamura, "Quantitative microstructural imaging by scanning laue x-ray micro- and nanodiffraction," *MRS Bulletin*, vol. 41, no. 6, p. 445–453, 2016.

[144] T. W. Cornelius and O. Thomas, "Progress of in situ synchrotron x-ray diffraction studies on the mechanical behavior of materials at small scales," *Progress in Materials Science*, vol. 94, p. 384–434, 2018.

[145] R. R. Hoffman, S. T. Mueller, G. Klein, and J. Litman, "Metrics for explainable ai: Challenges and prospects," *arXiv preprint arXiv:1812.04608*, 2018.

[146] G. Ice, B. Larson, J. Tischler, W. Liu, and W. Yang, "X-ray microbeam measurements of subgrain stress distributions in polycrystalline materials," *Materials Science and Engineering: A*, vol. 399, no. 1-2, p. 43–48, 2005.

[147] H. F. Poulsen, X. Fu, E. Knudsen, E. M. Lauridsen, L. Margulies, and S. Schmidt, "3dxrd – mapping grains and their dynamics in 3 dimensions," *Materials Science Forum*, vol. 467-470, p. 1363–1372, 2004.

[148] H. Simons, A. C. Jakobsen, S. R. Ahl, C. Detlefs, and H. F. Poulsen, "Multiscale 3d characterization with dark-field x-ray microscopy," *MRS Bulletin*, vol. 41, no. 6, p. 454–459, 2016.

[149] T. Tian, R. Morusupalli, H. Shin, H.-Y. Son, K.-Y. Byun, Y.-C. Joo, R. Caramto, L. Smith, Y.-L. Shen, M. Kunz, N. Tamura, and A. Budiman, "On the mechanical stresses of cu through-silicon via (tsv) samples fabricated by sk hynix vs. sematech – enabling robust and reliable 3-d interconnect/integrated circuit (ic) technology," *Procedia Engineering*, vol. 139, p. 101–111, 2016.

[150] M. Holt, R. Harder, R. Winarski, and V. Rose, "Nanoscale hard x-ray microscopy methods for materials studies," *Annual Review of Materials Research*, vol. 43, no. 1, p. 183–211, 2013.

[151] J. Deng, D. J. Vine, S. Chen, Q. Jin, Y. S. Nashed, T. Peterka, S. Vogt, and C. Jacobsen, "X-ray ptychographic and fluorescence microscopy of frozen-hydrated cells using continuous scanning," *Scientific Reports*, vol. 7, no. 1, p. 1–10, 2017.

[152] W. S. Drisdell, L. Leppert, C. M. Sutter-Fella, Y. Liang, Y. Li, Q. P. Ngo, L. F. Wan, S. Gul, T. Kroll, D. Sokaras, A. Javey, J. Yano, J. B. Neaton, F. M. Toma, D. Prendergast, and I. D. Sharp, "Determining atomic-scale structure and composition of organo-lead halide perovskites by combining high-resolution x-ray absorption spectroscopy and first-principles calculations," *ACS Energy Letters*, vol. 2, no. 5, p. 1183–1189, 2017.

[153] F. Pfeiffer, "X-ray ptychography," *Nature Photonics*, vol. 12, no. 1, pp. 9–17, 2018.

[154] T. W. Victor, L. M. Easthon, M. Ge, K. H. O'Toole, R. J. Smith, X. Huang, H. Yan, K. N. Allen, Y. S. Chu, and L. M. Miller, "X-ray fluorescence nanotomography of single bacteria with a sub-15 nm beam," *Scientific Reports*, vol. 8, no. 1, p. 1–8, 2018.

[155] D. J. Vine, D. Pelliccia, C. Holzner, S. B. Baines, A. Berry, I. McNulty, S. Vogt, A. G. Peele, and K. A. Nugent, "Simultaneous X-ray fluorescence and ptychographic microscopy of Cyclotella meneghiniana," *Optics Express*, vol. 20, no. 16, p. 18287, 2012.

[156] *Multimodal, Multidimensional, and Multiscale X-ray Imaging at the National Synchrotron Light Source II*, vol. 33(3), Informa UK Limited, 2020.

[157] T. Link, S. Zabler, A. Epishin, A. Haibel, M. Bansal, and X. Thibault, "Synchrotron tomography of porosity in single-crystal nickel-base superalloys," *Materials Science and Engineering: A*, vol. 425, no. 1-2, p. 47–54, 2006.

[158] L. Helfen, T. Baumbach, P. Mikulík, D. Kiel, P. Pernot, P. Cloetens, and J. Baruchel, "High-resolution three-dimensional imaging of flat objects by synchrotron-radiation computed laminography," *Applied Physics Letters*, vol. 86, no. 7, p. 071915, 2005.

[159] L. Helfen, A. Myagotin, A. Rack, P. Pernot, P. Mikulík, M. Di Michiel, and T. Baumbach, "Synchrotron-radiation computed laminography for high-resolution three-dimensional imaging of flat devices," *physica status solidi (a)*, vol. 204, no. 8, p. 2760–2765, 2007.

[160] L. P. Hunter, "Direct measurement of the angular dependence of the imaginary part of the atomic scattering factor of germanium," *IBM Journal of Research and Development*, vol. 3, no. 2, p. 106–113, 1959.

[161] N. Ritchie, "Efficient simulation of secondary fluorescence via nist dtsa-ii monte carlo.," *Microsc Microanal*, vol. 23, no. 3, p. 618–633, 2017.

[162] A. G. Karydas, "Self-element secondary fluorescence enhancement in xrf analysis," *X-Ray Spectrometry*, vol. 34, no. 5, p. 426–431, 2005.

[163] A. Shajkofci and M. Liebling, "Spatially-variant cnn-based point spread function estimation for blind deconvolution and depth estimation in optical microscopy," *IEEE Transactions on Image Processing*, vol. 29, p. 5848–5861, 2020.

[164] M. Weigert, U. Schmidt, T. Boothe, A. Müller, A. Dibrov, A. Jain, B. Wilhelm, D. Schmidt, C. Broaddus, S. Culley, M. Rocha-Martins, F. Segovia-Miranda, C. Norden, R. Henriques, M. Zerial, M. Solimena, J. Rink, P. Tomancak, L. Royer, F. Jug, and E. Myers, "Content-aware image restoration: pushing the limits of fluorescence microscopy.," *Nat Methods*, vol. 15, no. 12, p. 1090–1097, 2018.

[165] D. He, D. Cai, J. Zhou, J. Luo, and S.-L. Chen, "Restoration of out-of-focus fluorescence microscopy images using learning-based depth-variant deconvolution," *IEEE Photonics Journal*, vol. 12, no. 2, p. 1–13, 2020.

[166] B. P. MacLeod, F. G. Parlane, T. D. Morrissey, F. Häse, L. M. Roch, K. E. Dettelbach, R. Moreira, L. P. Yunker, M. B. Rooney, J. R. Deeth, V. Lai, G. J. Ng, H. Situ, R. H. Zhang, M. S. Elliott, T. H. Haley, D. J. Dvorak, A. Aspuru-Guzik, J. E. Hein, and C. P. Berlinguette, "Self-driving laboratory for accelerated discovery of thin-film materials," *Science Advances*, vol. 6, no. 20, 2020.

[167] J. Wagner, C. G. Berger, X. Du, T. Stubhan, J. A. Hauch, and C. J. Brabec, "The evolution of materials acceleration platforms: toward the laboratory of the future with amanda," *Journal of Materials Science*, vol. 56, no. 29, p. 16422–16446, 2021.

[168] J. Xu, "Autonomous robotic platform (polybot) for conjugated polymer processing," *Bulletin of the American Physical Society*, 2022.

[169] E. Stach, B. DeCost, A. G. Kusne, J. Hattrick-Simpers, K. A. Brown, K. G. Reyes, J. Schrier, S. Billinge, T. Buonassisi, I. Foster, C. P. Gomes, J. M. Gregoire, A. Mehta, J. Montoya, E. Olivetti, C. Park, E. Rotenberg, S. K. Saikin, S. Smullin, V. Stanev, and B. Maruyama, "Autonomous experimentation systems for materials development: A community perspective," *Matter*, 2021.

[170] M. Christensen, L. Yunker, P. Shiri, T. Zepel, P. Prieto, S. Grunert, F. Bork, and J. Hein, "Automation isn't automatic.," *Chem Sci*, vol. 12, no. 47, p. 15473–15490, 2021.

[171] M. R. Garey, D. S. Johnson, and R. Sethi, "The complexity of flowshop and jobshop scheduling," *Mathematics of Operations Research*, vol. 1, no. 2, pp. 117–129, 1976.

[172] D. S. Hochba, "Approximation algorithms for np-hard problems," *ACM Sigact News*, vol. 28, no. 2, pp. 40–52, 1997.

[173] G. J. Woeginger, "Exact algorithms for np-hard problems: A survey," in *Combinatorial optimization—eureka, you shrink!*, pp. 185–207, Springer, 2003.

[174] A. S. Jain and S. Meeran, "Deterministic job-shop scheduling: Past, present and future," *European journal of operational research*, vol. 113, no. 2, p. 390–434, 1999.

[175] G. Da Col and E. Teppan, "Google vs ibm: A constraint solving challenge on the job-shop scheduling problem," *Electronic Proceedings in Theoretical Computer Science*, vol. 306, p. 259–265, 2019.

[176] L. Perron and V. Furnon, "Or-tools."

[177] L. Bordeaux, Y. Hamadi, and L. Zhang, "Propositional satisfiability and constraint programming: A comparative survey," *ACM Computing Surveys (CSUR)*, vol. 38, no. 4, pp. 12–es, 2006.

[178] D. Lee and M. Yannakakis, "Principles and methods of testing finite state machines-a survey," *Proceedings of the IEEE*, vol. 84, no. 8, pp. 1090–1123, 1996.

[179] L. Bassett, *Introduction to JavaScript object notation: a to-the-point guide to JSON*. " O'Reilly Media, Inc.", 2015.

[180] O. Ramström and J.-M. Lehn, "Drug discovery by dynamic combinatorial libraries," *Nature Reviews Drug Discovery*, vol. 1, no. 1, pp. 26–36, 2002.

[181] J. P. Hughes, S. Rees, S. B. Kalindjian, and K. L. Philpott, "Principles of early drug discovery," *British journal of pharmacology*, vol. 162, no. 6, pp. 1239–1249, 2011.

[182] T. Kenakin and A. Christopoulos, "Signalling bias in new drug discovery: detection, quantification and therapeutic impact," *Nature reviews Drug discovery*, vol. 12, no. 3, pp. 205–216, 2013.

[183] A. Knauer, S. Schneider, F. Möller, A. Csáki, W. Fritzsche, and J. Köhler, "Screening of plasmonic properties of composed metal nanoparticles by combinatorial synthesis in micro-fluid segment sequences," *Chemical Engineering Journal*, vol. 227, pp. 80–89, 2013. IMRET 12: Proceedings of the Twelfth International Conference on Microreaction Technology.

[184] D. S. Koktysh and W. Pham, "A combinatorial approach for the fabrication of magneto-optical hybrid nanoparticles," *International Journal of Nanomedicine*, vol. 14, p. 9855, 2019.

[185] E. M. Chan, "Combinatorial approaches for developing upconverting nanomaterials: high-throughput screening, modeling, and applications," *Chemical Society Reviews*, vol. 44, no. 6, pp. 1653–1679, 2015.

[186] C. R. Brown, E. McCalla, C. Watson, and J. Dahn, "Combinatorial study of the li–ni–mn–co oxide pseudoquaternary system for use in li–ion battery materials research," *ACS combinatorial science*, vol. 17, no. 6, pp. 381–391, 2015.

[187] A. Todd, R. Mar, and J. Dahn, "Combinatorial study of tin-transition metal alloys as negative electrodes for lithium-ion batteries," *Journal of the Electrochemical Society*, vol. 153, no. 10, p. A1998, 2006.

[188] J. Dahn, R. Mar, and A. Abouzeid, "Combinatorial study of sn1- x co x (0¡ x¡ 0.6) and [sn0. 55co0. 45] 1- y c y (0¡ y¡ 0.5) alloy negative electrode materials for li-ion batteries," *Journal of The Electrochemical Society*, vol. 153, no. 2, p. A361, 2005.

[189] U. Manber, *Introduction to algorithms: a creative approach*. Addison-Wesley Longman Publishing Co., Inc., 1989.

[190] J. Schrier, "Solution mixing calculations as a geometry, linear algebra, and convex analysis problem," *Journal of Chemical Education*, vol. 98, no. 5, p. 1659–1666, 2021.

[191] A. B. Kahn, "Topological sorting of large networks," *Communications of the ACM*, vol. 5, no. 11, pp. 558–562, 1962.

[192] J. Li, E. Alvianto, and Y. Hou, "Developing the Next-Generation Perovskite/Si Tandems: Toward Efficient, Stable, and Commercially Viable Photovoltaics," *ACS Applied Materials Interfaces*, may 2022.

[193] J. Werner, B. Niesen, and C. Ballif, "Perovskite/Silicon Tandem Solar Cells: Marriage of Convenience or True Love Story? – An Overview," *Advanced Materials Interfaces*, vol. 5, p. 1700731, jan 2018.

[194] L. Li, S. Basu, Y. Wang, Z. Chen, P. Hundekar, B. Wang, J. Shi, Y. Shi, S. Narayanan, and N. Koratkar, "Self-heating-induced healing of lithium dendrites," *Science*, vol. 359, no. 6383, pp. 1513–1516, 2018.

[195] J. S. Manser, M. I. Saidaminov, J. A. Christians, O. M. Bakr, and P. V. Kamat, "Making and Breaking of Lead Halide Perovskites," *Accounts of Chemical Research*, vol. 49, pp. 330–338, feb 2016.

[196] D. P. McMeekin, G. Sadoughi, W. Rehman, G. E. Eperon, M. Saliba, M. T. Hörantner, A. Haghighirad, N. Sakai, L. Korte, B. Rech, M. B. Johnston, L. M. Herz, and H. J. Snaith, "A mixed-cation lead mixed-halide perovskite absorber for tandem solar cells," *Science*, vol. 351, pp. 151–155, jan 2016.

[197] K. A. Bush, S. Manzoor, K. Frohna, Z. J. Yu, J. A. Raiford, A. F. Palmstrom, H.-P. Wang, R. Prasanna, S. F. Bent, Z. C. Holman, and M. D. McGehee, "Minimizing Current and Voltage Losses to Reach 25Two-Terminal Perovskite–Silicon Tandem Solar Cells," *ACS Energy Letters*, vol. 3, pp. 2173–2180, sep 2018.

[198] E. Aydin, T. G. Allen, M. De Bastiani, L. Xu, J. Ávila, M. Salvador, E. Van Kerschaver, and S. De Wolf, "Interplay between temperature and bandgap energies on the outdoor performance of perovskite/silicon tandem solar cells," *Nature Energy*, vol. 5, pp. 851–859, nov 2020.

[199] J. Tong, Q. Jiang, F. Zhang, S. B. Kang, D. H. Kim, and K. Zhu, "Wide-Bandgap Metal Halide Perovskites for Tandem Solar Cells," *ACS Energy Letters*, vol. 6, no. 1, pp. 232–248, 2021.

[200] P. Makuła, M. Pacia, and W. Macyk, "How to correctly determine the band gap energy of modified semiconductor photocatalysts based on uv-vis spectra.," *J Phys Chem Lett*, vol. 9, no. 23, p. 6814–6817, 2018.

[201] J. Tauc, R. Grigorovici, and A. Vancu, "Optical properties and electronic structure of amorphous germanium," *physica status solidi (b)*, vol. 15, no. 2, p. 627–637, 1966.

[202] J. Xu, C. Boyd, Z. Yu, A. Palmstrom, D. Witter, B. Larson, R. France, J. Werner, S. Harvey, E. Wolf, W. Weigand, S. Manzoor, M. van Hest, J. Berry, J. Luther, Z. Holman, and M. McGehee, "Triple-halide wide-band gap perovskites with suppressed phase segregation for efficient tandems.," *Science*, vol. 367, no. 6482, p. 1097–1104, 2020.

[203] S. Siebentritt, T. P. Weiss, M. Sood, M. H. Wolter, A. Lomuscio, and O. Ramirez, "How photoluminescence can predict the efficiency of solar cells," *Journal of Physics: Materials*, vol. 4, p. 042010, 2021.

[204] M. B. Brown and A. B. Forsythe, "Robust tests for the equality of variances," *Journal of the American Statistical Association*, vol. 69, no. 346, p. 364–367, 1974.

[205] G. E. Eperon, K. H. Stone, L. E. Mundt, T. H. Schloemer, S. N. Habisreutinger, S. P. Dunfield, L. T. Schelhas, J. J. Berry, and D. T. Moore, "The Role of Dimethylammonium in Bandgap Modulation for Stable Halide Perovskites," *ACS Energy Letters*, vol. 5, pp. 1856–1864, jun 2020.

[206] A. Taylor, Q. Sun, K. Goetz, Q. An, T. Schramm, Y. Hofstetter, M. Litterst, F. Paulus, and Y. Vaynzof, "A general approach to high-efficiency perovskite solar cells by any antisolvent.," *Nat Commun*, vol. 12, no. 1, p. 1878, 2021.

[207] K. Wang, M. Tang, H. Dang, R. Munir, D. Barrit, M. De Bastiani, E. Aydin, D. Smilgies, S. De Wolf, and A. Amassian, "Kinetic stabilization of the sol-gel state in perovskites enables facile processing of high-efficiency solar cells.," *Adv Mater*, vol. 31, no. 32, p. e1808357, 2019.

[208] Q. An, L. Vieler, K. P. Goetz, O. Telschow, Y. J. Hofstetter, R. Buschbeck, A. D. Taylor, and Y. Vaynzof, "Effect of antisolvent application rate on film formation and photovoltaic performance of methylammonium-free perovskite solar cells," *Advanced Energy and Sustainability Research*, vol. 2, no. 11, p. 2100061, 2021.

[209] K. P. Goetz and Y. Vaynzof, "The challenge of making the same device twice in perovskite photovoltaics," *ACS Energy Letters*, p. 1750–1757, 2022.